

# *Inhomogeneous magnetic fields*

*A theoretical study of their  
effects on the transport properties  
of a two-dimensional electron gas*

**Jonas Reijnders**

**Condensed Matter Theory  
Physics Department  
University of Antwerp, Belgium**



# *Contents*

<b>1</b>	<b>Introduction</b>	<b>1</b>
1.1	The two-dimensional electron gas (2DEG)	2
1.1.1	How to create a 2DEG?	2
1.1.2	The Hamiltonian	4
1.1.3	Properties	4
1.1.4	Transport in a 2DEG	6
1.2	Influence of a homogeneous magnetic field	6
1.3	Influence of inhomogeneous magnetic fields	10
1.3.1	How to create them	10
1.3.2	New physics?	13
1.4	Theoretical approach	15
1.5	Quantum regime	17
1.5.1	2DEG in a (in)homogeneous magnetic field in one direction	18
1.5.2	2DEG in a cylindrical symmetric (in)homogeneous magnetic field	19
1.5.3	Scattering on a cylindrical symmetric magnetic profile	19
1.5.4	A Quantum wire	21
1.6	Ballistic regime	24
1.7	Diffusive regime	25

1.8	Classical regime	25
1.9	Applications	26
1.9.1	Magnetic Random Access Memory device	27
1.9.2	Magnetic field sensor	27
1.9.3	Magnetometer	28
1.10	Organization of the thesis	28
<b>2</b>	<b>Quantum states in a magnetic anti-dot</b>	<b>31</b>
2.1	Introduction	32
2.2	Magnetic field profile	33
2.3	The energy spectrum	35
2.4	The probability current distribution and the magnetic moment	39
2.5	Optical properties	43
2.6	Conclusions	44
<b>3</b>	<b>Snake orbits and related magnetic edge states</b>	<b>47</b>
3.1	Introduction	48
3.2	Theoretical approach	49
3.3	In the absence of a background magnetic field	50
3.3.1	Limiting behaviour for $k \rightarrow \pm\infty$	50
3.3.2	Spectrum and velocity	52
3.3.3	Classical picture	54
3.4	With a background magnetic field	55
3.4.1	$0 < B < B_0$	55
3.4.2	$B = B_0$	56
3.4.3	$B_0 > B$	57
3.5	Negative velocity state	58
3.6	Time dependent classical interpretation	62
3.6.1	$B = 0$	62
3.6.2	$B > B_0$	64
3.7	Conclusions	65
<b>4</b>	<b>Scattering on circular symmetric magnetic profiles</b>	<b>67</b>
4.1	Introduction	68
4.2	Scattering on a single profile	69
4.2.1	Classical scattering	69
4.2.2	Quantum mechanical scattering	70
4.3	Scattering on multiple profiles	76

4.3.1	Solution of the Boltzmann equation	77
4.3.2	Classical result	77
4.3.3	Quantum mechanical result	79
4.4	Conclusions	82
<b>5</b>	<b>Resistance effects due to magnetic guiding orbits</b>	<b>83</b>
5.1	Introduction	84
5.2	Theoretical approach	86
5.3	The energy spectrum and the two-terminal resistance	87
5.4	The Hall resistance	94
5.5	The magnetoresistance	95
5.6	Conclusions	97
<b>6</b>	<b>Hybrid ferromagnet/semiconductor Hall effect device</b>	<b>99</b>
6.1	Introduction	100
6.2	Setup of the device	100
6.3	Our theoretical approach	101
6.4	Results and discussion	102
6.5	Conclusions	105
<b>7</b>	<b>Diffusive transport and optimization of the hybrid Hall effect device</b>	<b>107</b>
7.1	Introduction	108
7.2	Temperature dependence of the Hall resistance	110
7.2.1	Diffusive regime	110
7.2.2	Ballistic regime	114
7.3	Determination of the optimal design parameters of the device	115
7.4	Conclusions	118
<b>8</b>	<b>Summary</b>	<b>119</b>
<b>9</b>	<b>Samenvatting</b>	<b>123</b>
<b>10</b>	<b>List of Publications</b>	<b>127</b>
<b>References</b>		<b>129</b>



# 1

---

## *Introduction*

During the last half century the field of solid-state electronics has drawn a lot of attention and consumed a lot of effort, which paid off at an almost continuous rate leading to a revolution in technology. What started with the discovery of the transistor, resulted subsequently in the integration of many circuit elements onto one semiconductor chip, allowing the writer to be a *typewriter*, assisted by a computer who is big in its compactness. We cannot imagine a world without computers or semi-conductor chips, and yet ... the transistor has only been discovered about fifty years ago.

Parallel with this revolution, and somehow stimulated by it, magnetic materials have been developed separately, mostly in view of applications related to the electronics revolution: they were necessary for information storage (tape, disk, magneto-optic disk) and for magnetic circuits. Nevertheless, this development took place far away from semiconductor systems.

It is only recently that one has started to incorporate magnetic materials into planar integrated electronic circuitry. In those integrated devices, the semiconductor properties are combined with and enhanced by the presence of magnetic elements. In a first level of integration, one fabricates on the same substrate a hybrid system consisting of separated magnetic and electronic components, a much higher level of integration is achieved when the presence of the magnetic elements modifies and enhances the behavior of the electronic devices by becoming part of them. This new technology will add a new functional dimension to the present semiconductor technology and will open new avenues for possible applications based on ... new physics.[5, 15, 85, 93]

The possibility provided by nowadays fabrication technologies, to create inhomogeneous magnetic field on a micrometer and nanometer scale, indeed

also raises questions from fundamental, theoretical point of view: how do electrons behave in mesoscopic samples under application of an inhomogeneous magnetic field. How can these magnetic fields be created and how do they influence the underlying two-dimensional electron gas (2DEG)? To which limit can we push (or use) the physics necessary for proper operation, and what happens beyond? The characterization of magnetic nanowires, magnetic dot arrays and so forth, will lead to an increased understanding of the physics of micromagnetism and magneto-electronics.

In this thesis we consider systems, consisting of a semiconductor heterojunction containing a 2DEG, with patterned ferromagnetic materials on top of it. The electrons move in locally inhomogeneous magnetic fields that alter the orbital motion of the electrons through the Lorentz force. Such magnetic fields also rearrange the energy spectrum of the electrons. We will not restrict ourselves to this situation, but we will also investigate other ways of creating magnetic field inhomogeneities, e.g. by means of deposition of superconducting materials, and we will study their effects on the properties of the underlying 2DEG. Because in typical III-V semiconductors the effective  $g$ -factor is small, the spin will be of secondary importance in the systems we study.

This chapter we will use to introduce you to the world of low dimensional semiconductor structures. First we will show how a 2DEG can be created in a heterojunction, we will discuss its properties and how one can tune them. We will discuss the effect of an homogeneous magnetic field on the 2DEG, before we focus on inhomogeneous magnetic field profiles. We gather the possible ways to create them, and summarize briefly the work which has been carried out in the past years on these systems. Next, we will characterize mesoscopic transport, and split it up into three major regions, the quantum, the ballistic and the diffusive regime, corresponding with different conditions of the system and therefore relying on different physics. We will stipulate briefly the theoretical complications imposed by each regime, and especially we will concentrate on the theory which is needed to comprehend the subsequent chapters. We will conclude this introduction by discussing the main drive behind magneto-electronic research: possible applications as magnetic random access memory (MRAM)[16, 38] and as magnetometer.[25, 47, 66]

## 1.1 THE TWO-DIMENSIONAL ELECTRON GAS

### 1.1.1 How to create a 2DEG?

There are several ways to physically realize a 2DEG-system. For example in metal-oxide-semiconductor inversion layers, on the surface of liquid Helium, and at the interface of semiconductor heterojunctions. We are mainly interested in 2DEG's created at the interface in semiconductor heterojunctions. For fundamental research, the most commonly used semiconductor interface

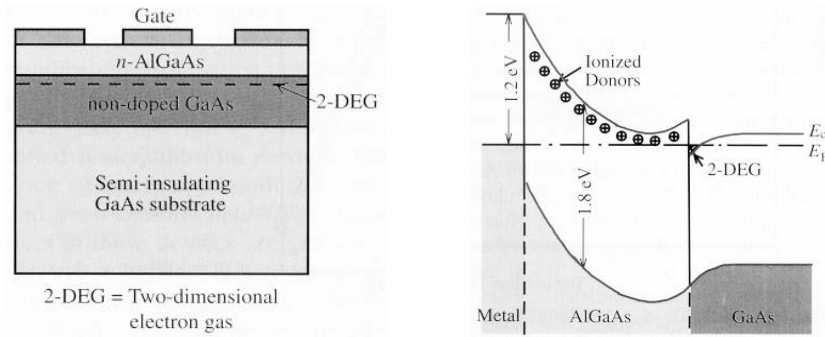


*Fig. 1.1* The structure and band diagram of a modulation-doped heterojunction between GaAs and  $n$ -AlGaAs.  $E_c$  and  $E_F$  represent, respectively, the conduction band edge and the Fermi energy. [from Ref. [97]]

to confine a 2DEG is the epitaxially grown  $\text{Al}_x\text{Ga}_{1-x}\text{As}$  heterojunction. The index  $x$  is the mole fraction of Ga-atoms replaced by Al-atoms keeping the III-V ratio the same. The structure and band diagram for this system are shown in Fig. 1.1. With the highly developed techniques of molecular beam epitaxy (MBE) and the metal organic chemical vapor deposition (MOCVD) it is possible to grow high quality epitaxial layers of crystalline semiconductors on top of each other. These layers form a single crystal which has regions with different material composition, doping levels and band gaps separated by atomically abrupt interfaces.

The principle is simple. A crystal of ultrapure undoped GaAs is grown, followed by a thin layer of moderately heavily  $n$ -doped AlGaAs. Because GaAs has a narrow energy gap between the top of the valence band and the bottom of the conduction band, it acts as a semiconductor, whereas AlGaAs has a wider gap and acts as an insulator or a barrier. The difference between the energy gaps in the two regions make the bottom of the conduction band in AlGaAs higher in energy than the bottom of the conduction band in GaAs. As a consequence the electrons in the  $n$ -type AlGaAs can be liberated from the donors by temperature or by light, and can lower their energy by migrating from the doped wide-gap AlGaAs layer to the undoped narrow-gap GaAs layer. This process of spatial charge separation between the electrons and the positive Silicon ions leads to an electric field built up across the interface with the subsequent band bending in the two regions until the Fermi energy is uniform throughout the structure.

Ended up there, they cannot easily return, as the potential barrier is typically about 0.2 eV high, i.e. corresponding to a thermal energy of about 2000 K. The electrons are trapped in this barrier, but the residual Coulomb interaction keeps them at the surface, with the net formation of a dipole layer. This layer is typically about 10-20 nm thick. The almost triangular potential well at the interface confines the motion of the electrons normal to the interface

leading to a discrete energy spectrum for motion in that direction while they remain free to move parallel to the interface and thus creating a 2DEG.

### 1.1.2 The Hamiltonian

Because of the translational invariance in the plane of the heterojunction interface, the single electron Hamiltonian in the effective mass approximation is a direct sum of the free motion in the  $xy$ -plane and a confined motion perpendicular to the plane, i.e. the  $z$ -direction

$$H = \frac{1}{2m}(p_x^2 + p_y^2) + \left[ \frac{1}{2m}p_z^2 + V(z) \right], \quad (1.1)$$

where  $m \approx 0.067m_e$  is the electron effective mass in GaAs and  $V(z)$  is the total confining potential in the  $z$ -direction. The corresponding Schrödinger equation is separable, since we can write the electron wavefunction as

$$\Psi = e^{ik_x x + ik_y y} \xi(z), \quad (1.2)$$

which after insertion into the Schrödinger equation, results in a 1D  $z$ -dependent equation. If  $V(z)$  is approximated by a triangular well  $V(z) = eEz$  for  $z \geq 0$  and  $V(z) = \infty$  for  $z < 0$ , where  $E$  is an effective electric field, the quantized energies read

$$\epsilon_n = \left[ \frac{\hbar^2 e^2 E^2}{2m} \right]^{\frac{1}{3}} \left[ \frac{3\pi}{2} \left( n + \frac{3}{4} \right) \right]^{\frac{2}{3}}, \quad (1.3)$$

and the  $\xi(z)$  wave functions are given by the corresponding Airy functions. The energy dispersion of the 2DEG is then given by

$$\epsilon_{nk} = \epsilon_n + \frac{\hbar^2 k^2}{2m}, \quad k^2 = k_x^2 + k_y^2. \quad (1.4)$$

In most cases only the lowest electric subband is populated and since it is only an added constant ( $\epsilon_0$ ) to the total energy, we set it to zero from now on.

### 1.1.3 Properties

In absence of an electric and magnetic field, the Fermi surface is a disk with radius  $k_F = \sqrt{2m\epsilon_F}/\hbar$ . The Fermi energy  $\epsilon_F$  depends on the number of electrons. In a free 2DEG this relation is given by  $\epsilon_F = \pi\hbar^2 n_e/m$ . In contrast to metallic systems, it is possible in these structures to change the electronic properties by doping, and to vary the electron density by application of an external gate voltage.

If no electric field is applied, there is no net current flowing: for every  $\mathbf{k}$ -value, its opposite  $-\mathbf{k}$  is also present. However, application of an electric field along the  $x$  direction, will induce a difference in the chemical potentials

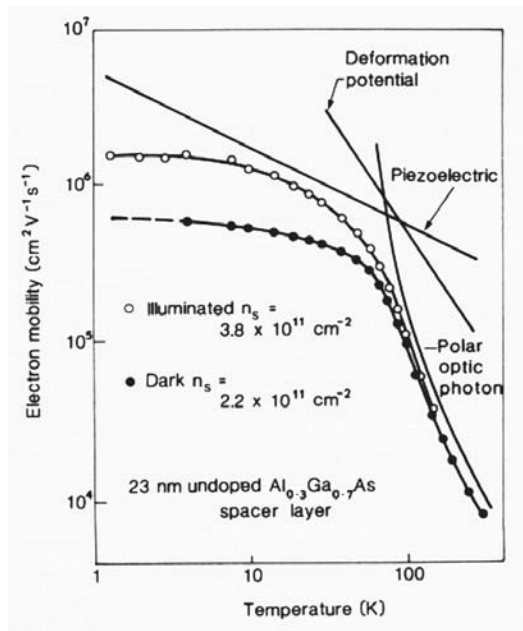


Fig. 1.2 Mobility of a 2DEG in a modulation doped GaAs/Ga<sub>0.7</sub>Al<sub>0.3</sub>As heterojunction as a function of temperature. The circles indicate the experimental results. The solid curves represent calculated contributions to the mobility from different scattering mechanisms [taken from Ref.[41]].

$\mu(x \rightarrow -\infty)$  and  $\mu(x \rightarrow -\infty)$ , and this will result in a slight deformation, a tilting of the Fermi disk, which results in a majority of electrons with momenta to the left/right side, and consequently a current will flow. Therefore, only electrons at the Fermi energy contribute to the conduction.

Since these 2D electrons are physically separated from the ionized impurities, they will not be bound to them when  $T \rightarrow 0$  and the mobility does not decrease as the temperature is decreased as depicted in Fig. 1.2. Hence at very low temperatures and in very pure materials, where the Coulomb scattering would otherwise be large, it is found that the mobility of electrons at heterojunctions can exceed the values in low-doped bulk material by factors in excess of 1000. The mean free path can approach fractions of a millimeter, and electrons retain their phase memory over this distance.

In addition, the lateral structure of the inversion layers can be systematically influenced by voltages and external gates. This enables us to construct almost any desirable geometry in the 2DEG. Therefore, they can be considered as perfect laboratories for the investigation of quantum (coherent) transport.

As we will see further, often other types of heterojunctions are used (e.g., InAs), which all benefit from the same physics, but have other properties.

The choice which heterojunctions are used in the experiment, does not only depend on the mentioned parameters, but also on the materials we want to grow on top of it. Since we want to combine these heterostructures with other materials (ferromagnets, superconductors), in order to create inhomogeneous magnetic fields in the 2DEG, the lattice constant of the used material is also important and should be more or less the same, if one wants to grow the layers epitaxially.

#### 1.1.4 Transport in a 2DEG

The classical charge transport in metals is described by the Drude theory. The basic result is that the DC-conductivity of a metal is  $\sigma = ne^2\tau/m$ , with the density of electrons  $n_e$  (charge  $-e$ ), the effective mass  $m$  and the *mean free time*  $\tau$ . The latter incorporates all of the scattering processes the electrons suffer from static impurities, vacancies and dislocations, and also from other elementary processes like electron-phonon and electron-electron scattering. The basic assumption behind the Drude theory is that scatterings are *incoherent*, i.e. the electrons, after having suffered a collision, do not “remember” that they existed before. Subject to the influence of the electric field, they move diffusively through the lattice. At sufficiently low temperatures this assumption breaks down. The quantum mechanical nature of the electrons comes into play. Incoherent processes that destroy the phase memory of the electrons, as electron-phonon scattering, are more or less “frozen” out. What remains is scattering at impurities which is not incoherent. The quantum mechanical state of an electron now depends on the configuration of all of the imperfections, which alters the transport properties: fascinating effects due to *localization*, as backscattering, *universal conductance fluctuations* (UCF’s), etc. arise.

In a 2D system, the same transport peculiarities can be observed, even more pronounced as a result of the enhanced localization by the additional confinement. More important for our work, is the fact that because the mobility can be much larger, it is possible to study electron transport in systems where even coherent scattering plays a minor role. This allows us to investigate mesoscopic transport in different regions: the diffusive, ballistic and quantum regime, which we will discuss in detail further in this introduction.

## 1.2 INFLUENCE OF A HOMOGENEOUS MAGNETIC FIELD

If we want to report on the effects of an homogeneous magnetic field on the 2DEG, we should discuss its implications in the different regimes. Since we only aim at a brief introduction, we will restrict ourselves to the ideal case, and solve the problem quantum mechanically for an infinite 2DEG subjected

to a homogeneous magnetic field where no scatterers are present, as was done by Landau many decades ago.

We will restrict ourselves to the one-electron case, since all of the phenomena that we discuss in this thesis are essentially one-electron phenomena. Most of the experimental observations to date are well explained, at least qualitatively, in terms of the simple one-particle picture. A notable exception however, is the *fractional quantum Hall effect*, [46] which resulted in a Nobel prize and still is a hot topic in present day research. This effect occurs at very low temperatures ( $\approx 150$  mK) in very pure samples if a large magnetic field is applied. Therefore it is out of the scope of this thesis.

In the presence of a homogeneous magnetic field  $B$  perpendicular to the heterojunction  $xy$ -plane, and subjected to an electric field  $\mathbf{E}$  in the  $x$ -direction, the single electron Hamiltonian reads

$$H = \frac{1}{2m} \left( \mathbf{p} + \frac{e\mathbf{A}}{c} \right)^2 + eEx. \quad (1.5)$$

It is convenient to choose the Landau gauge,  $\mathbf{A} = (0, Bx, 0)$ , which allows us to choose a wavefunction which has a plane-wave dependence on the  $y$ -coordinate

$$\psi(x, y) = e^{iky} \phi(x). \quad (1.6)$$

Substituting Eq. (1.6) into Eq. (1.5), the Schrödinger equation becomes

$$\left[ -\frac{\hbar^2}{2m} \frac{d^2}{dx^2} + \frac{1}{2} m \omega_c^2 (x - l_b^2 k)^2 + eEx \right] \phi(x) = \epsilon \phi(x), \quad (1.7)$$

where  $l_b = (\hbar c/eB)^{1/2}$  is the magnetic length and  $\omega_c = eB/mc$  is the cyclotron frequency. Eq. 1.7 can be easily solved by transformation to a familiar harmonic oscillator equation. The eigenvalues and eigenstates are

$$\epsilon_n(E) = \left( n + \frac{1}{2} \right) \hbar \omega_c + eE(l_b^2 k - eE/2m\omega_c^2) \quad (1.8)$$

$$\psi_n(x, y) = e^{-iky} e^{-(x-x_0)^2/2l_b^2} H_n[(x-x_0)/l_b], \quad (1.9)$$

where  $n = 0, 1, 2, 3, \dots$  and  $x_0 = l_b^2 k - eE/m\omega_c^2$ .

If no electric field is applied, i.e.  $E = 0$ , we obtain the discrete Landau levels. The density of states in this case is a series of delta functions

$$D(\epsilon) = 2 \sum_n \frac{eB}{h} \delta(\epsilon - \epsilon_n). \quad (1.10)$$

Classically, this corresponds to electrons circling around in closed orbits with different center  $x_0$  and with quantized cyclotron radii ( $R_c = v_F/\omega_c = \sqrt{(2n+1)}l_b$ ). Therefore, no net current is flowing in either the  $x$  or  $y$ -direction, as is clear from Fig. 1.3(a). The stronger the magnetic field, the

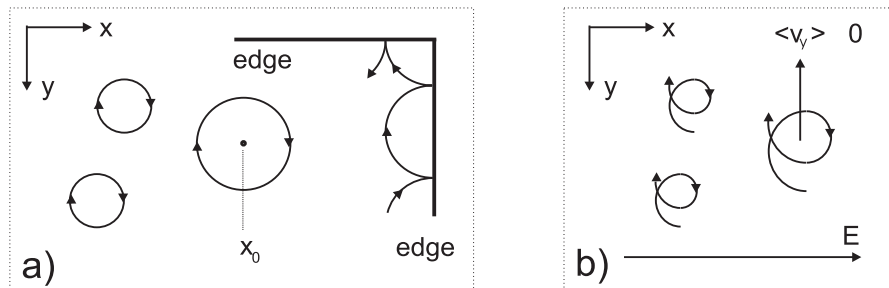


Fig. 1.3 a) The classical trajectories in the absence of a magnetic field. The cyclotron radius of the electrons is quantized. Only at the edges of the sample the electrons can propagate. b) The classical trajectories for an infinite 2DEG when an electric field  $E$  is applied along the  $x$ -axis. There is no current along the  $x$  axis, but all electrons propagate in the  $y$ -direction.

smaller the cyclotron radius, and the more electrons can be accommodated in the same level. For an infinitesimally small magnetic field, the Landau levels are so close to each other that they form the continuum of a free electron gas.

If an electric field is applied in the  $x$ -direction, i.e.  $E \neq 0$ , this simply shifts the eigenvalues without changing the structure of the energy spectrum. From the wavefunctions, we can calculate the mean values of the velocities

$$\langle v_y \rangle = \frac{1}{m} \int \psi_n^* \left( \frac{\hbar}{i} \frac{\partial}{\partial y} + \frac{eBx}{c} \right) \psi_n d\mathbf{r} = -\frac{cE}{B} \quad (1.11)$$

$$\langle v_x \rangle = \frac{1}{m} \int \psi_n^* \frac{\hbar}{i} \frac{\partial}{\partial x} \psi_n d\mathbf{r} = 0, \quad (1.12)$$

from which follows that a current flows in the  $y$ -direction  $j_y = -n_e e E c / B$ , and the current along the direction of the electric field is zero. This effect was discovered in 1879 by Edwin Hall,[27] and is therefore called the Hall effect. In mesoscopic physics, this effect can be described as follows: *if in addition to the uniform normal magnetic field there is also an electrostatic potential gradient directed in the plane of the electrons, their instantaneous center coordinates will drift perpendicular to these gradients.* As we will see further on, this is also true if the electrostatic potential changes abruptly, as in the case of electrostatic edges at the sample edge. From Fig. 1.3(a) one can see electron transport parallel to the edges; those states are called *edge states*. [10]

In many experiments, the applied electric field is so small (except at the edges), that its effect on the electron spectrum is negligible. Nevertheless, in a realistic sample, a limited number of imperfections cannot be avoided, and this results in a broadening of the density of states, which can be modeled as

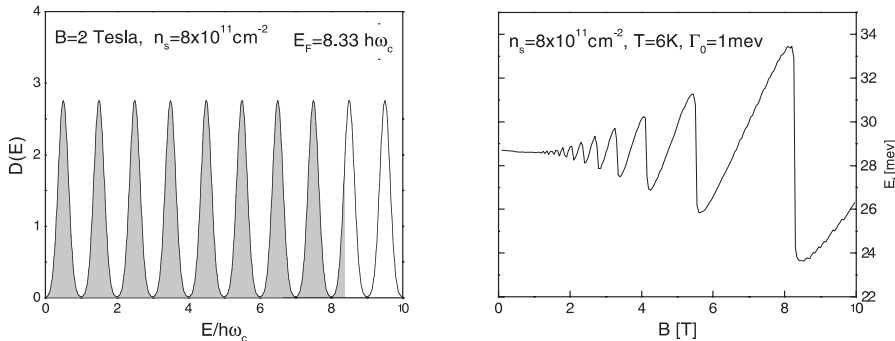


*Fig. 1.4* On the left: The density of states of a 2DEG subjected to a homogeneous magnetic field with strength  $B = 2$  T, and the subsequent filling of the states. On the right: the Fermi energy as a function of the magnetic field strength [taken from Ref. [32]].

follows

$$D(\epsilon) = 2 \sum_i \frac{eB}{h} \frac{\Gamma_0/\pi}{(\epsilon - \epsilon_i)^2 + \Gamma^2}, \quad (1.13)$$

where  $\Gamma_0$  is the broadening parameter which can be related to the scattering processes in the sample. In Fig. 1.4 (on the left) we show the density of states  $D(\epsilon)$  for magnetic field strength  $B = 2$  T. Note that the area under each of the peaks is constant and equal to the degeneracy of each Landau level which does not depend on the level index. This degeneracy is equal to the number of magnetic flux quanta per unit area  $eB/h$  multiplied by two to account for the two possible spin states of the electron. The Fermi energy in the 2DEG is determined by the condition of constant electron density  $n_e = \int d\epsilon D(\epsilon) f(\epsilon - \epsilon_F)$ , where  $f(\epsilon)$  is the Fermi distribution function. The Fermi energy oscillates as a function of the magnetic field (on the right). This oscillation in  $\epsilon_F(B)$  together with the oscillation in the density of states at the Fermi energy gives rise to an oscillatory behaviour in many properties of the 2DEG as function of the magnetic field, such as the Shubnikov-de Haas (SdH) oscillations in the magnetoresistance, as visible in Fig. 1.7(a) for  $B > 0.5$  T.

The behavior of electrons in macroscopically homogeneous magnetic fields has been used extensively to obtain experimental information on the properties of charge carriers, such as, for example, their density and the Fermi surface (through the SdH effect) and their mass (e.g., using cyclotron resonance).

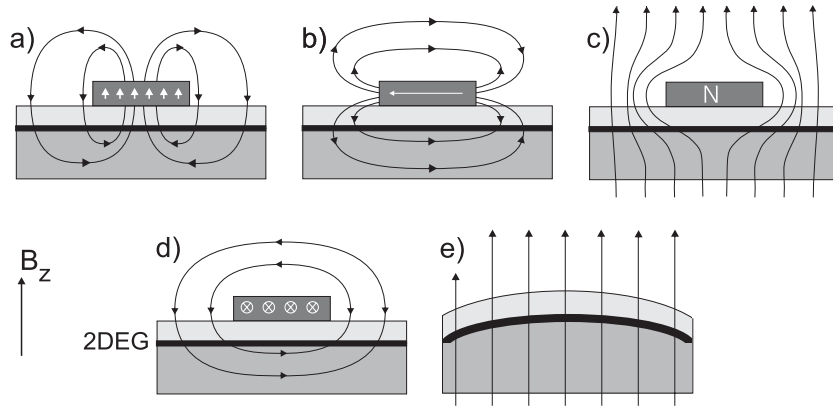


Fig. 1.5 The schematic sideview for the different methods of creating an inhomogeneous magnetic field in the 2DEG, i.e., by use of ferromagnetic material with a) perpendicular or b) in-plane magnetization, c) superconducting material, d) a current carrying wire and e) a nonplanar substrate

### 1.3 INFLUENCE OF INHOMOGENEOUS MAGNETIC FIELDS

#### 1.3.1 How to create them

Recent growth and patterning techniques (lithographic etching) have opened the door towards the creation of different magnetic field profiles. The methods of realizing these fields distributions are diverse, and are shown schematically in Fig. 1.5.

- **Integration of ferromagnetic materials (a,b)** can result in a locally large magnetic field in the 2DEG. The dimensions of the magnet can vary from clusters of tens of nanometers [2, 83, 96] up to larger stripes with any desirable shape.[11, 47, 59, 91] An external magnetic field is necessary to initially magnetize the magnet. The induced magnetic distribution can be controlled by the choice of the geometry and the dimensions of the magnet, distance to the 2DEG, magnetization of the material, etc.

The necessity of the application of a permanent background field depends on the hysteresis of the magnet. Hard magnets will retain their magnetization, even after the background magnetic field is switched off (see Fig. 1.6), soft magnets have low remanence and consequently have no magnetic memory. It should be mentioned that we talk about magnets and not about the material it is built of: the magnetic properties of materials on such a small scale can differ significantly from macroscopic samples. If the material is epitaxially grown, a magnetic anisotropy

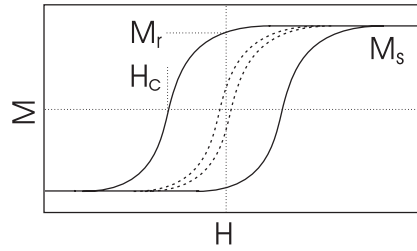


Fig. 1.6 Typical magnetization curve for a soft (dashed curve) and a hard (solid curve) ferromagnet.

arises since not all crystallographic directions are equal. If the magnetic material is sputter-deposited on the heterostructure, it is always polycrystalline (they have grains with sizes of order 5 nm), and consequently the crystalline anisotropy is less important. Nevertheless, due to reduced size, the shape of the magnet becomes important and also plays a role in the magnetic behaviour: this gives rise to a shape anisotropy. Handing a tool to study these parameters, i.e. creating a very sensitive nanomagnetometer, which would allow to probe magnetic properties on a nanometer scale, is one of the aims of this research.

In general, the shape anisotropy of the magnetic film (or the stripes) will force the magnetization in the plane of the film. Other mechanisms can be active that can lead to a magnetization vector perpendicular to the film. Out-of-plane magnetization has been realized in ultrathin layers of Fe on Ag or Cu; compounds such as MnAlGa, Co/Ni multilayers, and ultrathin MnGa films; and for the metastable  $\tau$ -MnAl phase, which can be grown epitaxially on GaAs/AlAs heterostructures using MBE.

- **Integration of superconducting materials (c)** can also result in a magnetic field inhomogeneity. When an external magnetic field is applied, the flux lines will be expelled from the superconductor due to the Meissner effect. If the latter is close enough, this will result in an inhomogeneous magnetic field in the 2DEG.[22, 23] For a type-II superconducting film, vortices will penetrate the superconductor and the 2DEG sees a very inhomogeneous magnetic field. The maximum temperature (magnetic field) is limited by the critical temperature (magnetic field) of the superconducting material.
- **Including current carrying wires (d)** Thanks to sophisticated lithographic techniques, it is possible to grow conducting wires close to, but electrically isolated from the 2DEG. Current through the wire will generate a radial magnetic field, which can penetrate the 2DEG, inducing locally an inhomogeneous magnetic field.

We will not encounter this remarkable property of a current carrying wire as creator of an inhomogeneous magnetic field in a 2DEG, but as generator of a background field needed to set the magnetization of a ferromagnetic strip.[16] We will elaborate on this further in last section of this introduction.

- **Growing the heterojunction on top of a pre-etched (nonplanar) substrate (e)** can also give rise to inhomogeneous magnetic fields in the interface, since only the perpendicular magnetic field component influences the transport. Because of this, a curved 2DEG experiences a nonuniform magnetic field, when an homogeneous external magnetic field is applied.[18, 19, 98]

It is clear that with this technique the magnetic field strength of the inhomogeneous profiles can exceed the strengths induced by the previous methods. These are limited by the magnetization of the ferromagnetic materials, or the critical  $B$ -value, above which the superconductor loses its fascinating property.

To calculate the magnetic field profiles produced by these methods in the 2DEG, one has to solve the corresponding Maxwell equations with the proper boundary conditions. Since we only consider static, time independent situations, the Maxwell equations we have to solve are

$$\nabla \cdot \mathbf{B} = 0, \quad \nabla \times \mathbf{H} = \frac{4\pi}{c} \mathbf{J},$$

with  $\mathbf{B}$  the magnetic induction,  $\mathbf{J}$  the current and  $\mathbf{H} = \mathbf{B}(\mathbf{r}) - 4\pi\mathbf{M}$  the magnetic field. The vector potential  $\mathbf{A}$  is defined as  $\mathbf{B} = \nabla \times \mathbf{A}$  and the magnetic potential as  $\mathbf{H} = -\nabla\phi_m$ . If superconducting materials are used to *corrupt* the homogeneous magnetic field, its effect corresponds to that of a current  $\mathbf{J} = ne^2/(mc)\mathbf{A}$ , which yields  $\nabla^2\mathbf{H} = 4\pi^2/(mc^2)\mathbf{H}$ . This equation has to be solved using the boundary condition  $B_n = -\partial\phi_m/\partial n = 0$  on the superconductor, and the condition that outside the superconductor  $\nabla^2\phi_m = 0$ .

The magnetic field profile in a curved magnetic field is just the  $B \cos(\alpha)$ , where  $B$  is the applied external field, and  $\alpha$  is the angle between the tangent of the 2DEG plain and the direction of the applied magnetic field.

In theoretical studies, one often includes an idealized profile. This is not solely to simplify the calculations, but also because this in a way generalizes its application: the same qualitative profiles can be created with different techniques. We will also show that this often simplifies the interpretation of the results. Nevertheless, sometimes it is appropriate to include the realistic profile. Therefore, depending on the kind of problem, we will insert a *realistic* or an *idealized* magnetic field distribution.

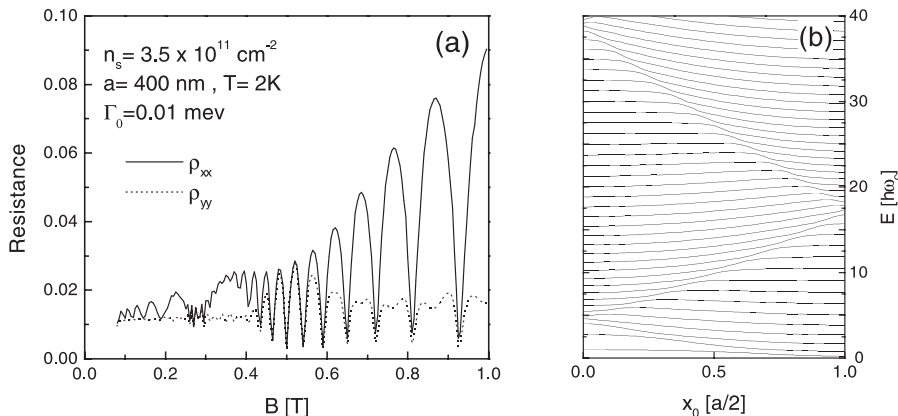


Fig. 1.7 a) The magnetoresistance in units of  $51.6 \Omega$  as a function of magnetic field at  $B_m = 0.07 \text{ T}$  showing the Weiss oscillations for  $B < 0.5 \text{ T}$  and SdH oscillations for  $B > 0.5 \text{ T}$ . b) The Landau levels evolving into Landau bands in the presence of a periodic modulation of the magnetic field where the modulation part and the uniform part have equal strengths [taken from Ref. [32]].

### 1.3.2 New physics?

Classically, electrons constrained in the  $xy$ -plane, subjected to a uniform magnetic field normal to the plane, circle around in closed orbits. We already showed that an electrostatic potential (i.e. electric field) in addition to the homogeneous magnetic field will cause the electron center coordinate to drift perpendicular to the gradient. A same effect can be obtained by applying a magnetic field gradient. The classical closed orbit is now broken, not by variation of the kinetic energy (circular velocity) due to a different electrostatic potential, but by changing locally the magnetic field strength.

**1.3.2.1 Periodic structures.** This is a basic feature behind the Weiss oscillations [48, 94]: when a 2DEG is subjected to a one dimensional periodic modulation of either electrostatic or magnetostatic origin, its magnetoresistance shows oscillatory behaviour as function of the magnetic field strength. This can be viewed in Fig. 1.7(a) for  $B < 0.5 \text{ T}$ . These oscillations were observed when a 2DEG in a homogeneous magnetic field is further perturbed by a weak 1D periodic magnetic field (period typically  $\approx 400 \text{ nm}$ ), produced by either ferromagnetic or superconducting materials grown on top of it. In contrast to the earlier mentioned SdH-oscillations these oscillations have a small temperature dependence and are most visible at low magnetic field strengths  $B < 1 \text{ T}$ . Both classical and quantum mechanical arguments have been used to interpret these oscillations. Classically, they are due to commensurability between two length scales: the cyclotron orbit at the Fermi energy, and the period of the magnetostatic (electrostatic) modulation.[6, 24] Quantum

mechanically, they can be explained as due to the lifting of the Landau level degeneracy and the oscillation of the Landau level width at the Fermi energy (see Fig. 1.7(b)). This gives rise to periodic oscillations of the drift velocity of the electron center coordinate as function of magnetic field with corresponding oscillations in the magnetoresistance.[71, 72]

When a periodic magnetic field modulation in two dimensions is applied to a 2DEG, the energy spectrum is also determined by fascinating commensurability effects. When the flux through a unit cell of the lattice is a rational multiple of the flux quantum, the resulting energy spectrum consists of broadened Landau levels, each having the same internal structure. This is called the Hofstadter butterfly,[30] when plotted versus the inverse flux ratio. The width of the Landau bands oscillates as a function of the Landau quantum number and the flux ratio. Although recently numerous experiments have applied themselves on observing this gap structure, no effects associated with the Hofstadter energy spectrum could be identified so far.

*1.3.2.2 Aperiodic structures.* In this thesis we will study inhomogeneous magnetic fields which are aperiodic. These result from just a single magnet/superconductor, or from an array which is randomly distributed.

In view of possible applications as magnetic field sensors, magnetic memory elements and magnetometers, a lot of research has been devoted to the influence of the stray field of a single magnetic strip (magnetic line) on a confined 2DEG (quantum wire, Hall bar).[25, 47, 91] Research has dealt with transport in the ballistic regime,[53, 67] where the magnetic distribution acts as a barrier, scattering ballistic electrons, and also on its effects at higher temperatures, in the diffusive regime.[34] Different configurations were investigated: where the stripe is along or perpendicular to the quantum wire axis, and where the magnetization of the strip is parallel or perpendicular to the 2DEG.

Deposition of a magnetic film can also give rise to a spatially random magnetic field. If one grows CoPd multilayers, onto a heterostructure containing a 2DEG, these multilayers have the property that maze-like domains patterns form ( $\approx 100 - 500$  nm) at certain points in the magnetization loops, magnetized perpendicular to the plane of the multilayers, and giving rise to a random inhomogeneous magnetic field of which the correlation length can be controlled by choice of growth parameters. The random field can be turned on or off by application of an external magnetic field.[81]

Another way to create an inhomogeneous magnetic field is by growing magnetic clusters above a 2DEG. This was done e.g. by Ye *et al.*[95] who grew a heterostructure with Dy-micromagnets on top of it. Dubonos *et al.*[17] even studied the effect of a single magnetic Dy-particle (with size down to  $\approx 70$  nm) on the transport properties of a close by Hall bar.

Geim [23] made use of a Hall cross to study the superconducting state of a type II-superconducting disk. Depending on the superconducting state, the

number of flux expelled from the disk –consequently not penetrating the Hall cross– changed, and hence the Hall and magnetoresistance changed. Indeed, Peeters and Li [66] simulated the ballistic motion of electrons in a mesoscopic Hall bar containing a local inhomogeneous magnetic field profile, and showed that it can be applied as *Hall magnetometer*. They found that in the regime of low magnetic fields, the Hall resistance is determined by the average magnetic field in the cross junction and is independent of the shape and the position of this profile in the junction. They found that the Hall resistance in the low magnetic field region is determined by the average magnetic field in the cross junction and is independent of the shape and the position of the profile in the junction.

Smith *et al.*[28, 86] grew a random distribution of superconducting lead grains on top of a heterojunction containing a 2DEG.

When a type-II superconducting film is grown on top of a 2DEG, vortices will penetrate the 2DEG creating magnetic scattering centers in the 2DEG. This experiment was carried out by Geim *et al.*, who grew a type II superconducting lead film above a 2DEG. If the external magnetic field is weak, below 100 G, the vortices will be well separated, and the 2DEG therefore sees a very inhomogeneous magnetic field. In the experiments conducted by Geim *et al.*[21] the flux pinning in the film was strong, resulting in a disordered distribution of flux vortices. In very clean films, the flux vortices will order in a periodic array, i.e. an Abrikosov lattice, and thereby create a periodic magnetic field in the 2DEG.

## 1.4 THEORETICAL APPROACH

The term *Mesoscopic physics* consists of the Greek words: *mesos*, which is *middle*, and *skopein*, which means *to look at*. Mesoscopic physics therefore covers the region between the microscopic and the macroscopic level. The crossover between these two regions is not abrupt, as most things in nature, which makes this regime very interesting.

We have a lot of quantum mechanical equations and approaches, and on the other hand we have classical equations. In mesoscopic physics one can butter one's bread on both sides. One has to start on quantum mechanical principles and calculate the problem quantum mechanically, but no more than necessary: as fast as nature allows it, one should try to make the leap to classical mechanics as an approximation, because this in general simplifies the problem considerably and enhances the understanding of the problem.

If we apply this to transport in mesoscopic systems, there are several length scales which can be used to characterize different regimes, ranging from the purely quantum mechanical to the classical regime.

The presence of imperfections in the conductor gives rise to the *elastic mean free path*  $\ell = v_F \tau$  with the Fermi velocity  $v_F$ . It is the only limiting

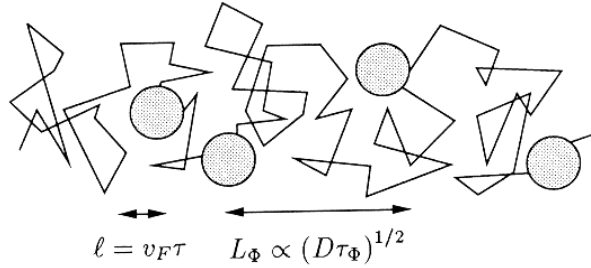


*Fig. 1.8* Diffusive motion of a particle in an impure conductor at a temperature close to absolute zero under the influence of impurity scattering (mean free path  $\ell = v_F \tau$ ), and rare phase randomizing scattering processes (shaded circles, the phase coherence length  $L_\phi$ ) [taken from Ref. [46]].

length for transport at  $T = 0$  and is independent of the temperature. The mean free time  $\tau$  has to be determined by quantum mechanical theory. It is very important to note here that *the elastic mean free path has nothing to do with the destruction of phase coherence*. In principle, the underlying impurity scattering can be exactly taken into account by diagonalizing the Hamiltonian of the electron in the presence of the impurity potential.

At finite temperatures, there are basically two additional limiting influences on the transport. First of all, the conductivity is an average over the states within an interval  $\Delta E \approx k_B T$  near the Fermi level. Since the phases of different eigenstates are completely independent, we expect a decay of the average correlation function on a time scale, which is usually interpreted as a temperature induced phase coherence time. On the other hand, interactions with other elementary excitations as phonons, lead to mixing of the one-electron states. These scatterings are in general inelastic and therefore lead to *phase coherence* with a temperature dependent characteristic time  $\tau_i(T)$  which is the mean free time between *inelastic* scattering events. If one assumes that at low temperatures phase randomizing processes are sufficiently rare in comparison with the mean free time due to the impurities one can determine a *phase coherence length* by assuming diffusive transport – due to impurity scattering – between two phase destroying scattering events  $L_\phi = \sqrt{D\tau_\phi(T)}$ . The phase coherence time  $\tau_\phi$  is the mean free time between two successive phase randomizing events. The diffusive constant  $D$  contains only the impurity scattering which does not destroy quantum coherence. The temperature dependence of  $L_\phi$  is determined by the nature of the contributing scattering processes and is presently a subject of research worldwide. The understanding is yet far from complete.

It is now easy to subdivide transport in mesoscopic structures, as is shown schematically in Fig. 1.9: when the dimensions of the system are smaller than the mean free path,  $L < \ell$ , and is comparable to the electron wave length,  $L \approx \lambda = 1/k_F$  transport is situated in the **quantum** regime. If the

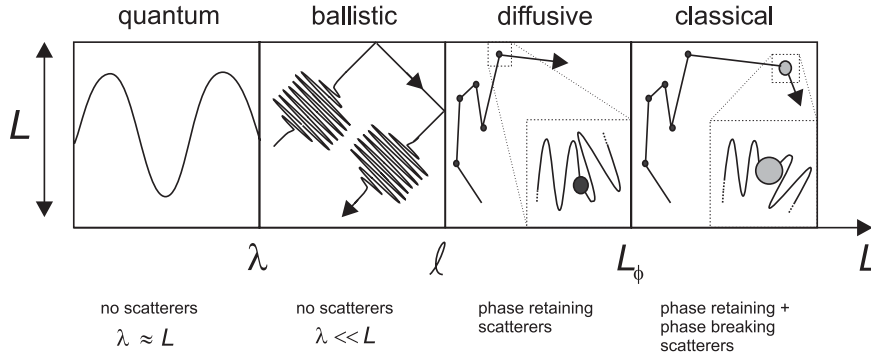


*Fig. 1.9* Classification of the different transport regimes in mesoscopic systems, where  $\lambda = 1/k_F$  denotes the electron wavelength at the Fermi energy,  $l$  is the mean free path and  $L_\phi$  is the phase coherence length. In the quantum and ballistic regime, only the wavefunctions are shown, in the diffusive and classical regime, the classical trajectory is shown, and the inset shows an enlargement of the respective scattering with the wavefunction retaining or losing its phase memory. Solid dots represent phase retaining scatterings, grey shaded circles correspond to rare phase randomizing scattering processes.

dimensions of the system are smaller than the mean free path,  $L < l$ , but the energy is such that the electron wavelength is larger than the system dimensions,  $L \gg \lambda$  we call the transport **ballistic**. Transport is nominated **diffusive** if the dimensions of the system are larger than the mean free path,  $L > l$  but smaller than the phase coherence length,  $L < L_\phi$ . If this last condition breaks, we finally arrive at the **classical** regime.

As being a thesis in mesoscopic physics, we have studied systems in all four regimes. In the following we will unfold the theories we will use in the next chapters, each in its own regime. Doing so, we will start with problems of quantum mechanical nature, and shifting up to the classical regime, we will make the jump towards classical physics, which then results in semi-classical theories.

## 1.5 QUANTUM REGIME

The first regime we study is the quantum regime. We consider the system to be ideal, i.e., the 2DEG is free of scatterers. The quantum mechanical approach is necessary when the Fermi-wavelength  $\lambda = 1/k_F$  is comparable to the dimensions of the system. We studied the quantum states in several systems in this regime: in a magnetic anti-dot (Chapter 2), which is a quasi zero magnetic field region in an otherwise constant magnetic field profile applied to an infinite 2DEG; in an infinite 2DEG under application of a 1D mag-

netic step discontinuity (Chapter 3); and in a quantum wire subjected to an inhomogeneous 1D magnetic field distribution (Chapter 5). We also studied the scattered states on a circular (magnetic) potential, for an infinite 2DEG (Chapter 4).

In the following we will briefly report on the textbook theories on which our work is based. We will start with the method of calculation of quantum states in an infinite 2DEG under application of a magnetic field profile which is invariant in one direction using Cartesian coordinates, then we will solve the Hamiltonian in polar coordinates, assuming a magnetic profile with cylindrical symmetry. The latter we will do for both the bound and the scattered states.

Next, we will study the effect of 1D confinement on the energy spectrum of the 2DEG and discuss the effect of a magnetic field in short. We will study transport through such a quantum wire, and extend this to transport in a multiprobe system, which is often used in experiments.

### 1.5.1 2DEG in a (in)homogeneous magnetic field in one direction

We consider an infinite 2DEG, in the absence of any scatterers and subjected to a (in)homogeneous magnetic field  $\mathbf{B} = \nabla \times \mathbf{A}$  in the  $x$ -direction. If we express all quantities in dimensionless units: magnetic field  $B \rightarrow B_0 B$ , the time  $t \rightarrow t/\omega_c$ , the coordinate  $\mathbf{r} \rightarrow l_B \mathbf{r}$ , and the energy  $\epsilon \rightarrow \hbar\omega_c \epsilon$ , with characteristic parameters  $\omega_c$  and  $l_B$  as defined earlier, the one-electron Hamiltonian for this system reads

$$H = \frac{1}{2m} \left( \mathbf{p} + \frac{e\mathbf{A}}{c} \right)^2. \quad (1.14)$$

As before, it is convenient to choose the Landau gauge,  $\mathbf{A} = (0, A_y(x), 0)$ , which allows us to choose a wavefunction which has a plane-wave dependence on the  $y$ -coordinate

$$\Psi(x, y) = \frac{1}{\sqrt{2\pi}} e^{-ik_y y} \phi(x). \quad (1.15)$$

Substituting Eq. (1.15) into Eq. (1.14), the Schrödinger equation becomes

$$\left[ -\frac{1}{2} \frac{d^2}{dx^2} + V_k(x) \right] \phi_{n,k}(x) = \epsilon_{n,k} \phi_{n,k}(x), \quad (1.16)$$

where it is the  $k$ -dependent effective potential

$$V_k(x) = \frac{1}{2} [A_y(x) + k]^2, \quad (1.17)$$

which contains the two-dimensionality of the problem. For some particular cases, it is possible to solve Eq. (1.16) analytically, but if the inhomogeneous profile is more complex, the wavefunction has to be solved numerically. We do this by use of a discretization procedure.

### 1.5.2 2DEG in a cylindrical symmetric (in)homogeneous magnetic field

Due to the cylindrical symmetry, it is preferable to use polar coordinates  $(r, \phi)$ . If we rescale the problem in the following way: length  $\mathbf{r} \rightarrow a\mathbf{r}$ , energy  $\epsilon \rightarrow (\hbar^2/ma^2)\epsilon$ , time  $t \rightarrow (ma^2/\hbar)t$  and magnetic field  $B \rightarrow (c\hbar/ea^2)B$ , the wavefunction can be written as

$$\Psi(r, \phi) = \frac{1}{\sqrt{2\pi}} e^{imr} R(r), \quad (1.18)$$

and we have to solve the following the 1D radial equation

$$\left\{ \frac{d^2}{dr^2} + \frac{1}{r} \frac{d}{dr} + 2[\epsilon - V_m(r)] \right\} R(r) = 0, \quad (1.19)$$

where the effective potential reads

$$V_m(r) = \frac{1}{2} \left[ A_\phi(r) + \frac{m}{r} \right]^2. \quad (1.20)$$

If we are looking for bound states, it is sufficient to solve this radial equation in order to obtain the desired wavefunction. Only, when the magnetic field strength at infinity  $r \rightarrow \infty$  is zero, no bound states are possible, electrons can only be quasi-bound, since it is energetically more favorable for an electron to be in the zero magnetic field region. Therefore one has to use another approach: scattering theory. Since we only consider circular scattering profiles, we restrict ourselves to partial wave scattering.

### 1.5.3 Scattering on a cylindrical symmetric magnetic profile

In this section we shall consider the electron scattering on a cylindrical symmetric (magnetic) profile within the framework of quantum theory.[82] The quantum nature of the electron radically alters the picture of the scattering process when the wavelength of the electron is comparable to, or longer than the diameter of the scattering profile. In the limit of very small electron wavelength, the scattering can essentially be described by the laws of geometrical optics, and thereby classical mechanics.

We have to solve Eq. (1.19), where  $\epsilon$  can now take all values, and is given by  $\epsilon = k^2/2$ . The scattering wavefunction has the same form as Eq. (1.18). We will assume that the scatterers are local perturbations, so that the effective potential satisfies

$$V_m(r \rightarrow \infty) = \frac{m^2}{2r^2}, \quad (1.21)$$

and at a large distance from the scatterer ( $r \rightarrow \infty$ ), the radial equation is the differential equation for the Bessel function of the first kind.

$$\left[ -\frac{1}{2r} \frac{d}{dr} r \frac{d}{dr} + \frac{m^2}{2r^2} - \frac{k^2}{2} \right] R_m(r) = 0, \quad (1.22)$$

with well known solutions

$$R_m(r) = a_m J_m(kr) + b_m Y_m(kr), \quad (1.23)$$

where  $J_m(x)$  and  $Y_m(x)$  are Bessel functions of the first kind. Again we will solve Eq. (1.19) numerically, now starting at  $r = 0$  with proper initial conditions for the wavefunction, until the asymptotic region is reached. This results in an  $m$ -dependent phase shift  $\delta_m$ , which describes the whole problem and enables us to calculate the scattering probability, as we will see further on.

In correspondence to 3D scattering theory, we can write the scattered wave as

$$\Psi(r, \phi) = \frac{1}{\sqrt{2\pi}} \left[ e^{i\mathbf{k}\mathbf{r}} + \frac{f(\phi)}{r^{1/2}} e^{ikr} \right] \quad (1.24)$$

with  $f(\phi)$  the scattering amplitude to be scattered over an angle  $\phi$ . To obtain the differential cross section, we may consider a large number of identically prepared particles all characterized by the wave function  $\exp(i\mathbf{k} \cdot \mathbf{r})/\sqrt{2\pi}$ . The number of incident particles crossing a plane perpendicular to the incident direction per unit area per unit time is denoted by the differential cross section, which is given by

$$\frac{d\sigma}{d\phi} = |f(\phi)|^2. \quad (1.25)$$

The total cross section then reads  $\sigma = \int_0^{2\pi} (d\sigma/d\phi) d\phi$ . We can write  $e^{i\mathbf{k}\mathbf{r}} = e^{ikr \cos \phi}$  as a series of Bessel functions

$$e^{ikr \cos \phi} = \sum_{m=-\infty}^{\infty} i^m e^{im\phi} J_m(kr). \quad (1.26)$$

The radial solution at  $r = \infty$ , given in (1.23), we can rewrite as

$$R_m(r \rightarrow \infty) = c_m [\cos \delta_m J_m(kr) - \sin \delta_m Y_m(kr)], \quad (1.27)$$

which, after insertion of the asymptotics [1]

$$J_m(x \rightarrow \infty) = \sqrt{\frac{2}{\pi x}} \cos \left[ x - \left(m + \frac{1}{2}\right) \frac{\pi}{2} \right], \quad (1.28)$$

$$Y_m(x \rightarrow \infty) = \sqrt{\frac{2}{\pi x}} \sin \left[ x - \left(m + \frac{1}{2}\right) \frac{\pi}{2} \right], \quad (1.29)$$

results in the following general solution in the  $r \rightarrow \infty$  limit

$$\Psi(r \rightarrow \infty, \phi) = \sum_{m=-\infty}^{\infty} e^{im\phi} c_m \sqrt{\frac{2}{\pi kr}} \cos \left[ kr - \left(m + \frac{1}{2}\right) \frac{\pi}{2} + \delta_m \right]. \quad (1.30)$$

Identification with Eq. (1.24)

$$\Psi(r \rightarrow \infty, \phi) = \sum_{m=-\infty}^{\infty} i^m e^{im\phi} \sqrt{\frac{2}{\pi k r}} \cos \left[ kr - \left(m + \frac{1}{2}\right) \frac{\pi}{2} \right] + \frac{f(\phi)}{r^{1/2}} e^{ikr}, \quad (1.31)$$

to the coefficients of  $e^{-ikr}$ , results into a solution for the coefficient

$$c_m = i^m e^{i\delta_m}. \quad (1.32)$$

Comparison of the coefficients of  $e^{ikr}$  after substitution of Eq. (1.32), leads to

$$f(\phi) = \sqrt{\frac{2i}{\pi k}} \sum_{m=-\infty}^{\infty} e^{im\phi} e^{-i\delta_m} \sin \delta_m. \quad (1.33)$$

It is clear that the phase shifts induced by the scattering center describe the whole problem, and enable us to calculate the differential cross section and study the quasi-bound states.

#### 1.5.4 A Quantum wire

An infinite 2DEG of course only exists in theory. The electrons are somehow confined, and the energy spectrum is not a continuum, even in the absence of a discretizing magnetic field. If the 2DEG electron gas is confined in one direction ( $x$ ), but electrons propagate freely along the other ( $y$ )-direction, one obtains a quantum wire. A lot of research has applied itself to transport through quantum wires.[9, 4, 14, 70, 92] We will study the system using Cartesian coordinates. The Hamiltonian for such a system reads

$$H = \frac{1}{2m} \left( \mathbf{p} + \frac{e}{c} \mathbf{A} \right)^2 + V(x), \quad (1.34)$$

where  $V(x)$  is the electrostatic confinement potential along  $x$ . If we choose the vector potential in the Landau gauge, the wavefunction can again be written as

$$\Psi_{n,k}(x, y) = \phi_n(x) e^{iky} \quad (1.35)$$

with corresponding energy  $\epsilon_n(k)$  and group velocity

$$v_{n,k} = \langle \Psi_{n,k} | \frac{1}{m} p_y + \frac{eBx}{c} | \Psi_{n,k} \rangle = \langle \Psi_{n,k} | \frac{\partial H}{\partial p_y} | \Psi_{n,k} \rangle = \frac{1}{\hbar} \frac{\partial \epsilon_n(k)}{\partial k}. \quad (1.36)$$

If the applied background field  $B = 0$ , the effective potential corresponds to the one of an electron in a 1D potential well. If we consider hard wall confinement, the energy spectrum is well known and quantized

$$\epsilon_n(k) = \epsilon_n + \frac{\hbar^2 k^2}{2m}, \quad (1.37)$$

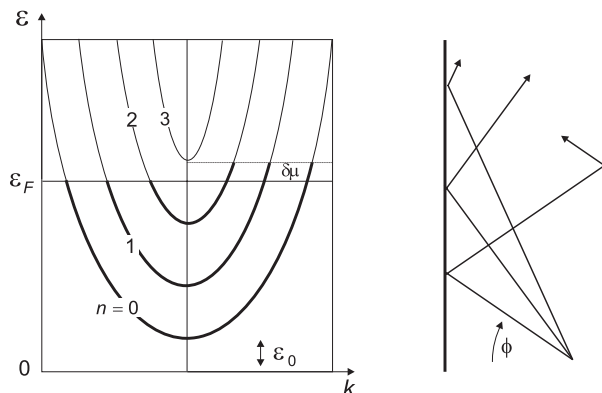


Fig. 1.10 a) The dispersion of an electron in a quantum wire. Only electrons with energy between  $\epsilon_F$  and  $\epsilon_F + \delta\mu$  contribute to the conductivity, b) the angles of the classical trajectories in a quantum wire are quantized. Each angle corresponds to a different channel.

which we plotted schematically in Fig. 1.10(a). The two-dimensionality of the problem is contained in the wavevector  $k$ . Although different channels have the same total (kinetic) energy, the group velocity (in the  $y$ -direction) differs, i.e.  $v_n(k) = \hbar k/m$ . This corresponds to the classical picture where the angles of the allowed trajectories are quantized, as is shown in Fig. 1.10(b).

If a magnetic field is applied, the energy spectrum will change dramatically. Because of the additional confinement imposed by the magnetic field, energy levels will shift away from each other, and less channels will intersect the Fermi energy level. Also the velocity of the states will change, as the magnetic field increases, until the first Landau level exceeds the Fermi-energy of the system, and there are no states occupied anymore in the wire. Application of a background magnetic field, therefore has a big impact on the electronic properties of a quantum wire.

Classically, the presence of the external magnetic field is contained in the formation of skipping orbits, circular orbits which propagate on a circular orbit bouncing against the hard wall, as was earlier pointed out in Fig. 1.3(a).

**1.5.4.1 Transport in a single wire.** An electronic device is typically connected to two contacts across which a voltage is applied. Each of these contacts launches a steady stream of electrons into the device, of which a fraction is transmitted to the other contact. At equilibrium both contacts have the same electrochemical potential, the current  $I_{1 \rightarrow 2}$ , transmitted from contact 2 to contact 1, equals  $I_{2 \rightarrow 1}$ . An applied voltage shifts the local chemical potential  $\mu_1 = -eV_1 + \epsilon_F$  in contact 1 with respect to the local chemical potential  $\mu_2 = -eV_2 + \epsilon_F$  in contact 2, making  $I_{1 \rightarrow 2}$  different from  $I_{2 \rightarrow 1}$  and causing a

net current flow through the device

$$j = \sum_{n=1}^N j_n, \quad (1.38)$$

where  $N$  is the number of channels at the Fermi energy, and  $j_n$  is the current of each particular channel which is

$$j_n = 2e \int_{\epsilon_F}^{\epsilon_F + \delta\mu} d\epsilon v_n D_n(\epsilon) = \frac{2e}{h} \delta\mu, \quad (1.39)$$

since  $D_n(\epsilon) = [2\pi d\epsilon/dk]^{-1}$  is the density of states in 1D. So even for an ideal conductor, we obtain a conductance which is finite, even though no scatterers are present. If the channels are not ideal, a part of the injected current can be scattered back. Hence, we introduce  $T_n$ , the fraction of the current in channel  $n$  which is passed through, such that the total current is given by

$$j = \frac{2e}{h} \sum_{n=1}^N T_n \delta\mu.$$

**1.5.4.2 Transport in a multiprobe system.** Considering transport in multiprobe systems is not as easy as when only two probes are present, yet these configurations are very important when it comes to experimental measurements. In order to generalize the situation to the multiprobe situation, we introduce  $R_{ii}$ , the fraction of the current which is reflected to probe  $i$ , and  $T_{12}$ , the fraction of the current in probe 1 coming from probe 2. Current conservation requires

$$R_{jj} + \sum_{i \neq j} T_{ij} = N_j, \quad (1.40)$$

hence the current in probe  $i$  equals

$$I_i = \frac{e}{h} [(N - R_{ii})\mu_i - \sum_{j \neq i} T_{ij}\mu_j], \quad (1.41)$$

which is the multiprobe Landauer-Büttiker formula. The resistance is given by  $R_{ij,kl} = (\mu_k - \mu_l)/eI_{ij}$ .

In view of chapter 5, we will calculate the four-terminal resistance  $R_{12,34}$  when probes 3 and 4 are weakly coupled. The coupled equations which have to be solved are

$$\begin{pmatrix} I_1 \\ I_2 \\ I_3 \\ I_4 \end{pmatrix} = \begin{pmatrix} T_{11} & T_{12} & T_{13} & T_{14} \\ T_{21} & T_{22} & T_{23} & T_{24} \\ T_{31} & T_{32} & T_{33} & T_{34} \\ T_{41} & T_{42} & T_{43} & T_{44} \end{pmatrix} \begin{pmatrix} \mu_1 \\ \mu_2 \\ \mu_3 \\ \mu_4 \end{pmatrix}, \quad (1.42)$$

where we defined  $-T_{ii} \equiv N_i - R_{ii} = \sum_{j \neq i} T_{ij}$ . Instead of solving this matrix equation, we will make use of the fact that probes 3 and 4 are weakly

coupled with the conductor. They *measure* the voltage and consequently no net current flows through probe 3 and 4. Therefore, we consider the situation as being two three-terminal configurations. Hence we obtain the chemical potential in probe 3 and analog in probe 4

$$\mu_3 = \frac{T_{31}\mu_1 + T_{32}\mu_2}{T_{31} + T_{32}} \quad \mu_4 = \frac{T_{41}\mu_1 + T_{42}\mu_2}{T_{41} + T_{42}}. \quad (1.43)$$

If we disregard the effect of probe 3 and 4 to first order, we find  $I = I_1 = -I_2 = \frac{e}{h}T(\mu_1 - \mu_2)$  with  $T = T_{12} = T_{21}$  and the four terminal resistance equals

$$R_{12,34} = \frac{\mu_3 - \mu_4}{eI} = \frac{h}{e^2} \frac{1}{T} \frac{T_{31}T_{42} - T_{32}T_{41}}{(T_{31} + T_{32})(T_{41} + T_{42})}. \quad (1.44)$$

This formula can be used to calculate the Hall resistance, or the resistance of the conductor between probe 3 and 4, i.e., without the contact resistance.

## 1.6 BALLISTIC REGIME

This region holds, when the electron energy is high enough, such that (a) electron trajectories are classical to a good approximation – which means that the Fermi wavelength  $\lambda = 1/k_F$  is smaller than the dimensions of the system, and external fields vary slowly with respect to  $\lambda$  – and (b) the scattering length due to impurities, thermal scattering etc. is larger than the dimensions of the system, and therefore does not dominate the transport.

In this regime, one can make use of the Boltzmann transport equation,[44] which reads

$$\frac{\partial f}{\partial t} = -\mathbf{v} \cdot \nabla_{\mathbf{r}} f - \frac{1}{\hbar} \mathbf{F} \cdot \nabla_{\mathbf{k}} f + \int_{V_{\mathbf{k}}} w(\mathbf{k}, \mathbf{k}') [f(\mathbf{r}, \mathbf{k}') - f(\mathbf{r}, \mathbf{k})] \frac{d\mathbf{k}}{(2\pi)^2},$$

where  $f(\mathbf{r}, \mathbf{k}, t) \frac{d\mathbf{k}}{(2\pi)^2}$  is the number of states occupied in an elementary unit of Fermi surface and  $w(\mathbf{k}, \mathbf{k}')$  is the probability for an electron to transit from state  $|\mathbf{r}, \mathbf{k}\rangle$  to  $|\mathbf{r}', \mathbf{k}'\rangle$ .

The integral of Eq. (1.6) contains the function we want to determine. Hence, it is a integral-differential equation, of which we don't know the general solution. It describes that in a stationary case, the variation of the distribution function under influence of an externally applied field and of the motion of the particles is compensated by the scattering on the local perturbations (through  $w(\mathbf{k}, \mathbf{k}')$ ) and impurity scattering  $[\partial f / \partial t = -(f - f_0) / \tau]$ .

As a consequence, there are two ways of including the random magnetic field in the Boltzmann equation: (1) one can treat the inhomogeneous magnetic field as an ordinary external field in the driving force term of the Boltzmann equation. This approach is only justified if the dimension of the perturbation  $a \gg \lambda$ , which is satisfied in most experiments. (2) Or one can view the ‘‘impurities’’ as scatterers, i.e., include them in the scattering term on the

right hand side. This can always be done, even when the correlation length  $a$  of the modulation is much greater than  $\lambda$ . In Chapter 4 we will choose for the latter approach and consider the random magnetic field as scattering centers. We will consider the ordinary impurity scattering to be negligible, i.e.,  $\tau \approx \infty$ .

To conclude, this kinetic equation is only valid if: (a) application of external forces does not modify the energy spectrum of the electron in the crystal. This imposes a limit to the intensity of the applied fields. And (b) the kinetic equation is a quasi-classical equation, and therefore cannot be used to study processes of very short duration, taking place in very small volumes, since this results in an uncertainty on the energy values which is too large.

## 1.7 DIFFUSIVE REGIME

In this regime the transport is influenced by scattering on imperfections, but without destruction of the phase coherence. We will only consider transport in this regime in Chapter 5, where we calculate the conductivity of a quantum wire quantum mechanically, and afterwards introduce the effects of scatterings by assuming the transmission probability of each channel  $T_n$  to be proportional to its velocity parallel with the wire, i.e.  $T_n \sim v_y(n)\tau/L_y$ , where  $\tau$  is the mean free time and  $L_y$  is the length of the quantum wire.

In general, conductivity in a 1D conductor in the diffusive regime can be written as

$$\sigma_{1D} = \frac{e^2}{L_y} \sum_{n,k} v_n^2(k) \tau(\epsilon) \left( -\frac{\partial f(T)}{\partial \epsilon} \right), \quad (1.45)$$

where  $f(T)$  is the Fermi-Dirac distribution function at temperature  $T$  and  $n$  runs over all the conducting subbands.

## 1.8 CLASSICAL REGIME

If the phase coherence length  $L_\phi$  is larger than the dimensions of the sample, we can use classical equations to study the transport in a 2DEG. We will do this in Chapter 6 and 7, where we calculate the Hall resistance of a Hall bar, subjected to a spatially dependent magnetic field, at higher temperatures.

Classically, the equation of motion is given by  $\mathbf{F} = m\mathbf{a}$ , which results in

$$\frac{d(m\mathbf{v})}{dt} + \frac{m\mathbf{v}}{\tau} = -e(\mathbf{E} + \mathbf{v} \times \mathbf{B}), \quad (1.46)$$

where  $t$  is time,  $m\mathbf{v}$  is momentum, and  $\tau$  is introduced as an average momentum relaxation time. The second term describes the friction which the carriers experience on drifting through the 2DEG. In a steady state situation, the time derivative is zero, and if a static magnetic field is applied in the

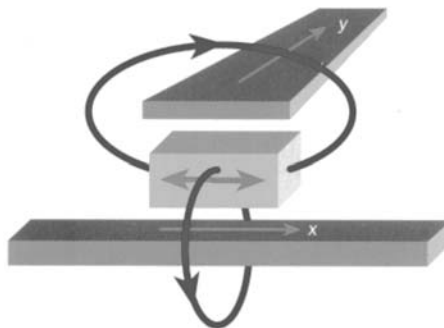


*Fig. 1.11* In MRAM the magnetic moment of a material is used to store data. Data can be written to the material by sending an electric current down conductors that pass nearby. In this case, the magnetic field produced by current  $x$  puts the magnetization into an intermediate state, and current  $y$  then triggers the magnetic moment to move to a particular orientation. Two currents are needed so that a specific magnetic element in an array of many can be written. The stored date can then be read electronically by measuring the material's magnetic moment [taken from Ref. [16]].

$z$ -direction, the drift velocities respectively in the  $x$  and  $y$ -direction read

$$v_x = -\frac{e\tau}{m}E_x - \omega_c\tau v_y ; \quad v_y = -\frac{e\tau}{m}E_y + \omega_c\tau v_x,$$

where  $\omega_c = eB/mc$  is the cyclotron frequency as discussed before. Using  $\mathbf{j} = \sigma\mathbf{E}$ , and  $\mathbf{j} = nev$ , it is straightforward to arrive at

$$\begin{pmatrix} j_x \\ j_y \end{pmatrix} = \begin{pmatrix} \sigma_{xx} & \sigma_{xy} \\ \sigma_{yx} & \sigma_{yy} \end{pmatrix} \begin{pmatrix} E_x \\ E_y \end{pmatrix} \quad (1.47)$$

$$= \frac{\sigma_0}{1 + (\omega_c\tau)^2} \begin{pmatrix} 1 & -\omega_c\tau \\ \omega_c\tau & 1 \end{pmatrix} \begin{pmatrix} E_x \\ E_y \end{pmatrix}, \quad (1.48)$$

where  $\sigma_0 = ne^2\tau/m$  is the zero magnetic field Drude conductivity,  $\sigma$  is a spatially dependent tensor, which depends on both the mean free time  $\tau$  and on the magnetic field strength  $\omega_c(\mathbf{r})$  in each point of the 2DEG.

## 1.9 APPLICATIONS

In the following we will discuss two applications, which were the driving forces behind the development in this area. They will prove that problems dealt with in this thesis are not only interesting from a fundamental point of view, but might also put forward new possible devices, or determine the feasibility of others.

### 1.9.1 Magnetic Random Access Memory device

Magnetic Random Access Memory (MRAM) devices would use magnetic materials – rather than semiconductor transistors and capacitors found in conventional dynamic random access memory (DRAM) – to store information. The big advantage is that the stored data is non-volatile, that it still persists for many, many years, even if the power is switched off. This is important in present-day technology, if we think about smart cards, cellular phones, and other portable technologies, which one wants to consume as less power as possible. Moreover it would be a more durable and reliable alternative than other possible non-volatile memory chips.

The basic write-function for the MRAM is shown in Fig. 1.11. The magnetic moment of a magnetic material is used to store data: left and right correspond respectively to  $0$  or  $1$ . Data can be written to the material by sending an electric current through conductors placed nearby the magnetic element. In this case, the magnetic field produced by current  $x$  puts the magnetization into an intermediate state, and current  $y$  then triggers the magnetic moment to move to a particular orientation. Two currents are needed so that a specific magnetic element in an array of many can be written.

So far the writing function of MRAM. Reading out the data, determining the state of the magnetic material, is a tougher job, which leaves the door open for different design possibilities, operating with different physics.

Well known are the two-terminal devices, who contain two magnetic layers with magnetizations that can point either in the same or opposite directions. For example, parallel could represent a  $1$ , while antiparallel magnetizations could represent a  $0$ . The basic operation is based on the fact that the resistance through two parallel layers differs from when the magnetic moments are directed in opposite directions.

These systems exploit the spin, rather than the charge of the electron. Yet, it is well known that the behaviour of the charge of an electron depends on the presence of a magnetic field, and therefore could -in theory- be used to determine the state of the magnetic material. Monzon *et al.*[54] and Johnson *et al.*[38, 39] presented results on a new magnetoelectronic device, the hybrid Hall effect device and demonstrated that this is indeed possible.

They grew a ferromagnetic stripe on top of a Hall cross, as shown in Fig. 1.12. The information, i.e., the state of the magnetic moment, can be *read* electronically thanks to the effect of the fringe fields of the magnet on the charge carriers in the Hall bar. Currently, one is trying to commercialize such a system, but the interest is somewhat tempered, since storage densities are likely to be higher with two-terminal devices.

### 1.9.2 Magnetic field sensor

It was already known that Hall bars work well as magnetic field sensors. Indeed, the Hall cross devices are already used for magnetic imaging in scanning

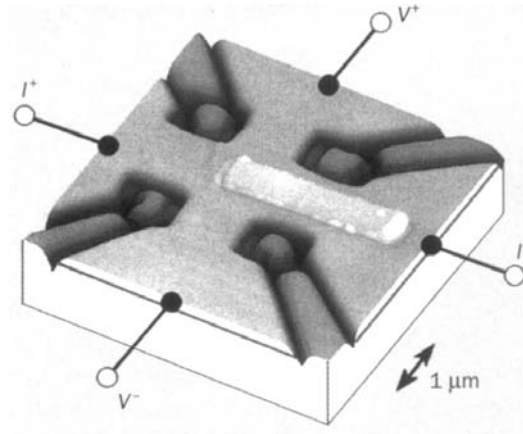


Fig. 1.12 An atomic force micrograph of a semiconducting indium arsenide Hall cross with a magnetic strip made from a nickel-iron alloy on top of it [taken from Ref. [16]].

Hall probe microscopes. Addition of a magnetic component as in the device of Johnson *et al.* and Monzon *et al.* might result in more sensitive magnetic field sensors. If one chooses the proper magnetic material, then a small applied background field – which cannot be measured with the ordinary Hall cross – magnetizes the magnetic film, and result locally in a much larger magnetic field, which on its turn can be measured. If one chooses a magnetic material with a steep linear magnetization loop with very little hysteresis, this might be used as a sensitive Hall magnetic field sensors.

### 1.9.3 Magnetometer

One can also study the electron transport in the 2DEG subjected to an inhomogeneous magnetic field profile, to characterize this profile, and consequently the magnetic material that creates this magnetic field profile. Even if the magnetic material is too small to study with standard magnetometry! In order to extract information on the magnetic field inhomogeneity, it is necessary to know the effects of different magnetic field profiles on the 2DEG. This allows one to study the magnetic properties of ultrasmall magnetic particles which might be of importance in future applications.

## 1.10 ORGANIZATION OF THE THESIS

Next chapters reveal the work I have done in the past four years. All chapters were published in scientific journals, more or less in the same form. As was done in this introduction, we start with the problems situated in the quantum

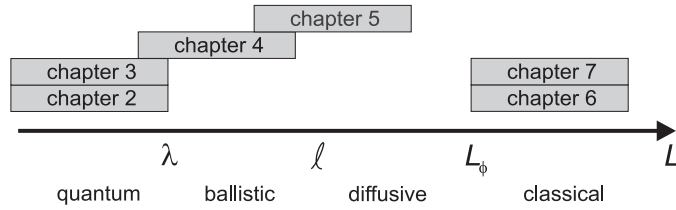


Fig. 1.13 Schematical overview of the thesis: different chapters as situated in the different mesoscopic transport regimes.

regime. In Chapter 2 we study the electron bound states in a magnetic antidot, which is a low magnetic field region in an otherwise constant magnetic field. In Chapter 3 we will study snake orbits, electron bound states which arise when a steplike magnetic field is applied in one ( $x$ ) direction. These states propagate parallel to the interface and have the quality to enhance the conductivity locally. Later on, in Chapter 5, we will study the effects of these snake orbits in a realistic experimental situation, where four-terminal measurements were performed on a quantum wire subjected to the (steplike) magnetic field distribution created by a nearby *magnetic line*. In order to explain recent experimental result we will have to include phase retaining collisions, and hence make the leap to the diffusive transport regime.

But first, in Chapter 4, we will study transport in the ballistic regime through a 2DEG subjected to a random array of magnetic profiles, as created by a magnetic disk with perpendicular magnetization. To do this we will first study the pure quantum case of scattering on a single magnetic profile, and then introduce this scattering process into the Boltzmann equation.

In the classical transport regime, we will study a novel magneto-electronic device with possible device applications as a non-volatile memory element. This device has good output values, even at room temperature. In Chapter 6 we show that our theoretical approach works well to understand the operation of this device, in Chapter 7 we study the temperature dependence of this device, and go beyond experimental measurements, in search for its optimal parameters.



# 2

---

## Quantum states in a magnetic anti-dot

*We study a new system in which electrons are confined in two dimensions by a non homogeneous magnetic field. The system consists of a heterostructure with on top of it a superconducting disk. We show that in this system electrons can be confined into a dot region. This magnetic anti-dot has the interesting property that the filling of the dot is a discrete function of the magnetic field. For some of the bound states the circulating electron current inside and outside the anti-dot can be in opposite direction. Such states exhibit a diamagnetic to paramagnetic transition with increasing magnetic field. The absorption spectrum consists of many peaks, some of which violate Kohn's theorem, which is due to the coupling of the center of mass motion with the other degrees of freedom.*

---

The results presented in this chapter were published as:

- J. Reijniers, F. M. Peeters, and A. Matulis, Phys. Rev. B **59**, 2817 (1999).

## 2.1 INTRODUCTION

Quantum dots have been the subject of both theoretical and experimental research in recent years.[36] They have been successfully created experimentally by applying lithographic and etching techniques to impose a lateral structure onto an otherwise two-dimensional electron system. These structures introduce electrostatic potentials in the plane of the two-dimensional electron gas (2DEG), which confine the electrons to a dot region. The energy levels of electrons in such a quantum dot are fully quantized like in an atom, and therefore are also referred to as *artificial atoms*. In such electrically confined quantum dots the confinement potential can well be represented by a parabolic potential.

In the present paper we study a new quantum dot system which is different from the usual quantum dot system: 1) the electrons are confined magnetically, 2) the confinement potential is inherently non-parabolic, and 3) the dot contains a finite number of electrons where the filling of the dot is a discrete function of the strength of the confinement (magnetic field).

This *magnetic anti-dot* can be realized [23] by depositing a superconducting disk on top of a 2DEG. When a homogeneous magnetic field is applied perpendicular to the 2DEG, the magnetic flux lines are expelled from the superconducting disk due to the Meissner effect, which results in an inhomogeneous magnetic field profile in the 2DEG. Note that this problem is related to the problem of type II superconductors on a heterostructure, where flux lines penetrate the 2DEG.[8] Between the flux lines regions of zero magnetic field are present. Here we have the inverse situation in which we have a uniform magnetic field except for a local dot-like region where there is no magnetic field present. Bound states are now possible in the zero magnetic field region.

Such a system was discussed by Peeters *et al.* in Ref. [68] where preliminary results were presented for the energy levels of such a magnetic anti-dot. Here we elaborate on this system and give a more detailed and complete study of the bound states of such a system and calculate also other properties of this system. In Ref. [66] the Hall and bend resistance resulting from such a system was discussed in the ballistic regime and in Ref. [35] the diffusive transport of such a magnetic anti-dot placed on top of a Hall bar was studied.

Solimany *et al.*[87] studied a limiting case of the present system in which the magnetic field was  $B(\rho) = B_a \theta(\rho - a)$  and they solved the classical and quantum mechanical equations for a magnetically confined quantum dot, and recently Sim *et al.*[84] investigated the formation of magnetic edge states along with the corresponding classical trajectories. Mallon and Maksym [50] generalized the above works to the case of two electrons. Although the above groups referred to this theoretical system as a magnetic dot, we think the name ‘magnetic anti-dot’ is more appropriate in this case. Here we start from the experimental realizable system, i.e. a superconducting disk on top of a 2DEG, and calculate in Sec. II the non-homogeneous magnetic field profile

induced in the 2DEG. We find that the magnetic field profile is different from the one assumed in Refs. [87] and [84]. In Sec. III the energy spectrum of electrons in the 2DEG near this magnetic field profile is calculated and compared with those of two circular model magnetic anti-dot systems. The filling of the magnetic anti-dot is calculated as function of the strength of the confinement. In Sec. IV we discuss the electron probability current and the induced magnetic moment. The optical absorption spectrum, i.e. frequencies and oscillator strengths, are obtained in Sec. V. A summary of our results and the conclusions are presented in Sec. VI.

## 2.2 MAGNETIC FIELD PROFILE

The system we have in mind is shown schematically in the inset of Fig. 2.1(a). We have a high mobility heterostructure with on top of it a superconducting disk placed in a homogeneous applied magnetic field  $\mathbf{B} = (0, 0, B_a)$ . For convenience, we consider a very thin superconducting disk which is perpendicular to the magnetic field and a distance  $z$ -above the 2DEG. Because of the symmetry of the system, we use cylindrical coordinates  $(\rho, \varphi, z)$  and measure all lengths in units of the disk radius  $a$ . We solve the following magnetostatic equations outside the disk

$$\begin{aligned}\nabla \cdot \mathbf{B} &= 0, \\ \nabla \times \mathbf{B} &= 0,\end{aligned}\tag{2.1}$$

with the conditions that  $B_\varphi = 0$  due to symmetry considerations, and  $B_z|_{\rho \leq 1} = 0$  on the disk surface ( $z=0$ ).

This problem is equivalent to the problem of liquid flow around a disk and was solved in Ref. [55]. There the *oblate spheroidal coordinates*  $\rho = \sqrt{(\xi^2 + 1)(1 - \eta^2)}$ ,  $\varphi$  and  $z = \xi\eta$  were introduced, where  $0 < \xi < \infty$ ,  $0 < \eta < 1$  and  $0 < \varphi < 2\pi$  which have the corresponding scale factors  $h_\xi = \sqrt{(\xi^2 + \eta^2)/(\xi^2 + 1)}$ ,  $h_\eta = \sqrt{(\xi^2 + \eta^2)/(1 - \eta^2)}$ ,  $h_\varphi = \sqrt{(\xi^2 + 1)(1 - \eta^2)}$ . The surface  $\xi = 0$  is a disk of radius 1 in the  $xy$ -plane with center at the origin. According to that solution, the magnetic field under such an infinitesimal thin disk can be represented as  $\mathbf{B} = -\nabla\Phi$  where

$$\Phi(\xi, \eta) = -B_a\eta \left\{ \xi + \frac{2}{\pi} \left[ 1 - \xi \tan^{-1} \left( \frac{1}{\xi} \right) \right] \right\}.\tag{2.2}$$

Using cylindric symmetry and  $\mathbf{B} = \nabla \times \mathbf{A}$ , we arrive at the single non zero component of the vector potential

$$A_\varphi(\xi, \eta) = \frac{B_a\rho}{2} \left\{ 1 + \frac{2}{\pi} \left[ \frac{\xi}{1 + \xi^2} - \tan^{-1} \left( \frac{1}{\xi} \right) \right] \right\},\tag{2.3}$$

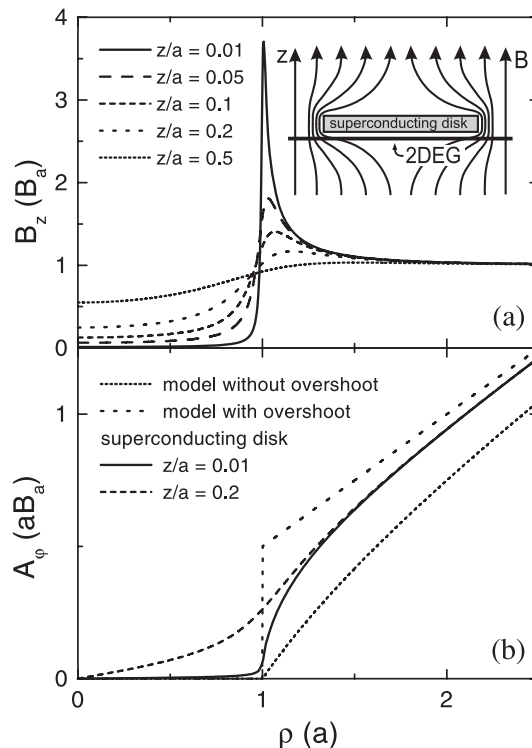


*Fig. 2.1* (a) The calculated magnetic field profile in the 2DEG plotted as function of the radial distance from the center  $\rho$  of the dot for different values of  $z$ , the distance of the disk above the 2DEG. The inset is a side view of the experimental configuration we have in mind. (b) The vector potential profile in the 2DEG plotted as function of the radial distance from the center  $\rho$  of the dot for the model systems without magnetic overshoot (dashed curve), with overshoot (dotted curve) and for the superconducting disk case with  $z/a = 0.01$  (solid curve) and  $z/a = 0.2$  (long dashed curve).

from which we obtain the perpendicular component of the magnetic field profile (or from Eq. (2.2) using  $\mathbf{B} = -\nabla\Phi$ )

$$B_z(\xi, \eta) = \frac{2A_\varphi}{\rho} + \frac{2B_a}{\pi} \frac{\xi(1 - \eta^2)}{(1 + \xi^2)(\xi^2 + \eta^2)}. \quad (2.4)$$

These results can be easily converted back to the cylindrical coordinate system  $(\rho, \varphi, z)$  by inserting  $\xi^2 = (1/2)[\sqrt{(r^2 - 1)^2 + 4z^2} + (r^2 - 1)]$  and  $\eta^2 = (1/2)[\sqrt{(r^2 - 1)^2 + 4z^2} - (r^2 - 1)]$  with  $r^2 = \rho^2 + z^2$  in the above equations.

The resulting magnetic field profile is shown in Fig. 2.1(a) for different values of the distance ( $z$ ) between the 2DEG and the superconducting disk. Notice that the magnetic field under the disk is very small due to the Meissner effect, while far from the disk it becomes equal to the external magnetic field strength  $B_a$ . At the edge of the disk there is an overshoot of the magnetic field

strength, which becomes larger with decreasing value of  $z$ . When the 2DEG is further away from the superconducting disk, there is almost no overshoot and  $B_z$  gradually increases away from the center. Notice that in the latter case the magnetic field is nonzero and consequently the model systems of Ref. [87] and Ref. [84] cannot be realized using a thin superconducting disk.

Before discussing the electron states in such a magnetic field profile, we will first consider two model systems which correspond to two extreme situations, but which contain the essential physics of the problem. The two models we consider are defined by the following profiles: 1)  $B_z(\rho) = B_a\theta(\rho - 1)$  with corresponding vector potential  $A_\varphi(\rho) = [B_a(\rho - 1/\rho)/2]\theta(\rho - 1)$ , and 2)  $A_\varphi = (B_a\rho/2)\theta(\rho - 1)$ , which results into a magnetic field profile with a delta function overshoot  $B_z = B_a\theta(\rho - 1) + (B_a\rho/2)\delta(\rho - 1)$ . The first model was used as the magnetic field profile in the magnetic anti-dot of the previous papers [35, 66, 68, 84, 87]. The second model contains a magnetic overshoot at the edge of the magnetic dot (see also Ref. [68]), which models the real system for  $z/a \ll 1$ . This overshoot is due to the de-magnetization effects of the superconducting disk. The vector potential profile of these two models is shown in Fig. 2.1(b) together with the one resulting from the superconducting disk for two different values of the set back distance  $z$ .

### 2.3 THE ENERGY SPECTRUM

In order to calculate the wavefunctions and their corresponding energy, we have to insert the expression for the spatial dependent vector potential ( $\mathbf{A}$ ) into the momentum operator  $\mathbf{p} \rightarrow \mathbf{p} + (e/c)\mathbf{A}$  which results in the Schrödinger equation:  $-(1/2m_e)[\hbar\Delta + (ie/c)\mathbf{A}(\mathbf{r})]^2\Psi(\mathbf{r}) = E\Psi(\mathbf{r})$ . Due to the cylindrical symmetry of the problem, the wave function can be written as

$$\Psi(\rho, \varphi) = \frac{1}{\sqrt{2\pi}} e^{im\varphi} R(\rho), \quad (2.5)$$

and the problem reduces to solving the 1D radial equation

$$\left\{ \frac{d^2}{d\rho^2} + \frac{1}{\rho} \frac{d}{d\rho} + 2[E - V(\rho)] \right\} R(\rho) = 0, \quad (2.6)$$

where the effective potential reads

$$V(\rho) = \frac{1}{2} \left( A_\varphi(\rho) + \frac{m}{\rho} \right)^2. \quad (2.7)$$

We solved this eigenvalue problem numerically, using the Newton iteration technique and subjecting the solution to the following boundary conditions:  $R(\rho \rightarrow 0) = \rho^{|m|}$  and  $R(\rho \rightarrow \infty) = 0$ .

The numerical results for the energy spectrum are shown in Fig. 2.2(a) for the model without overshoot, in Fig. 2.2(b) for the model with overshoot and

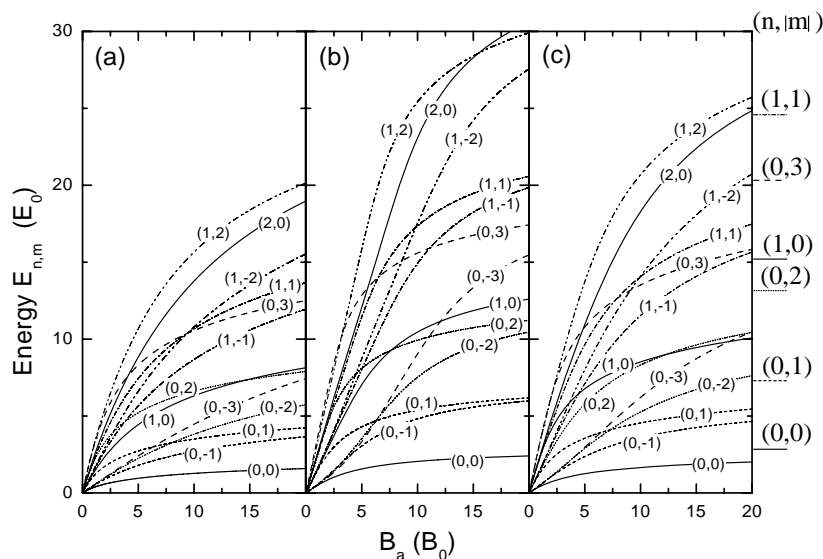


Fig. 2.2 Energy spectra as function of  $B_a$  for (a) the model without overshoot, (b) the model with overshoot, and (c) the superconducting disk case with  $z/a = 0.01$ . The  $B_a \rightarrow \infty$  limiting behavior is indicated at the right of the figure.

in Fig 2.2(c) for the real profile in case of  $z/a = 0.01$ . The different energy levels are labeled with the corresponding quantum numbers  $(n, m)$ . We found it convenient to express the energy in units of  $E_0 = \hbar^2/m_e a^2$  and the applied magnetic field  $B_a$  in units of  $B_0 = c\hbar/ea^2$ . These units are related to the problem of a particle in a box. For example for  $a = 0.01, 0.1, 1, 10\mu\text{m}$  we have respectively  $E_0 = 7.63 \times 10^{-1}, 7.63 \times 10^{-3}, 7.63 \times 10^{-5}, 7.63 \times 10^{-7}$  meV and  $B_0 = 6.6 \times 10^4, 6.6 \times 10^2, 6.6, 0.066$  Gauss, where  $m_e$  was taken the electron mass in vacuum. From Fig. 2.2 we notice that for small magnetic fields the energy is linear in  $B_a$  and in fact we recover the Landau levels  $E_{n,m} = \hbar\omega_c(n + (|m| + m)/2 + 1/2)$  for an electron in a homogeneous magnetic field. The reason is that for small magnetic field we have  $l_B/a \gg 1$ , where  $l_B = \sqrt{\hbar c/eB}$  is the magnetic length. So the electron wavefunction is spread out over a large region and most of its probability is in the  $\rho/a > 1$  region where  $B(\rho) \approx B_a$ . In the opposite case of a large external magnetic field we have  $l_B/a \ll 1$  and the electron wavefunction is localized in the dot region where there is no magnetic field present. The problem is then similar to the one of an electron in a circular dot in the absence of a magnetic field and we recover the discrete energy levels which are determined by the zeros of the Bessel function:  $J_{|m|}(k) = 0$  and are plotted on the right hand side of

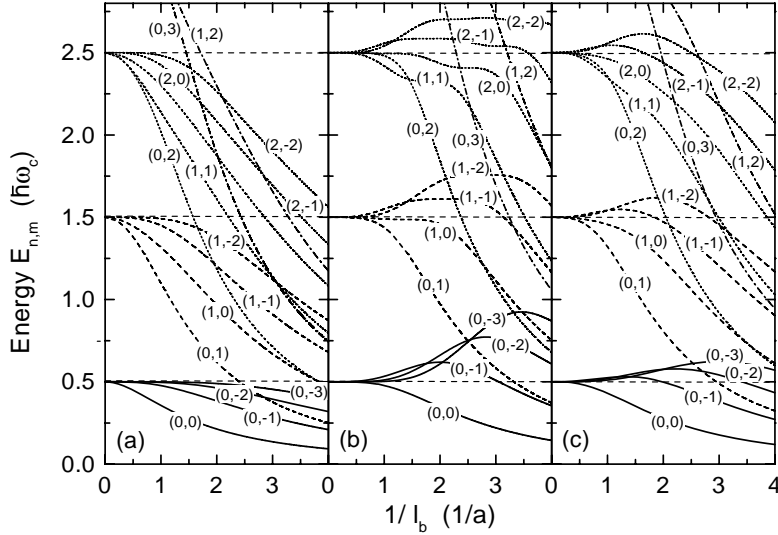


Fig. 2.3 Energy spectra (in units of  $\hbar\omega_c$ ) as function of  $l_B/a \sim \sqrt{B_a}$  for (a) the model without overshoot, (b) the model with overshoot, and (c) the superconducting disk case with  $z/a = 0.01$ .

the figure. In this case the energy scale is  $E_0 = \hbar^2/m_e a^2$  like for a particle confined in a 1D box.

Although the limiting behavior of the spectrum for  $B_a \rightarrow 0$  and  $B_a \rightarrow \infty$  is very similar in all three cases the intermediate behavior turns out to be very different. Indeed we see that the energy levels  $E_{n,m}$  of the model without overshoot increase slower than linear with increasing  $B_a$ . This is not the case when there is a magnetic field overshoot where there are a number of energy levels which for small/intermediate fields have a superlinear behavior as function of  $B_a$ . This distinct behavior is made more visible when we plot the energy in units of  $\hbar\omega_c$  as function of  $1/l_B \sim \sqrt{B_a}$  as is done in Fig. 2.3. This different behavior between the two cases can be understood by looking at Fig. 2.4, where the radial part of the electron wavefunction  $(n,m)=(0,-1)$  is plotted for various values of the magnetic field strength  $B_a$  in case of the model with magnetic overshoot. For  $m < 0$  the wavefunction exhibits a maximum at  $\rho = \rho^* > 0$ . With increasing  $1/l_B$  this maximum shifts towards the center of the dot. In case there is an overshoot in the magnetic field profile and when the maximum of the electron wavefunction is situated near  $\rho/a = 1$ , the electron energy will be increased which results in the local maximum in the energy as shown in Fig. 2.3. From this interpretation it is easy to understand that when  $m < 0$  the maximum in  $E_{n,m}/\hbar\omega_c$  shifts to larger  $1/l_B$  with increasing  $|m|$ .

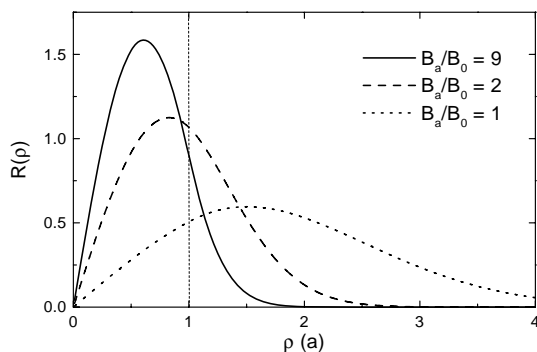


Fig. 2.4 Radial part  $R(\rho)$  of the wavefunction with quantum numbers  $(n, m) = (0, -1)$  in case of the model with overshoot as function of the radial distance to the center of the dot, for different values of  $B_a$ .

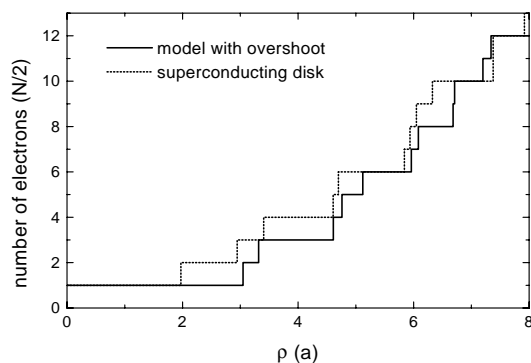


Fig. 2.5 The filling of the magnetic anti-dot with electrons as function of  $B_a$  for the model with overshoot (solid lines) and the superconducting disk model (dotted lines) with  $z/a = 0.01$ .

This behavior of the electron energy has important consequences for the filling of the dot. Outside the quantum dot the magnetic field is  $B_a$  and the electron lowest energy state is  $\hbar\omega_c/2$ . An electron will only be situated in the dot when its energy is lower than in the region outside the dot. From Fig. 2.3(a) we note that for a dot without magnetic field overshoot at its edges there are an infinite number of states, i.e. the states with  $m \leq 0$  for  $n = 0$ , which have an energy less than  $\hbar\omega_c/2$  and consequently the electrons will be attracted towards the dot. For the system with magnetic overshoot the situation is totally different. The  $|0, 0\rangle$  state has an energy below  $\hbar\omega_c/2$  and two electrons (two because of spin) will be able to occupy the dot. When

we try to add more electrons to the system we see that for small  $1/l_B$  the electrons will prefer to sit far away from the dot region where they have a lower energy, i.e.  $\hbar\omega_c/2$ . Thus in this situation the electrons are repelled by the anti-dot. Increasing the magnetic field will bring the (0,-1) level below  $\hbar\omega_c$  and then two more electrons will be attracted towards the magnetic anti-dot. This discrete filling of the dot is shown in Fig. 2.5 for the model with magnetic overshoot (solid curve) and for the superconducting disk case (dashed curve) with  $z/a = 0.01$ .

Including the real magnetic profile does not alter our conclusions qualitatively. This is shown for  $z/a = 0.01$  in Fig. 2.2(c) and Fig. 2.3(c). We obtain some kind of intermediate behavior between the two model systems. The discrete filling of the dot is still present, which can be inferred from Fig. 2.3(c). Nevertheless, the exact position at which the number of electrons jump to higher values is a function of the exact magnetic profile, and in particular depends strongly on the sharpness of the magnetic overshoot. This is why  $z/a$  has to be very small, which can always be experimentally achieved, by making the superconducting disk large enough.

## 2.4 THE PROBABILITY CURRENT DISTRIBUTION AND THE MAGNETIC MOMENT

The probability current distribution of the eigenstates is also different from the usual quantum dot case. When we rewrite the wavefunction as  $\psi(\mathbf{r}) = \alpha(\mathbf{r})e^{i\xi(\mathbf{r})}$ , the probability current is given by [13]

$$\mathbf{J}(\mathbf{r}) = (1/m_e)\alpha^2 [\hbar\nabla\xi(\mathbf{r}) + (e/c)\mathbf{A}(\mathbf{r})], \quad (2.8)$$

where the first term is the well-known circular current and the second term is due to the magnetic field. For bound states the current vector has only an angular component  $\mathbf{J}(\mathbf{r}) = J_\varphi(\mathbf{r})\mathbf{e}_\varphi$  which is independent of  $\varphi$ . The probability current distribution  $J_\varphi(\rho)$  and the corresponding radial distribution function of bounded states with  $n = 0$  and different  $m$ -values (indicated in the figure) are plotted in Fig. 2.6 for the three different cases.

For  $m = 0$  no current flows inside the dot except for the realistic magnetic field profile (Fig. 2.6), although it is very small. The  $m > 0$  states have a positive circular current which is larger with increasing overshoot of the magnetic field at the edge. For  $m < 0$  the current is circulating in the opposite direction and the magnitude increases with increasing overshoot. The maximum of the current profile moves closer to the edge with increasing  $|m|$ . Sufficiently outside the dot region the circular current is positive, irrespective of the value of  $m$ . With the delta overshoot this is also true near the outside edge of the dot where the current distribution exhibits a discontinuous behavior. In the latter case the current intensity is a uniform decreasing function of the distance  $\rho > a$ . For the case without overshoot, or when we have a continuous

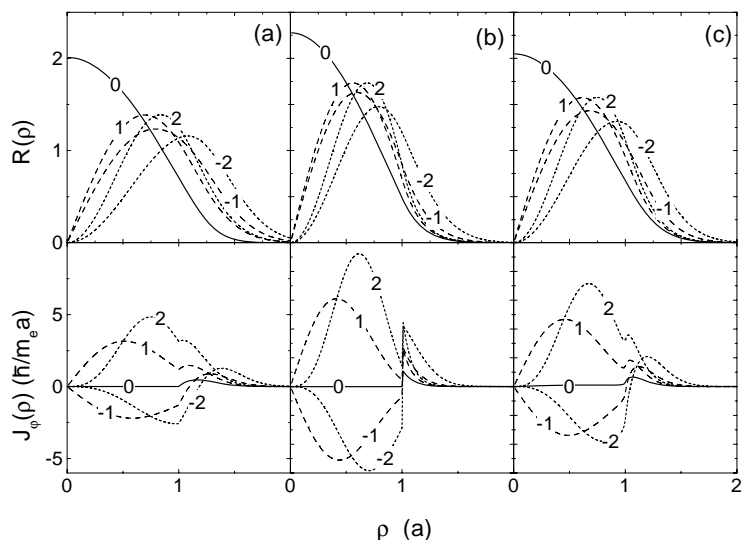


Fig. 2.6 The current density profile and the electron radial distribution when  $B_a/B_0 = 10$  are shown for various  $m$ -values (indicated on the figure) with  $n = 0$  for (a) the model without overshoot, (b) with overshoot and (c) for the superconducting disk case with  $z/a = 0.01$ .

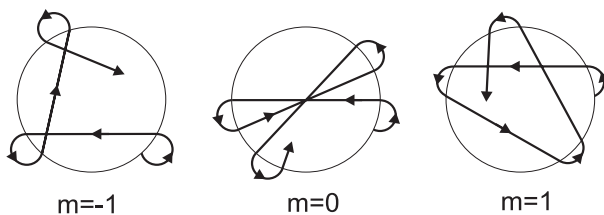


Fig. 2.7 Classical trajectories of electrons confined into a magnetic antidot without overshoot for  $m = -1$  (clockwise),  $m = 0$  and  $m = 1$  (counterclockwise).

overshoot, the current is negative near the outside edge for  $m < 0$ . These results can be understood from classical trajectories of magnetic edge states circulating clockwise ( $m < 0$ ) or counterclockwise ( $m \geq 0$ ) along the boundary region of the magnetic anti-dot without overshoot (Cfr. Ref. [84]) and which are shown in Fig. 2.7 for  $m = -1$ ,  $m = 0$  and  $m = 1$ . For completion, we also included Fig. 2.8, which is the same as Fig. 2.6, but for the states with  $m = 1$  and different  $n$ -values (indicated on the figure). Now the radial part of the wavefunction has  $n$ -nodes which results in zeros in the circular current. Note also that the current becomes much more strongly peaked near

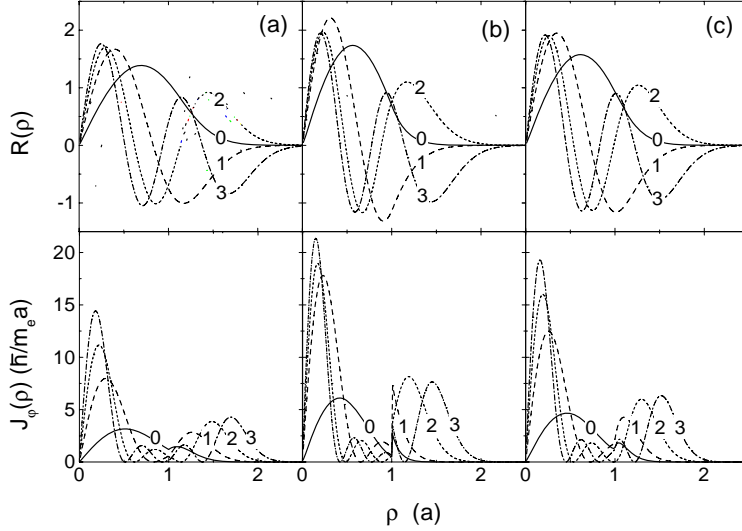


Fig. 2.8 The current density profile and the electron radial distribution when  $B_a/B_0 = 10$  are shown for various  $m$ -values (indicated on the figure) with  $n = 0$  for (a) the model without overshoot, (b) with overshoot and (c) for the superconducting disk case with  $z/a = 0.01$ .

$\rho \approx 0$ . The amount of current outside the dot also increases with increasing  $n$ . Because  $m = 1 > 0$  the current is positive irrespective of the value of  $n$ .

Also the magnetic moment is different from the quantum dot case. The magnetic moment of a particular bound state  $|n, m\rangle$  is defined as follows:  $M_{n,m} \equiv q/(2m_e)\langle n, m|\lambda_z|n, m\rangle$ , where  $\lambda_z$  is the  $z$ -component of the moment of the mechanical momentum  $\boldsymbol{\lambda} = \mathbf{r} \times [\mathbf{p} + (e/c)\mathbf{A}]$ . For convenience we write the magnetic moment  $M_{n,m}$  in units of  $M_0 = -e\hbar/(2m_e)$ , so we obtain

$$M_{n,m} = m + \frac{e}{\hbar c}\langle n, m|\rho A_\varphi(\rho)|n, m\rangle, \quad (2.9)$$

which is plotted for various one electron states in Fig. 2.9 for the three different systems. In the limit  $B_a \rightarrow 0$  we obtain the well known result  $M_{n,m} = 2n + |m| + m + 1$ : the magnetic moment is that of an electron in a homogeneous magnetic field. Notice that all states with the same  $n$  but  $m \leq 0$  have the same moment in this limit. Furthermore  $M_{n,m} > 0$  for all bound states with  $m \geq 0$ . For  $B_a \rightarrow \infty$ , the same result as for a circular dot defined by hard walls, i.e.  $M_{n,m} = m$ , is obtained for the models with (a) and without (b) overshoot. Thus the magnetic moment of the  $m < 0$  states changes sign with increasing  $B_a$ . This change in sign occurs at a larger  $B_a$ -value when  $m$  is more negative. Although the extreme limits are the same, again the intermediate behavior is

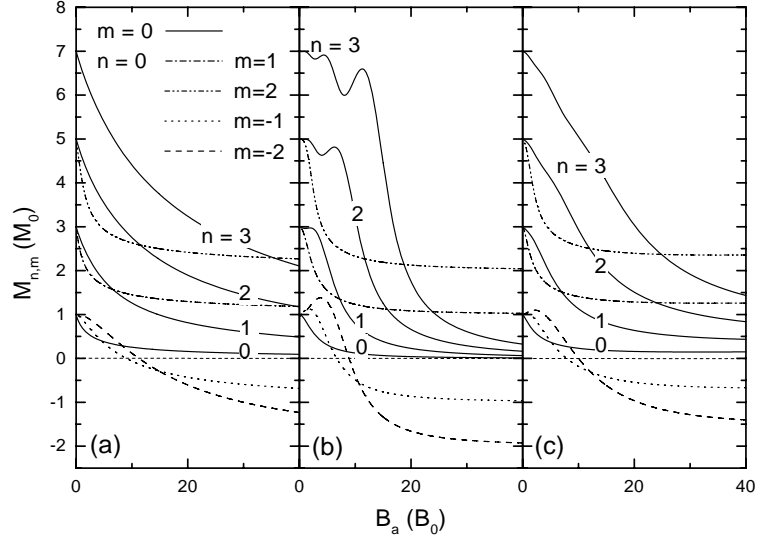


Fig. 2.9 The magnetic moment  $M_{nm}$  (in units of  $M_0 = -e\hbar/2m_e$ ) as a function of applied magnetic field strength  $B_a$  for (a) the model without overshoot, (b) with overshoot and (c) for the superconducting disk case with  $z/a = 0.01$ .

different for the three systems. As one would expect, the magnetic moment in the case of the model with overshoot reaches its  $B_a \rightarrow \infty$  limit at a smaller applied field, than in the case without overshoot. For small applied magnetic field we also observe oscillations in  $M_{n,m}$  in case of a magnetic overshoot. The oscillatory nature smoothes out and disappears as  $B_a$  is raised or when the magnetic field is smoother at the edge (see Fig. 2.9(c)). This behavior can be understood by the following picture: depending on the radial quantum number  $n$  the radial electron density has  $n + 1$  maxima. For small magnetic fields the electron wavefunction is extended outside the magnetic anti-dot. With increasing magnetic field the position of the maxima and minima in the electron density shifts, and when a maximum is at the position of the overshoot, the magnetic field has the largest influence, and consequently the magnetic moment exhibits a minimum. For a radial quantum number  $n$ , there will be  $n$  maxima in the electron density which will shift through the overshoot at  $\rho/a = 1$  with increasing magnetic field strength  $B_a$  and consequently  $M_{n,m}$  exhibits  $n$ -maxima (one is at  $B_a = 0$ ). When a minimum of the electron density is located at the overshoot, the magnetic moment has a local maximum.

In the superconducting disk case the limit  $M_{n,m}(B_a \rightarrow \infty) = m$  is never reached. In fact,  $M_{n,m}$  slightly increases for  $B_a/B_0 > 35$ , and we found  $M_{n,m} > m$  for all values of  $B_a$ . This is a consequence of the small magnetic field under the disk, which is always present as one can see in Fig. 2.1. With

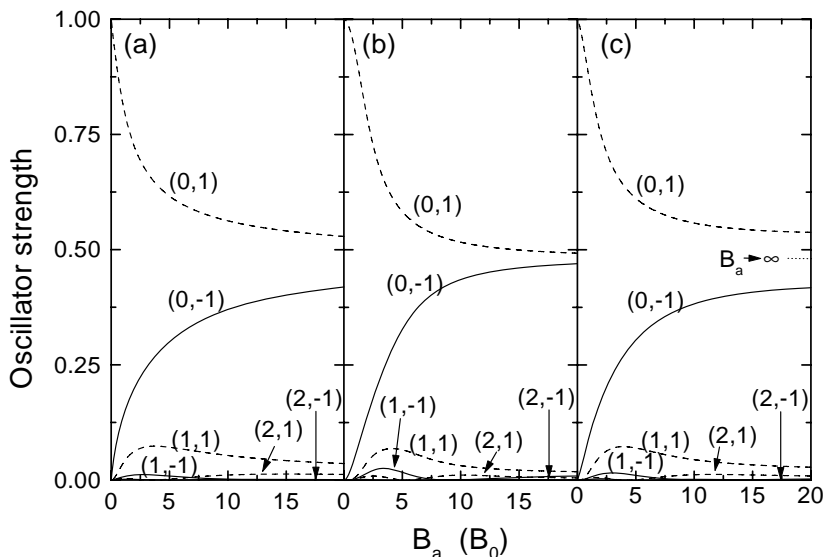


Fig. 2.10 The oscillator strength  $f_{0,0}^{n,m}$  as a function of the applied magnetic field strength  $B_a$  for (a) the model without overshoot, (b) with overshoot and (c) for the superconducting disk case with  $z/a = 0.01$ .

increasing applied magnetic field  $B_a$ , this field grows continuously, which influences the magnetic moment. The oscillatory nature of the magnetic moment of the superconducting disk case is still vaguely visible in the low magnetic field region.

## 2.5 OPTICAL PROPERTIES

For the present case of magnetically confined dots the confinement potential is not quadratic like it is often assumed for the case of electrically confined dots. This has important consequences for the optical absorption spectrum. Due to the generalized Kohn's theorem [63] the long wavelength radiation couples only with the center of mass motion of the electrons in the quadratically confined dots and the absorption spectrum exhibits only two peaks. In the present case we observe coupling between the center of mass motion and the other degrees of freedom. Transitions are only possible for  $\Delta m = \pm 1$  like in the case of quadratic confinement, but the other selection rule  $\Delta n = 0, 1$  is now broken. This is shown in Fig. 2.10 where the oscillator strength

$$f_{0,0}^{n,m} = (2m_e/\hbar^2)(E_{n,m} - E_{0,0})|\langle 0,0|\rho e^{\pm i\varphi}|n,m\rangle|^2, \quad (2.10)$$

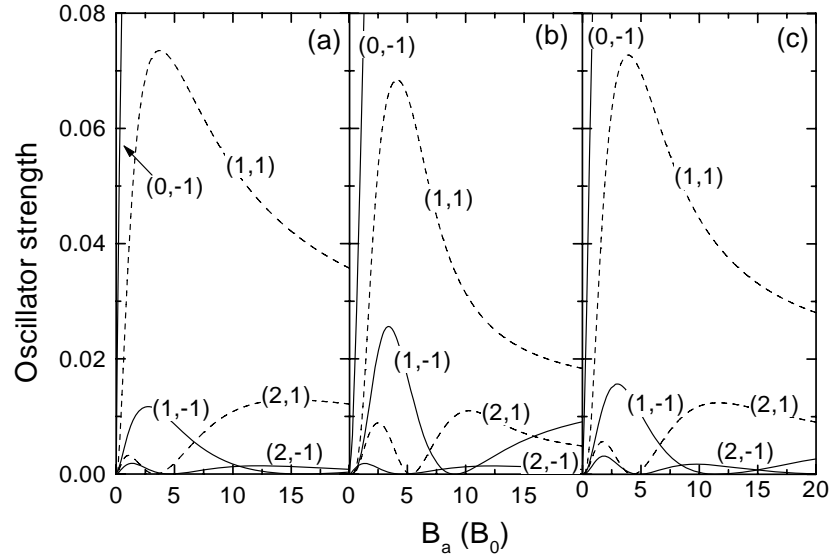


Fig. 2.11 The same as Fig. 2.10 but now the small oscillator strength region is enlarged.

for excitation from the ground state is plotted as function of  $B_a$ . This becomes more visible in Fig. 2.11 which shows an enlargement of the smaller oscillator strength region.

Consequently the absorption spectrum exhibits a larger number of peaks than in the case of a quadratic confinement potential. The transition energies as a function of the applied magnetic field  $B_a$  are plotted in Fig. 2.12. The solid curves correspond to the transitions with largest oscillator strength, the dashed and the dotted curves are respectively for transitions with one order, and two orders of magnitude smaller oscillator strength.

## 2.6 CONCLUSIONS

In conclusion we have studied the single particle properties of a magnetically confined quantum dot. When this is realized through a thin superconducting disk which is situated close to the 2DEG of a heterostructure, the magnetic field profile exhibits an overshoot at the edge of the disk which leads to a superlinear behavior of some of the energy levels as function of the strength of the external magnetic field  $B_a$ . The consequence of this behavior is a discrete filling of the dot as function of  $B_a$ . The circular current of the electron bound states has opposite sign inside and outside the dot region for the  $m < 0$  states.

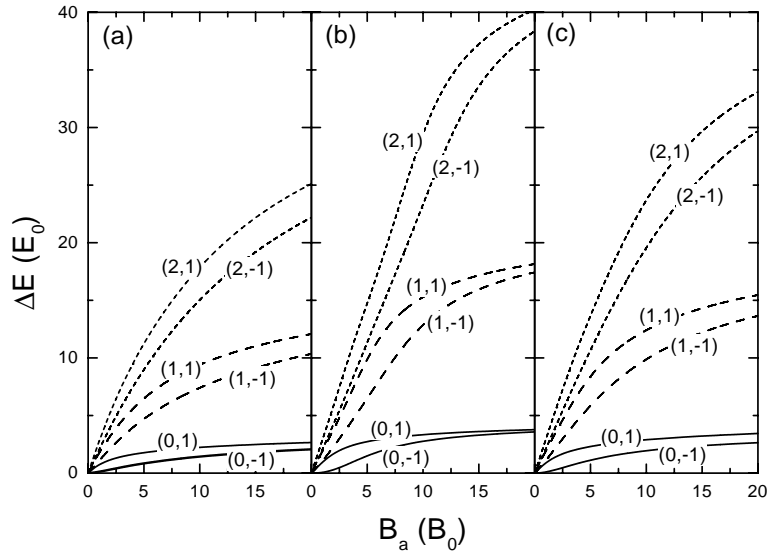


Fig. 2.12 The transition energy for excitation from the ground state  $(0, 0)$  to  $(n, m)$ . The solid curves correspond to the transitions with highest oscillator strength, the dashed and the dotted curves are respectively for transitions with amplitude one order and two orders of magnitude smaller.

These  $m < 0$  states exhibit a transition from a diamagnetic to a paramagnetic behavior with increasing  $B_a$ -field. Because of the non quadratic nature of the confinement potential we predict that the optical spectra of these new dots have aside of the two main absorption peaks a number of other peaks, with one order of magnitude smaller oscillator strength, which are a consequence of the breakdown of Kohn's theorem.

The system under study was realized in Refs. [22] and [23] where superconducting disks with  $a = 0.25 - 1.2 \mu\text{m}$  were studied in a magnetic field range  $B_a = 0 - 100$  Gauss. The superconducting disks were placed on top of a GaAs/AlGaAs heterostructure and the distance between the 2DEG and the superconducting disk was about  $z = 100$  nm. Consequently the units used in the paper take the values  $E_0 = 1.8 \times 10^{-2} - 7.9 \times 10^{-4}$  meV and  $B_0 = 105 - 4.57$  Gauss. Because the experiments were performed at temperature  $T = 0.4$  K  $\gg E_0$  the bound states studied in the present paper were not found. Furthermore, in that system the electron density was rather high  $n_e \approx 3 \times 10^{11} \text{ cm}^{-2}$  and consequently the magnetic anti-dot acts rather as a scatterer than as a potential well. One needs to increase  $E_0$ , which can be achieved by decreasing the radius of the superconducting disks, and to decrease the electron density such that the average distance between the electrons is less than the diameter of the superconducting disk. For example  $a = 0.01 \mu\text{m}$  gives  $E_0 = 11.4$  meV

and an electron density less than  $n_e = 1/\pi(2a)^2 = 7.9 \times 10^{10} \text{ cm}^{-2}$  is needed, which would be a realistic experimental situation where the predicted bound states should be observable.

# 3

---

## *Snake orbits and related magnetic edge states*

*We study the electron motion near magnetic field steps at which the strength and/or sign of the magnetic field changes. The energy spectrum for such systems is found and the electron states (bound and scattered) are compared with their corresponding classical paths. Several classical properties as the velocity parallel to the edge, the oscillation frequency perpendicular to the edge and the extent of the states are compared with their quantum mechanical counterpart. A class of magnetic edge states is found which do not have a classical counterpart.*

---

The results presented in this chapter were published as:

- F. M. Peeters, J. Reijniers, S. M. Badalian, and P. Vasilopoulos, *Microelectronic engineering* **74**, 405 (1999).
- J. Reijniers and F. M. Peeters, *J. Phys.: Condens. Matter* **12**, 9771 (2000).

### 3.1 INTRODUCTION

The transport properties of a two-dimensional electron gas (2DEG) subjected to a nonhomogeneous perpendicular magnetic field (periodically modulated or not) have been the focus of a great deal of research in recent years.[65] Current fabrication technologies permit to create nonhomogeneous magnetic fields on a nanometer scale by deliberately shaping or curving the 2DEG,[18] or by integration of superconducting [23, 86] or ferromagnetic materials [17, 47] on top of the 2DEG. This will add a new functional dimension to the present semiconductor technology and will open avenues for new physics and possible applications.[38, 54, 75]

Theoretically, the effect of nonhomogeneous magnetic fields on a 2DEG have been studied both in the ballistic and the diffusive regime. The resulting perpendicular magnetic field can act as a scattering centre,[17, 47, 74] but can also bind electrons,[42, 79, 84, 87] and so influence the transport properties of the 2DEG. In transport calculations one needs the electron states, which are obtained by solving the Schrödinger equation.

Müller [56] studied theoretically the single particle electron states of a 2DEG in a wide quantum waveguide under the application of a nonuniform magnetic field and showed that in the case of a magnetic field modulation in one direction, transport properties also become one dimensional and electron states propagate perpendicularly to the field gradient.

Making use of this decoupling, the electron states for different nonhomogeneous magnetic field profiles along one dimension were investigated, i.e. for a periodically modulated magnetic field,[33, 72, 98] for magnetic quantum steps, barriers and wells in an infinite 2DEG [12, 67] and in a narrow waveguide.[26]

In this paper we consider an infinite 2DEG subjected to a step-like magnetic field, i.e abruptly changing in magnitude or polarity at  $x = 0$ , in one dimension (taken to be the  $x$ -direction). Preliminary results were presented in Ref. [69]. First the situation for two opposite homogeneous magnetic fields with the same strength will be considered. The classical trajectories correspond to *snake orbits* and were already used in the seventies[51] to describe electron propagation parallel to the boundary between two magnetic domains. Back then, one was interested in understanding the electron transport through multi-domain ferromagnets and it turned out to be more convenient to work with the classical trajectories than with the corresponding electron states, which allows one to use a semi-classical theory which reduces the complexity of the theory considerably. We are interested in transport through a 2DEG situated in a semiconductor in which the Fermi energy is orders of magnitude smaller than in the metallic systems of Ref. [51].

We will study thoroughly the quantum mechanics of such electron states in a 2DEG subjected to this step magnetic field profile, and we will compare them with their classical counterpart. We will discuss the energy spectrum and the corresponding electron states, and derive several properties. We will show the existence of states which have a velocity in the opposite direction of

what one would expect classically. Additionally, we will show that adding a background magnetic field modifies the spectrum and the states considerably.

The paper is organized as follows. In Sec. II we present our theoretical approach. In Sec. III we calculate the energy spectrum, the wavefunctions and their corresponding group velocity, and compare this with their quantum mechanical counterpart. In Sec. IV we study the influence of a background magnetic field on the quantum mechanical and classical behaviour. In Sec. V we focus on the negative velocity state, and finally, in Sec. VI, we construct time dependent states, and interpret them classically for several magnetic field profiles.

### 3.2 THEORETICAL APPROACH

We consider a system of noninteracting electrons moving in the  $xy$ -plane in the absence of any electric potentials. The electrons are subjected to a magnetic field profile  $\vec{B} = (0, 0, B_z(x))$ . First, we will study the electronic states near the edge of two magnetic fields with the same strength but opposite sign

$$B_z(x) = B_0 [2\theta(x) - 1], \quad (3.1)$$

which is independent of the  $y$ -coordinate. Next, we will consider the influence of a background magnetic field  $B$  on these states, which results in the magnetic field profile

$$B_z(x) = B_0 [2\theta(x) - 1] + B. \quad (3.2)$$

In the following we will use  $B^l = B_z(x < 0)$  and  $B^r = B_z(x > 0)$  to denote respectively the magnetic field on the left and the right hand side of the magnetic edge.

The one-particle states in such a 2DEG are described by the Hamiltonian

$$H = \frac{1}{2m_e} p_x^2 + \frac{1}{2m_e} \left[ p_y - \frac{e}{c} A(x) \right]^2. \quad (3.3)$$

Taking the vector potential in the Landau gauge,

$$\vec{A} = (0, xB_z(x), 0), \quad (3.4)$$

we arrive at the following 2D Schrödinger equation

$$\left\{ \frac{\partial^2}{\partial x^2} + \left[ \frac{\partial}{\partial y} + ixB_z(x) \right]^2 + 2E \right\} \psi(x, y) = 0,$$

where the magnetic field is expressed in  $B_0$ , all lengths are measured in the magnetic length  $l_B = \sqrt{\hbar c / eB_0}$ , energy is measured in units of  $\hbar\omega_c$ , with  $\omega_c = eB_0 / m_e c$  the cyclotron frequency and the velocity is expressed in units

of  $l_B\omega_c$ .  $H$  and  $p_y$  commute due to the special form of the gauge, and consequently we can write the wavefunction as follows

$$\psi(x, y) = \frac{1}{\sqrt{2\pi}} e^{-iky} \phi_{n,k}(x), \quad (3.5)$$

which reduces the problem to the solution of the 1D Schrödinger equation

$$\left[ -\frac{1}{2} \frac{d^2}{dx^2} + V_k(x) \right] \phi_{n,k}(x) = E_{n,k} \phi_{n,k}(x), \quad (3.6)$$

where it is the  $k$ -dependent effective potential

$$V_k(x) = \frac{1}{2} [xB_z(x) - k]^2, \quad (3.7)$$

which contains the two dimensionality of the problem. We will solve Eq. (3.6) numerically by use of a discretization procedure. In some limiting cases analytical results can be obtained.

### 3.3 IN THE ABSENCE OF A BACKGROUND MAGNETIC FIELD

Let us first consider the case when no background magnetic field is present. The situation is then symmetric, and easier to solve. The effective potential for this case is shown in Fig. 3.1(a) for  $k = -2$  (dotted curve) and  $k = 2$  (solid curve). We notice from Eq. (3.7) that this potential is built from two parabolas, with minima situated at  $x^l = -k$ , and  $x^r = k$ , thus respectively on the left and right hand side of the magnetic edge. The total potential has for  $k > 0$  two local minima respectively at  $x = -k$  and  $x = +k$ , while for  $k < 0$  it has only one minimum at  $x = 0$ . Before we describe the energy spectrum of the snake orbits and their corresponding properties, we first discuss the limiting behaviour.

#### 3.3.1 Limiting behaviour for $k \rightarrow \pm\infty$

For  $k \rightarrow \infty$ , the minima of the parabolas are situated far from each other. The electrons are in the Landau states of two opposite magnetic fields, one on the left, the other on the right, and they are not interacting with each other. The electron wavefunctions are given by  $\langle L|x \rangle = C_m H_m(x+k) e^{-(x+k)^2/2}$ , and  $\langle R|x \rangle = C_m H_m(x-k) e^{-(x-k)^2/2}$ , respectively, where  $H_m(x)$  is the Hermite polynomial. For decreasing  $k$  the parabolas shift towards each other, and the electrons will start to “feel” each other. In terms of wavefunctions, this results in a parabolic cylinder function  $\phi(x) = D_{E-\frac{1}{2}}[\sqrt{2}(x-k)]$  matched at  $x = 0$ , with the condition that  $\frac{d}{d\alpha} D_{E-\frac{1}{2}}(\alpha)|_{\alpha=-\sqrt{2}k} = 0$  or  $D_{E-\frac{1}{2}}(-\sqrt{2}k) = 0$ , for the symmetric and the antisymmetric wavefunction, respectively. This leads

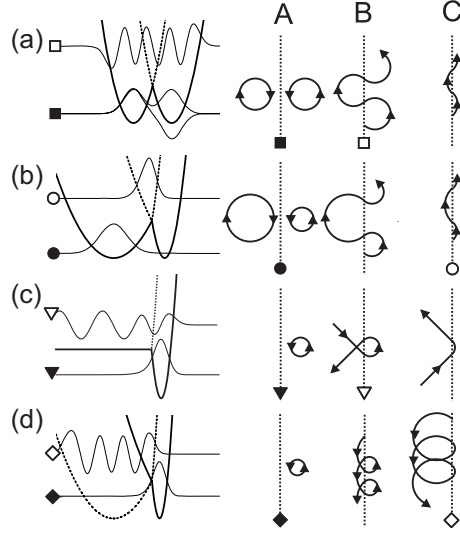


Fig. 3.1 The effective potential (left part of the figure) for  $k = -2$  (dotted curve) and  $k = 2$  (solid curve) for the different magnetic field profiles  $(B^l, B^r)$ : (a)  $(-1, 1)$ , (b)  $(-0.5, 1.5)$ , (c)  $(0, 2)$ , (d)  $(0.5, 2.5)$ , indicated at the top of Fig. 3.2. The wavefunctions corresponding to the states in Fig. 3.2, as indicated by the corresponding symbols, are also shown. Schematic representation of the classical electron trajectories (right part of the figure) corresponding to the different regions indicated in Fig. 3.2.

to a change in energy of the electron states, which can be understood as a lifting of the degeneracy of the two original electron wavefunctions. The energy can then be written as  $E_{\pm}(k) = \langle L|H|L\rangle(k) \pm \langle L|H|R\rangle(k) = E(k) \pm \Delta E(k)$  with the corresponding wavefunctions  $|\phi\rangle = |R\rangle \mp |L\rangle$ . One can see that for an electron confined in one parabola, the presence of the other parabola results in two effects: (1) a decrease of  $E(k)$  due to the finite presence of the wave function in the other parabola, and (2) a splitting of the energy level due to the overlap, i.e. one level ( $E_+$ ) shifts upwards, while the other ( $E_-$ ) shifts down. For  $k \rightarrow \infty$ , this results in the following first-order approximation to  $E$  and  $\Delta E$ :

$$E_m(k) = \frac{1}{2} + m - \frac{2^{m-1}}{m! \sqrt{\pi}} k^{2m-1} e^{-k^2}, \quad (3.8)$$

$$\Delta E_m(k) = \frac{2^m}{m! \sqrt{\pi}} e^{-k^2} k^{2m+1}. \quad (3.9)$$

In the other limit  $k \rightarrow -\infty$ , the effective potential can be approximated by a triangular well  $V(x) = k^2/2 - kB_0x$ . Solutions for this potential consist of Airy functions, again matched at  $x = 0$  with the condition that  $\phi'(0) = 0$  or  $\phi(0) = 0$  which results respectively in the anti-symmetric wavefunction

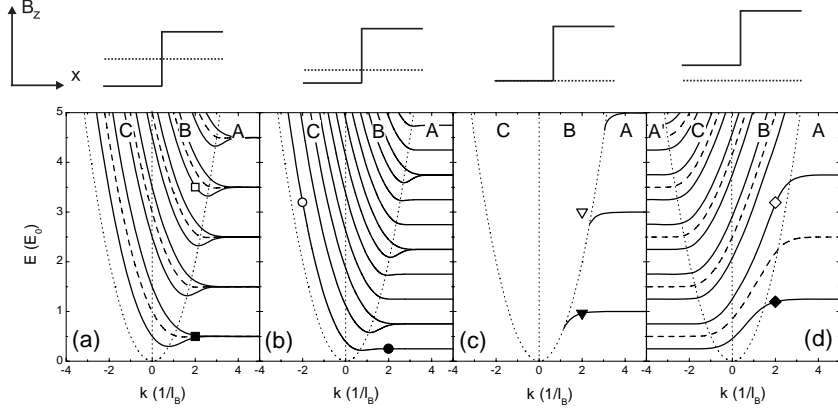


Fig. 3.2 The energy spectra for different magnetic field profiles ( $B^l, B^r$ ) shown on top of the figure: (a)  $(-1, 1)$ , (b)  $(-0.5, 1.5)$ , (c)  $(0, 2)$ , (d)  $(0.5, 2.5)$ . The dotted curves mark the different classical regions. The dashed curves in (a) and (b) are the average energy of two adjacent levels. The symbols correspond to the electron wavefunctions plotted in Fig. 3.1.

$\phi_{2m}(x) = C_{2m}(k) (|x|/x) Ai \left[ z_{Ai', m+1} + (2k)^{1/3} |x| \right]$  and a symmetric one  $\phi_{2m+1}(x) = C_{2m+1}(k) Ai \left[ z_{Ai, m+1} + (2k)^{1/3} |x| \right]$ , respectively with energy

$$E_{2m}(k \rightarrow -\infty) = \frac{1}{2} \left[ k^2 - z_{Ai', m+1} (2|k|)^{2/3} \right], \quad (3.10)$$

$$E_{2m+1}(k \rightarrow -\infty) = \frac{1}{2} \left[ k^2 - z_{Ai, m+1} (2|k|)^{2/3} \right], \quad (3.11)$$

where  $z_{Ai, n} (= -2.338, -4.088, -5.521, \dots, -[3\pi(4n-1)/8]^{2/3})$  and  $z_{Ai', n} (= -1.019, -3.248, -4.820, \dots, -[3\pi(4n-3)/8]^{2/3})$ , denote respectively the  $n^{\text{th}}$  ( $n = 1, 2, 3, \dots, \infty$ ) zero of the Airy function and of its derivative. One can see that for increasing negative  $k$ , the difference between the two energy branches increases, which is to first order linear in  $|k|$ . Namely, the more negative  $k$ , the narrower the well, thus the more the energy levels are shifted from each other.

### 3.3.2 Spectrum and velocity

Solving Eq. (3.6) numerically gives rise to the energy spectrum shown (solid curves) in Fig. 3.2(a). For  $k = \infty$ , we obtain the earlier mentioned Landau levels, which are labeled with the quantum number  $m$ . Each level is twofold degenerate. For decreasing  $k$ , the degeneracy is lifted and they separate into

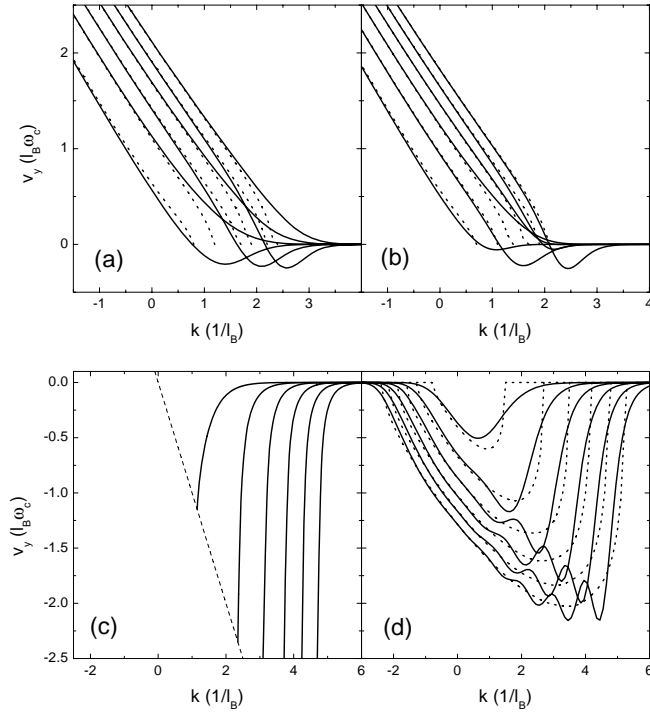


Fig. 3.3 The group velocity in the  $y$ -direction (parallel to the edge) of the 6 lowest branches of Fig. 3.2 for the different magnetic field profiles (a,b,c,d). The dotted curves correspond to the velocity calculated for the classical snake orbits.

two different branches with eigenstates  $|2m\rangle$  and  $|2m+1\rangle$  and eigenvalues  $E_{2m}$  and  $E_{2m+1}$ , and corresponding quantum numbers  $n = 2m$  and  $n = 2m+1$ . This quantum number  $n$  does not only result from arranging the levels according to their lowest energy, starting with  $n = 0$ , but it also reflects the number of nodes of the corresponding wavefunction. Notice that the levels have now a non-zero derivative, i.e. electrons propagate in the  $y$ -direction, and their group velocity is given by  $v(k) = -\partial E(k)/\partial k$ . (The minus sign appears here because in Eq. (3.5) we took  $k_y = -k$ ). This group velocity is plotted (solid curves) in Fig. 3.3(a) for the 6 lowest levels. For  $k = \infty$  electrons are in a Landau level, and consequently there is no net current in the  $y$ -direction. Decreasing  $k$ , results in a net current in the  $y$ -direction, which is positive for the upper branches ( $2m+1$ ), but is initially negative for the branches ( $2m$ ). For more negative values of  $k$  it increases almost linearly with increasing  $|k|$ , which becomes the first order analytical result  $v_m(k \rightarrow \infty) = -k$ , obtained by differentiating (3.10) and (3.11).

### 3.3.3 Classical picture

The center of the classical orbit corresponds to a zero in the effective potential. The energy spectrum can be divided up into three regions which can be classically understood by the electron orbits drawn in Fig. 3.1(a). In region (A) the electrons move in closed orbits either in the magnetic field on the left or on the right hand side. Since its cyclotron radius is smaller than the distance to the magnetic field discontinuity, they feel a homogeneous magnetic field. As a result of the opposite magnetic field, one electron rotates clockwise, while the other moves counterclockwise. There is no net velocity. In region (B) the cyclotron radius intersects the magnetic field discontinuity slightly, i.e. in such a way that the moving electron and the center of its orbit are on the same side. The electron is able to penetrate into the opposite magnetic field region, which results in a (rather small) propagation in the  $y$  direction  $v_y > 0$ . For  $k = 0$  the center of the orbit is exactly on the edge between the two opposite magnetic fields. In region (C) the center of the cyclotron orbit is located in the opposite magnetic field region of which the electron is moving in, resulting in a faster propagation of the electron in the  $y$ -direction. These different regions are also indicated in Fig. 3.2(a).

We can also make a quantitative classical study of the velocity, starting from the quantum mechanical energy spectrum. Since in classical mechanics there is no quantization, we make use of the obtained quantum energy spectrum in order to find the classical energy and thus the radius of the cyclotron orbit. Classically, the energy is contained in the circular velocity  $v_\varphi$  through  $E(k) = v_\varphi^2(k)/2$ . For any given quantum mechanical  $E(k)$ -value we obtain classically the circular velocity  $v_\varphi(k) = \sqrt{2E(k)}$ . Now if we consider  $x_0 = \pm k$  to be the center of the electron orbit, we can calculate for every  $k$ -value the classical velocity  $v_y(k)$ , since we also know  $v_\varphi(k)$  and the cyclotron radius  $R(k) = v_\varphi(k)$ . Using geometrical considerations, we obtain the following relation

$$v_y(k) = v_\varphi(k) \sqrt{1 - [k/v_\varphi(k)]^2 / \arccos[k/v_\varphi(k)]}, \quad (3.12)$$

which is shown in Fig. 3.3(a) by the dotted curves. Comparing this with its quantum mechanical counterpart, we notice that for  $k < 0$  good agreement is found, but for  $k > 0$  there is a large discrepancy. Moreover, one can see that negative velocities cannot exist classically.

The critical  $k$ -value,  $k^*$ , defines the region for which no classical propagating state can exist, i.e. when the electron describes just a circular orbit in a homogeneous magnetic field and does not intersect the magnetic field discontinuity. Hence, this critical value has to be equal to the cyclotron radius  $k^* = R(k^*) = v_\varphi(k^*) = \pm \sqrt{2E(k^*)}$ , which leads to the boundary drawn in Fig. 3.2(a) (dotted parabola).

### 3.4 WITH A BACKGROUND MAGNETIC FIELD

With a background magnetic field three different configurations: a)  $0 < B < B_0$ , b)  $B = B_0$ , and c)  $B_0 < B$  have to be considered. In the following we will study the snake orbits in these configurations.

#### 3.4.1 $0 < B < B_0$

Applying a background magnetic field  $0 < B < B_0$ , results in a situation which is very similar to the previous one. Again the two magnetic fields have opposite sign, but in this case they also have a different strength, i.e.  $B^l = -B^r/p$ . Again we can calculate analytically the correction to the energy in the limit  $k \rightarrow \infty$ . For an electron on the right hand side in the  $m^{\text{th}}$  Landau state of a magnetic field with strength  $B^r = B_0$ , the deviation from the Landau energy due to the presence of the other parabola in the effective potential is given by the following matrix element, which to second-order reads

$$\begin{aligned} E_m(k \rightarrow \infty) &= |\langle R | H | R \rangle (k)| \\ &= \left[ m + \frac{1}{2} \right] - \frac{2^{m-2}}{m! \sqrt{\pi}} \left( 1 + \frac{1}{p} \right) k^{2m-1} e^{-k^2}. \end{aligned} \quad (3.13)$$

For an electron on the left hand side, i.e. in the smaller magnetic field  $B^l = -B_0/p$  region, in the  $m^{\text{th}}$  Landau level, this results in

$$\begin{aligned} E_m(k \rightarrow \infty) &= |\langle L | H | L \rangle (k)| \\ &= \frac{1}{p} \left[ m + \frac{1}{2} \right] - \frac{2^{m-2}}{m! \sqrt{\pi}} \left( 1 + \frac{1}{p} \right) k^{2m-1} e^{-k^2}. \end{aligned} \quad (3.14)$$

Also in this case the energy is smaller than the corresponding Landau energy. The downward energy shift decreases for increasing  $p$ .

If  $p$  is an integer, Landau states on the left and right hand side, respectively with quantum number  $p \cdot m$  and  $m$ , coincide for  $k \rightarrow \infty$ . As a consequence these states have an overlap, which reads to first order

$$\begin{aligned} \langle L | H | R \rangle &= (-1)^{m+1} 2^{m(p+1)/2} \left( \frac{1}{(pm)! m! \pi} \right)^{1/2} \\ &\quad \times p^{pm/2} e^{-k^2(1+p)/2} k^{m(p+1)+1}. \end{aligned} \quad (3.15)$$

One can see that for decreasing magnetic field, i.e. increasing  $p$ , this function decreases because of the exponential factor. The electron wavefunction in the lower magnetic field region is extended over a larger region, and further away from the other (center at  $kp$ ). The overlap therefore decreases with increasing  $p$ . As a result of this, the energy for  $k \rightarrow \infty$  and  $p > 1$  is given by  $\langle R | H | R \rangle$  and  $\langle L | H | L \rangle$ .

For  $p = 1$ , we obtain the previous result, but for increasing  $p$ , the second order term in Eqs. (3.13) and (3.14) becomes more important than Eq. (3.15),

because of the exponential factor. The splitting is lifted, and the main contribution to the negative velocity for  $k \rightarrow \infty$  arises from Eq. (3.15) due to the finite extent of the wavefunction in the other parabola.

As an example we studied numerically the case when a background magnetic field  $B = B_0/2$  is applied, i.e.  $B^l = -B_0/2$  and  $B^r = 3B_0/2$ . As one can see in Fig. 3.1(b), this results in two parabolas with different minima and confinement strength. The resulting spectrum (see Fig. 3.2(b)) is very similar to the one of the previous case, but unlike the previous symmetrical case, not all states are twofold degenerate for  $k \rightarrow \infty$ . We now obtain two different sets of Landau states, corresponding to electrons moving in different magnetic field regions with different strength. In this case the second Landau level on the left coincides with the first on the right. The classical picture for the three different regions corresponds to the one drawn in Fig. 3.1(b), and is also similar to the previous case, except for the different cyclotron radii. With this picture in mind, one can again calculate the classical velocity, which turns out to be identical to Eq. (3.12). From Fig. 3.3(b) we notice that again we obtain good agreement for  $k > 0$ , but for  $k < 0$ , there is a large discrepancy. The negative velocity can also in this case not be explained classically.

The critical  $k$ -value  $k^* = \sqrt{2E(k^*)}$  for which snake orbits are classically possible are indicated by the parabola in Fig. 3.2(b).

### 3.4.2 $B = B_0$

When a background magnetic field  $B = B_0$  is applied, we obtain the magnetic barrier studied in Ref.[67], where the magnetic field is different from zero only in the region  $x > 0$ , i.e.  $B^l = 0$  and  $B^r = 2B_0$ . From Fig. 3.1(c) one can see that in this case the potential is made up of only one parabola on the right hand side, on the left side it is constant  $k^2/2$ . The energy spectrum and corresponding velocities for this particular case are shown in Fig. 3.2(c) and 3.3(c), respectively. We notice that for  $k \rightarrow \infty$  we again obtain Landau states, which correspond to bound states on the right hand side of the magnetic edge. Consistent, as being a limiting case of the former magnetic field states, i.e.  $p = \infty$ , the energy decreases with decreasing  $k$  and there is no splitting of the energy levels. Thus now we only have states which propagate with negative velocity to which we cannot assign a classical interpretation.

Also in this case we can subdivide the spectrum into three regions: (A) the electrons move in closed orbits in the magnetic field region on the right hand side, (B) electrons are free, propagate forward and are reflected on the barrier and (C) electrons are free, propagate backward and are reflected on the magnetic edge. Notice that for a free electron, the energy is larger than  $k^2/2$ , since now the electron also propagates in the  $x$ -direction and consequently has an additional kinetic energy  $k_x^2/2$ .

Classically, propagating states in the magnetic field region do not exist, only Landau states. The boundary where these classical trajectories are possible is again given by  $k^* = \sqrt{2E(k^*)}$ .

### 3.4.3 $B_0 > B$

By applying a background magnetic field with strength larger than  $B > B_0$ , we arrive at the situation where  $0 < B^l < B^r$ . The magnetic fields on the left and the right hand side have the same sign, but a different strength, i.e.  $B^l = B^r/p$ .

To obtain the energy in the limits  $k \rightarrow \pm\infty$ , we again can approximate the wavefunction as being in a Landau state in the corresponding magnetic field. We found

$$\begin{aligned} E(k \rightarrow \infty) &= \langle R | H | R \rangle (k) \\ &= \left[ m + \frac{1}{2} \right] - \frac{2^{m-2}}{m! \sqrt{\pi}} \left( 1 + \frac{1}{p} \right) k^{2m-1} e^{-k^2}, \end{aligned} \quad (3.16)$$

for an electron on the right hand side in the  $m^{\text{th}}$  Landau state of a magnetic field with strength  $B^r = B_0$ . For an electron on the left hand side, in the smaller magnetic field  $B^l = B_0/p$  in the  $m^{\text{th}}$  Landau level, we have

$$\begin{aligned} E(k \rightarrow -\infty) &= \langle L | H | L \rangle (k) \\ &= \frac{1}{p} \left[ m + \frac{1}{2} \right] + \frac{2^{m-2}}{m! \sqrt{\pi}} \left( 1 + \frac{1}{p} \right) k^{2m-1} e^{-k^2}, \end{aligned} \quad (3.17)$$

which results in a negative velocity.

The energy spectrum and the velocity of these eigenstates for the case when  $B = 3B_0/2$ , i.e.  $B^l = B_0/2$ ,  $B^r = 5B_0/2$ , are plotted respectively in Fig. 3.2(d) and 3.3(d). The center of the orbit is situated on the right side for  $k > 0$ , for  $k < 0$  it is on the left side. For  $k \rightarrow \pm\infty$ , the electrons move in a homogeneous magnetic field (on the left ( $k \rightarrow -\infty$ ) or right ( $k \rightarrow +\infty$ ) hand side of  $x = 0$ ), and thus  $v_y = 0$ .

From Fig. 3.1(d) one notices that there is only one minimum in the effective potential. This is due to the fact that the two different parabolas (corresponding to the different magnetic fields) which constitute the effective potential, have their minima on the same side, i.e. on the left ( $k < 0$ ) or on the right hand side ( $k > 0$ ). The trajectories corresponding with regions (A), (B), and (C) are depicted in Fig. 3.1(d). The trajectories in region (A') are similar to those in (A) but now for a magnetic field on the left hand side, i.e. with smaller strength.

Geometrical considerations yield the following classical velocity

$$\begin{aligned} v_y(k) &= 2v_\varphi(k) \sqrt{1 - [k/v_\varphi(k)]^2} \\ &\times \{ B^l \arccos[-k/v_\varphi(k)] + B^r \arccos[k/v_\varphi(k)] \}^{-1}, \end{aligned} \quad (3.18)$$

which is plotted in Fig. 3.3(d) as dotted curves together with the quantum mechanical group velocity. One can see that, in contrast to the previous cases, the negative velocity can be understood as classical snake orbits, but these

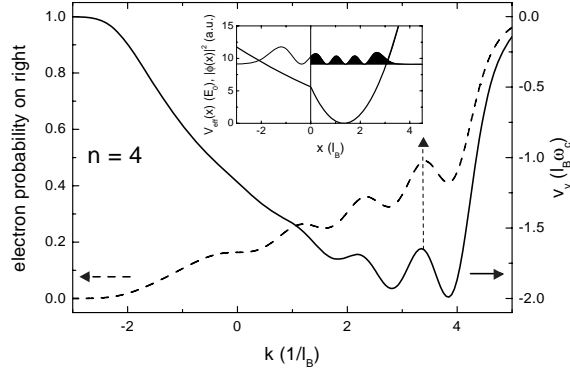


Fig. 3.4 The velocity for the  $n = 4$  state of Fig. 3.3(d), and the electron probability for the electron to be in the right part of the parabola as function of  $k$ . The inset shows the effective potential and the electron probability at the local maximum  $kl_B = 3.4$ .

snake orbits all run in the same  $y$ -direction and now there are no states with  $v_y > 0$ .

Notice that the quantum mechanical velocity exhibits a small oscillatory behaviour on top of a uniform profile. These wiggles can be understood from the electron distribution over the two parabolas (see Fig. 3.4). With increasing  $k$ , the electron distribution is shifted from the left parabola to the right one. Due to the wavelike character of this distribution, the probability for an electron to be in the right parabola (integrated solid region in the inset of Fig. 3.4) exhibits wiggles as function of  $k$ , with  $n$  maxima as shown in Fig. 3.4. Energetically it is favorable for an electron state to have as much as possible electron probability in the lower potential region. Consequently, when the electron probability in the lower potential region attains a maximum, a maximum downward energy shift will be introduced on top of the overall energy change, and this will result in a maximum in the group velocity.

### 3.5 NEGATIVE VELOCITY STATE

Formally, the existence of the quantum mechanical negative velocity state can be attributed to the fact that shifting two

one dimensional potential wells towards each other results in a significant rearrangement of the energy levels in the composite potential well. Because the composed well is broader, some states, e.g. the ground state, have an energy which is lower than in each of the individual narrower wells. In this particular case, the wave vector  $k$  measures the distance of the two wells to each other, and consequently this energy decrease results in a negative group

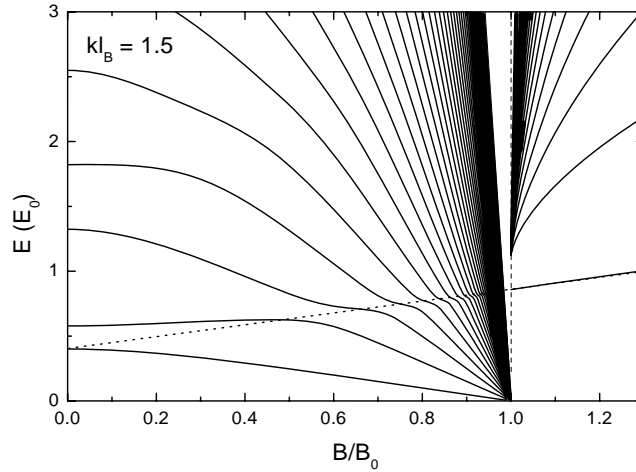


Fig. 3.5 The energy spectrum at  $kl_B = 1.5$  for the 40 lowest states as function of the applied background field  $B/B_0$ .

velocity  $-\partial E/\partial k$ . In this section we focus on these negative group velocity states.

Since the negative velocity states are present for any background magnetic field  $B$ , but can only be understood classically in the situation  $B > B_0$ , we will investigate the group velocity for a fixed  $k$ -value with varying background magnetic field. In Fig. 3.5 the spectrum is plotted as function of the applied background field  $B$ . We have chosen  $k = 1.5$  because in this case a large negative velocity is obtained for the lowest level when  $B = 0$ . Notice that for  $B < B_0$ : (1) almost all levels decrease in energy with increasing background field; (2) there is an anti-crossing for  $E/E_0 = 0.4 + 0.458B/B_0$  (dotted line). This anti-crossing occurs when  $B/B_0 = n/(n+1)$ , with  $n$  the Landau level index. For this condition some of the Landau levels are degenerate in the limit  $k \rightarrow \infty$  (see Fig. 3.2(b) for the case  $n = 0$ ); and (3) for  $B \rightarrow B_0$  the separation between the levels decreases to zero and a continuous spectrum is obtained with a separate discrete level at the anti-crossing line. The continuous spectrum for  $B = B_0$  results from the scattered states in the potential of Fig. 3.2(c), while the discrete state is the bound state in this potential. For the considered  $k$ -value, i.e.  $k = 1.5$ , only one bound state is found for  $B = B_0$ .

The corresponding group velocity  $v_y = -\partial E/\partial k$  is shown in Fig. 3.6. Notice that the maximum negative velocity is obtained near the anti-crossings in the energy spectrum (Fig. 3.5). Near  $B/B_0 = n/(n+1)$  the splitting in the energy spectrum (see Fig. 3.2) is largest and as a consequence one of the levels is pushed strongly down in energy and consequently  $v_y$  becomes strongly

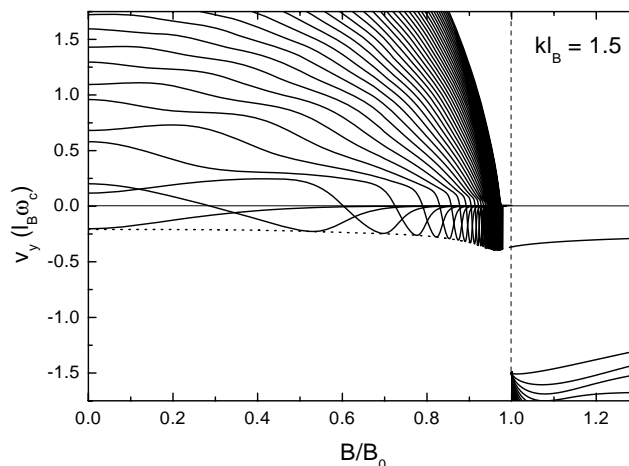


Fig. 3.6 The group velocity  $v_y$  as function of  $B/B_0$ , corresponding to the electron states of Fig. 3.5.

negative. Notice that: (1) every level has some  $B/B_0$  region at which  $v_y < 0$ , and (2) for  $B/B_0 \rightarrow 1$  the velocity  $v_y \rightarrow 0$ , while (3) the envelope of  $(v_y)_{\min}$  in Fig. 3.6 reaches for  $B/B_0$  the  $v_y < 0$  value of the  $B = B_0$  state. For  $B > B_0$  we have  $v_y < 0$  for all states.

Using expressions (3.12) and (3.18), we can also calculate the classical velocity corresponding to the energy spectrum in Fig. 3.5. This is shown in Fig. 3.7. We notice that for  $B/B_0 < 1$ , the classical velocity has a similar behaviour as the quantum mechanical one, except for the anti-crossings and the lack of negative velocities, which do not have a classical counterpart. These negative velocities appear suddenly for  $B/B_0 > 1$  and exhibit more or less the same behaviour.

As was already apparent from the above study a necessary condition for the existence of the non-classical edge states is the presence of two local minima in the effective potential. In the limiting case  $B = B_0$  the second minima is the limiting case of a flat region in  $V_k(x)$  for  $x < 0$ . But not all these states have a negative velocity. How can we classify them?

From Fig. 3.2(a,b) one notices that initially (for rather small  $B$  values) the parabola  $E = k^2/2$  separates the region where only states with positive group velocity exist from the region where also negative velocity states are present. This is due to the fact that the value of this parabola equals the barrier height between the two parabolic wells for the corresponding  $k$ -value. When the energy exceeds this barrier, the shape of the wavefunction is not determined anymore by the separate parabolas, but by the overall composite well width. For decreasing  $k$  the well is squeezed, and thus all the energy

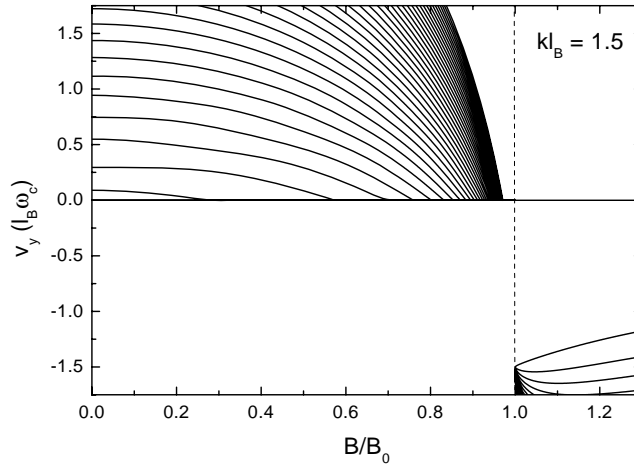


Fig. 3.7 The classical velocity in the  $y$ -direction as function of  $B/B_0$ , corresponding to the electron states of Fig. 3.5.

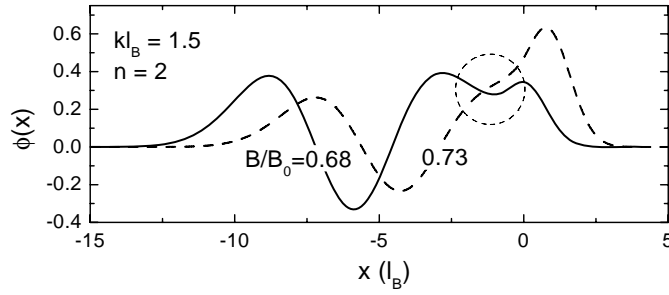


Fig. 3.8 The wavefunctions for  $kl_B = 1.5$ ,  $n = 2$  for two negative velocity states (see Fig. 3.6) with background magnetic field  $B/B_0 = 0.68; 0.73$ .

levels are pushed upwards, resulting in a positive group velocity. Although this is not an exact rule which cannot be extended rigorously throughout the  $B < B_0$  regime, it nevertheless provides insight into the  $k$ -values (or  $B$  values) for which these negative velocities states arise.

Inspection of the wavefunctions shows that there is a feature which marks the negative velocity states, and which relates indirectly to the presence of the different potential wells. It turns out that if the wavefunction or its first derivative exhibits a dip at some  $x$  which satisfies  $\phi(x)\phi''(x) > 0$  and  $\phi'(x) = 0$ , or  $\phi'(x)\phi'''(x) > 0$  and  $\phi''(x) = 0$  and the condition that  $\phi(x) \neq 0$ ,

then the state has a non-classical negative velocity. This is true for every  $k$  value, as long as  $B < B_0$ . This is illustrated in Fig. 3.8 where we plot the wavefunction for  $k = 1.5$ ,  $n = 2$ , with background magnetic field  $B/B_0 = 0.68$  and  $0.73$ . The above dip in the wavefunction or its derivative (indicated by the dashed circle in Fig. 3.8) is a result of the different potential wells, which have their separate influence on the shape of the wavefunction, and therefore hamper the matching. The difference in  $\phi(x)$  being zero (or not), can be interpreted as a generalization of matching the individual states in an asymmetric (symmetric way) when the Landau states are degenerate at  $k \rightarrow \infty$ .

### 3.6 TIME DEPENDENT CLASSICAL INTERPRETATION

One can make different attempts to link a classical picture to quantum mechanics. Often the comparison starts with a schematic classical picture which is then supported by comparing the quantum mechanical probability density with the classical one, obtained through calculation of the classical electron trajectory solving Newton's equation. For a 1D problem one can also verify the classical motion by inspection of the velocity parallel to the edge.[26, 56, 65, 98] For a cylindrical symmetric problem, the classical electron motion can be inferred from the magnetic moment or the circular current distribution of the electron state.[42, 79, 84, 87] In this paper, a quantitative comparison was made by use of a quantum mechanical velocity parallel to the 1D magnetic field discontinuity. In the following, we will try a different approach where we will construct time dependent states, and in doing so we will introduce another feature, i.e. the oscillation frequency perpendicular to the magnetic edge.

#### 3.6.1 $B = 0$

We already mentioned before that the solutions for this kind of problem are the parabolic cylinder functions  $\phi(x) = D_{E-\frac{1}{2}}[\sqrt{2}(x-k)]$ , matched in such a way that we have symmetric and anti-symmetric wavefunctions as is shown for  $k = 2$  in Fig. 3.1(a). At  $k = \infty$ , these symmetric and antisymmetric states are twofold degenerate (see the two wavefunctions corresponding to the solid square in Fig. 3.1(a)). Due to this degeneracy any linear combination of these states is also an eigenstate. If we take the following linear combination

$$\begin{aligned} |m_+\rangle &= \frac{1}{\sqrt{2}} (|2m\rangle + |2m+1\rangle), \\ |m_-\rangle &= \frac{1}{\sqrt{2}} (|2m\rangle - |2m+1\rangle), \end{aligned} \quad (3.19)$$

we arrive at the well known Landau states, i.e. wavefunctions of electrons located in two different homogeneous magnetic field profiles. One electron is moving clockwise, while the other is moving counterclockwise. For decreasing

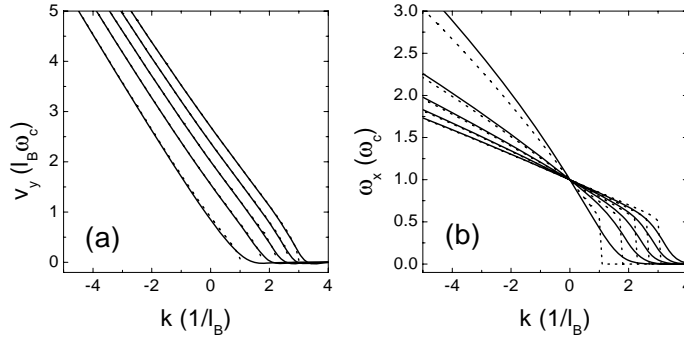


Fig. 3.9 (a) The quantum mechanical velocity in the  $y$ -direction (solid curves) of the time dependent states for the case  $B^l = -B^r = -1$  and the velocity obtained classically (dotted curves). (b) The same as in (a) but now for the oscillation frequency in the  $x$ -direction.

$k$  this degeneracy is lifted. Although taking linear combinations of states with a different energy yields a time dependent solution, we will extrapolate this picture towards all the other states. We choose a new orthonormal but time dependent basis:

$$\begin{aligned} |m_+\rangle &= (e^{iE_{2m}t}|2m\rangle + e^{iE_{2m+1}t}|2m+1\rangle) / \sqrt{2} \\ |m_-\rangle &= (e^{iE_{2m}t}|2m\rangle - e^{iE_{2m+1}t}|2m+1\rangle) / \sqrt{2} \end{aligned} \quad (3.20)$$

with  $E_{m_+} = E_{m_-} = (E_{2m} + E_{2m+1})/2$ . The resulting energy spectrum is shown in Fig. 3.2(a) by the dashed curves. The corresponding velocities are plotted in Fig. 3.9(a). For every branch there are two states  $|m_+\rangle$  and  $|m_-\rangle$ .

With these new quantum states much better agreement is obtained with the corresponding classical results (dotted curves in Fig. 3.9(a)). Because of the addition of the two eigenstates the negative velocity almost disappeared. Only the lowering of the energy, as was mentioned in the limiting case (i.e.  $k \rightarrow \infty$ ), results in a small negative velocity, which can't be understood even in this picture. Also the boundary which indicates when classical states propagate is in much better agreement now.

Since we now have time dependent states, we can calculate a new feature: the oscillation frequency  $\omega_x$  in the  $x$ -direction. The time dependent probability densities of the  $|m_+\rangle$  and  $|m_-\rangle$  states have the following form:

$$\begin{aligned} |\langle m_+|x\rangle(t)|^2 &= \frac{1}{2}(|\langle 2m|x\rangle|^2 + |\langle 2m+1|x\rangle|^2 \\ &\quad + 2\cos[\omega_x t]\langle 2m|x\rangle\langle 2m+1|x\rangle), \\ &= |\langle m_-|x\rangle(t + \pi/\omega_x)|^2, \end{aligned} \quad (3.21)$$

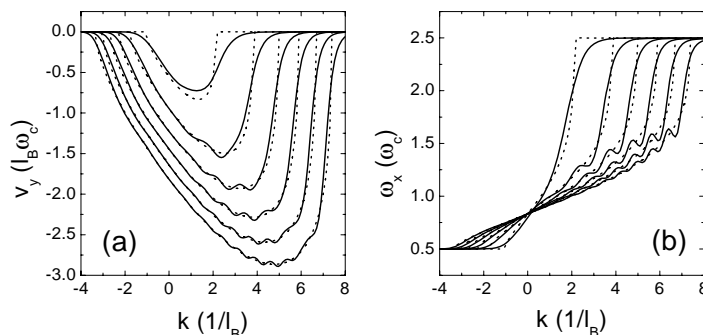


Fig. 3.10 The same as in Fig. 3.9, but now for the magnetic field profile with  $(B^l, B^r) = (0.5, 2.5)$ .

where  $\omega_{x,m} = (E_{2m+1} - E_{2m})/\hbar$  is the quantum mechanical oscillator frequency in the  $x$ -direction.

Classically we can calculate this frequency  $\omega_x$ , again using simple geometrical considerations, which results in

$$\omega_x(k) = \frac{\pi}{2 \arccos(-k/v_\varphi(k))}. \quad (3.22)$$

Both results are plotted in Fig. 3.9(b), and we obtain reasonably good agreement between the quantum (solid curves) and classical (dotted curves) results. Notice that for  $|k| > k^*$ , classically  $\omega_x = 0$ , which means that the electron does not oscillate between the two different magnetic field regions (i.e. it is not a snake orbit state), but it oscillates in a homogeneous magnetic field and consequently we obtain the time independent eigenstates corresponding to the Landau levels.

Of course this approach is only useful if proper linear combinations are possible. Unfortunately this is not the case when a background magnetic field  $B \leq B_0$  is applied.

### 3.6.2 $B > B_0$

The above approach is also fruitful in the case when  $0 < B^l < B^r$ . We can again add adjacent levels, two by two, similar as described before. We can repeat exactly as was done before, and we arrive again at the time dependent states of Eq. (3.20). The energy spectrum of these states when  $B = 3B_0/2$  is shown in Fig. 3.2(d), by dashed curves. From Fig. 3.10(a), we notice that the classical velocity is in better agreement than before, since the amplitude of the wiggles is lowered, due to the summation. The quantum mechanical oscillation frequency in the  $x$ -direction is again given by  $\omega_{x,m} = (E_{2m+1} - E_{2m})$  and

plotted in Fig. 3.10(b). We notice that since there are no degenerate states, we always have oscillating electrons. For  $k \rightarrow \infty$  the electron oscillates with frequency  $\omega_x = 2.5\omega_c$ , while for  $k \rightarrow -\infty$  the electron oscillates with frequency  $\omega_x = 0.5\omega_c$ , i.e. the electrons circle around in their separate homogeneous magnetic fields. This can also be seen from the classical oscillation frequency in the  $x$ -direction, which is given by

$$\omega_x(k) = \pi \left[ \frac{\arccos(k/v_\varphi(k))}{B^l} + \frac{\arccos(-k/v_\varphi(k))}{B^r} \right]^{-1}. \quad (3.23)$$

Notice that also here wiggles in  $v_y$  are present (see Fig. 3.10(b)) which are not present in the classical results. It is clear that proper linear combinations can always be made, as long as  $B > B_0$ .

### 3.7 CONCLUSIONS

We studied the electron states near discontinuities in the magnetic field. Different 1D magnetic field profiles, i.e. steps, were considered. The quantum mechanical energy spectrum was obtained and the group velocity of the states was calculated. Their corresponding classical orbits were found and the propagating states which are located at the magnetic field discontinuity correspond to snake orbits. Quantum mechanical magnetic edge states were found which move along the magnetic field step in opposite direction to the classical snake orbits and which cannot be understood classically. We were able to construct non stationary quantum mechanical states which closely approximate the classical solution for the symmetrical case  $B^l = -B^r$  and for the more general case  $B^r > B^l > B_0$ .

The characteristics of the electron states, e.g. their energy, velocity and position, play an important role in the electron transport and in fact they are used as input in conductivity calculations. Recently Nogaret *et al.*[58] realized an experiment in which a ferromagnetic stripe was placed on top of a quantum wire parallel to the wire axis. If magnetized perpendicular, the fringe fields of the stripe induce an alternating magnetic field in the wire, and snake orbits propagate underneath its edges. As function of the applied background field, a resonance peak in the magneto- and the differential Hall resistance was measured, which was explained as due to the destruction of the snake orbits with increasing background magnetic field. We recently reviewed[78] this theoretical explanation and found that this picture has to be supplemented with the normal edge states in order to find the correct magnetic field position of the resonance peak.

In future experimental setups it might be possible to inject a chosen  $k$ -vector for a particular energy, by use of a sort of  $k$ -dependent filter, like Matulis *et al.*[67] suggested. This would allow to selectively populate the different orbital states.



# 4

---

## Scattering on circular symmetric magnetic profiles

*The quasi-bound and scattered states in a 2DEG subjected to a circular symmetric steplike magnetic profile, with zero average magnetic field are studied. We calculate the effect of a random distribution of such identical profiles on the transport properties of a 2DEG. We show that a nonzero Hall resistance can be obtained, although  $\langle B_z \rangle = 0$ , and in some cases it can even change sign as function of the Fermi energy or the magnetic field strength. The Hall and magnetoresistance show pronounced resonances apart from the Landau states of the inner core, corresponding to the so called quasi-bound snake orbit states.*

---

The results presented in this chapter were published as:

- J. Reijniers, A. Matulis and F. M. Peeters, *Physica E* **6**, 759 (2000).
- J. Reijniers, A. Matulis and F. M. Peeters, not published yet.

#### 4.1 INTRODUCTION

The response of a two-dimensional electron gas (2DEG) to a spatially inhomogeneous magnetic field has been the subject of considerable interest in recent years. In such systems the inhomogeneities in the magnetic field act as scattering centers for the 2DEG.

These inhomogeneous magnetic fields can be realized by growing a type-II superconducting film on top of a heterojunction, containing a 2DEG.[21] If a background magnetic field is applied, vortices will penetrate the 2DEG, where they form scattering centers. If the applied magnetic field is low, the vortices will be distributed randomly, due to the inhomogeneities in the superconducting film. Brey *et al.*[8] and Nielsen *et al.*[57] studied scattering on these vortices if distributed randomly, or if distributed on a periodic array.

In an alternative approach superconducting particles are deposited above a 2DEG. Due to the Meissner effect, magnetic flux will be expelled from the particles, which again results in a low magnetic field region underneath the superconductor. This was realized by Smith *et al.*,[86] who grew lead grains on top of a heterojunction.

A logic next steps would be to deposit ferromagnetic clusters as inhomogeneous magnetic field creators. This was realized by Ye *et al.*,[95] who grew Dy-micromagnets on top of a GaAs/AlGaAs heterostructure and recently Dubonos *et al.*[17] studied scattering of electrons on the stray field of a single Dy-magnet. This problem is essentially different from the earlier problems, because now, the average magnetic field strength is zero,  $\langle B_z \rangle = 0$ .

Preliminary results on this system were already presented in Refs. [68] and [74], where scattering on the stray fields of infinitesimally flat magnetic disks with perpendicular magnetization was studied. In this paper we extend and generalize these earlier results and study cylindrical symmetric steplike profiles, with average magnetic field zero. This enables us to classify the arising phenomena and understand its underlying physics. We will show that such a system can give rise to a nonzero Hall resistance, even though  $\langle B_z \rangle = 0$ . Moreover, such a system can give rise to quasi-bound states, similar to the ones studied by Kim *et al.*,[43] who investigated theoretically the modified magnetic dot, except that we deal with quasi-bound states, since the magnetic profiles are finite in extent.

We will model this magnetic field by

$$B(r < R_a) = B_a \quad (4.1)$$

$$B(R_a < r < R_b) = B_b \quad (4.2)$$

$$B(r > R_b) = 0, \quad (4.3)$$

with  $B_b = -B_a/[(R_b/R_a)^2 - 1]$ . As an example we plot in Fig. 4.1 the magnetic field profile (solid line) resulting from a ferromagnet with radius  $R_a$  and thickness  $d/R_a = 1$ , grown a distance  $h/R_a = 0.1$  above a 2DEG, as

shown in the inset. The dotted line represents the magnetic field according to our model, i.e.  $R_b/R_a \approx 2.8$ .

The parameters depend on the specific properties of the ferromagnetic material (as extent, thickness, magnetization, distance to the 2DEG). The resulting profile can also be affected by including superconducting strips, which expel the flux lines due to the Meissner effect and consequently can rearrange/guide the magnetic field lines.

We will first consider scattering on a single magnetic profile, and then calculate the response of the 2DEG to a random, homogeneous distribution of these (identical) profiles over the sample. The approach is along the lines presented by Nielsen and Hedegård in Ref. [57] which was based on the Boltzmann transport equation. The magnetic inhomogeneity is included as a scatterer, and not in the driving force, as was done in Ref. [29].

We will solve the problem classically in order to get a reference frame which holds in the limit of large energies. Then we will concentrate on the quantum mechanical behaviour, and study the bound states and their influence on the transport properties.

## 4.2 SCATTERING ON A SINGLE PROFILE

### 4.2.1 Classical scattering

Classically, the scattering on a magnetic field profile is determined by the solution of Newton's equation of motion with the force given by the Lorentz expression  $\mathbf{F} = e\mathbf{v} \times \mathbf{B}$  for a particle with charge  $e$ . Outside the profile the path is just a straight line, inside it is an arc of a circle with radius equal to the cyclotron radius in the respective magnetic field. This cyclotron radius is given by  $l_c = v/\omega_c$ , with  $v$  the velocity of the particle and  $\omega_c = eB/m$  the cyclotron frequency in the local magnetic field, which is  $B = B_a$  in the inner core or  $B = B_b$  in the outer region.

The geometry of the scattering process is determined by the following dimensionless parameters: (a)  $R_b/R_a$ , i.e., the ratio of the radii of the inner and the outer circle, and (b)  $l_a/R_a = (m/e)(v/B_a)$ , which is the ratio of the cyclotron radius and the radius of the center part. It is clear that because of geometrical considerations, it is impossible for a particle which was initially outside the magnetic profile to become trapped inside the magnetic profile.

We calculated the differential cross section numerically, by calculation of the different trajectories. The integrated cross section  $\sigma$  is equal to the total weight of impact parameters corresponding to particles which hit the magnetic profile. It is equal to the total diameter of the magnetic inhomogeneity  $\sigma = 2R_b$ , as is always the case in classical scattering.

In the limit of  $kl_a \rightarrow 0$ , the cyclotron radius is very small compared to  $R_b$ , and therefore the electron scatters on the magnetic profile as if it were bouncing off a hard wall. As a consequence the differential cross section is

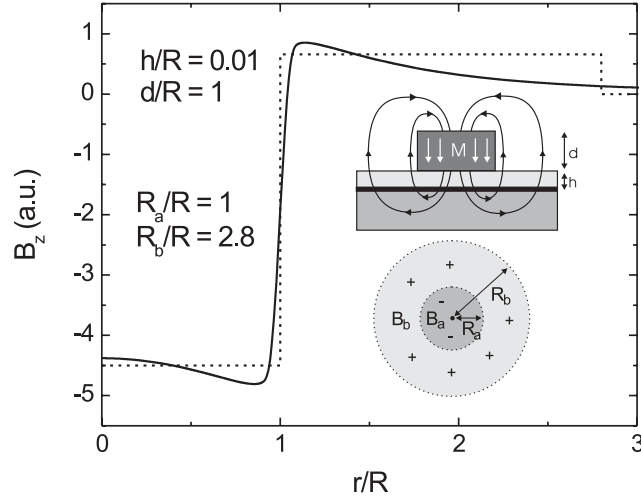


*Fig. 4.1* The magnetic field profile (solid line) and the theoretical model (dotted line) for a magnet of radius  $R$  and thickness  $d/R = 1$ , deposited a distance  $h/R = 0.01$  above a 2DEG, as shown in the inset. The theoretical values describing the theoretical model are also shown.

symmetric in  $\phi$ . If  $kl_a$  increases, the differential cross section changes drastically, and loses its symmetry due to the time reversal breaking magnetic field, as is clear from Fig. 4.2, where we show examples of these cross sections for the  $R_b/R_a = 1.5$  configuration for different  $l_a/R_a$ . The bold lines show the classical differential cross section, which we discuss now. We notice that  $d\sigma/d\phi$  is sensitive to  $kl_a$ : for increasing  $kl_a$  it is more centered around 0, as one would expect, but its structure also changes significantly. The different electron trajectories resulting in these  $d\sigma/d\phi$ -differences are shown on the right.

## 4.2.2 Quantum mechanical scattering

**4.2.2.1 The Schrödinger equation.** Because of cylindrical symmetry, we work with polar coordinates  $\mathbf{r} = (r, \varphi)$ . If we rescale the problem in the following way: length  $R_0 = R_a$ , energy  $E_0 = \hbar^2/(mR_a^2)$ , time  $t_0 = mR_a^2/\hbar$  and magnetic field  $B_0 = c\hbar/eR_a^2$ , we have to solve the following equation

$$(H - E)\Psi(r, \varphi) \quad (4.4)$$

with  $E = k^2/2$ . We can write the scattering wavefunction as follows

$$\Psi(r, \varphi) = R(r)\Phi(\varphi) = 0, \quad (4.5)$$

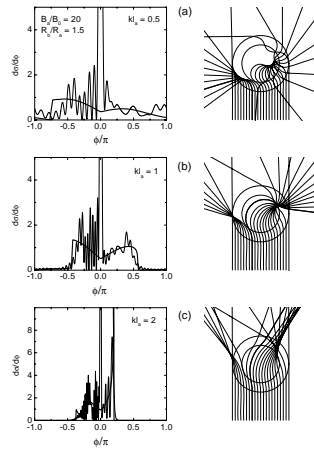


*Fig. 4.2* This figure corresponds with the situation  $B_a/B_0 = 20$  and  $R_b/R_a = 1.5$ . *On the left:* The differential cross section for different  $kl_a$ , i.e., (a)  $kl_a = 0.5$ , (b)  $kl_a = 1$ , and (c) for  $kl_a = 2$ . The bold curve corresponds to the classical result, the thin curve to the quantum mechanical result. *On the right:* Some classical trajectories interacting with the magnetic profile, giving rise to the differential cross sections on the left.

where the angular part equals

$$\Phi_m(\varphi) = \frac{1}{\sqrt{2\pi}} e^{im\varphi}, \quad (4.6)$$

since the problem is cylindrical symmetric. This results in the following equation for the radial part

$$\left[ -\frac{1}{2r} \frac{d}{dr} r \frac{d}{dr} + V_m(r) - E \right] R_m(r) = 0, \quad (4.7)$$

with

$$V_m(r) = \frac{1}{2} \left[ A_\phi(r) + \frac{m}{r} \right], \quad (4.8)$$

the effective potential and  $A_\phi = (1/r) \int_0^r dr' r' B(r')$  the radial component of the vector potential. We will assume that

$$V_m(r \rightarrow \infty) = \frac{m^2}{2r^2}, \quad (4.9)$$

such that at a large distance from the scatterer ( $r \rightarrow \infty$ ) the radial equation is the differential equation for Bessel function of the first kind

$$\left[ -\frac{1}{2r} \frac{d}{dr} r \frac{d}{dr} + \frac{m^2}{2r^2} - \frac{k^2}{2} \right] R_m(r) = 0, \quad (4.10)$$

with the well known solutions

$$R_m(r) = a_m J_m(kr) + b_m Y_m(kr), \quad (4.11)$$

where  $J_m(x)$  and  $Y_m(x)$  are Bessel functions of the first kind. Notice that the quantum numbers  $-\infty < m < \infty$ , in contrast to when the scatterers are non magnetic, in which we have  $0 \leq m < \infty$ , due to the symmetry.

We know that the scattering process is fully determined, if we know  $\delta_m$  for every  $m$ . In order to calculate this phase shift we have to solve Eq. (4.10) in presence of our magnetic profile, and compare the scattered wave with the unperturbed one. The solution for  $r < R_a$  is

$$R_{km}(r) = C r^{|m|} e^{-\frac{1}{2} B_a} M \left[ \frac{1}{2} [ |m| + 1 - m - \frac{(k)^2}{2B_a} ], |m| + 1, B_a r^2 \right], \quad (4.12)$$

where  $M(\alpha, \beta, \gamma)$  is the confluent hypergeometric function in the notation of Abramowitz and Stegun,[1] and  $C$  is a normalization constant. The solution for  $R_a < r < R_b$  is of the same form and should be matched at  $r = R_a$ . Instead of matching these two functions, we choose to calculate the wavefunction numerically up to  $r = R_b$ . The resulting phase shifts can be calculated at this point, and are derived from the condition that the logarithmic derivative of the radial wavefunction must be continuous at this boundary

$$\frac{1}{R^<} \frac{dR^<}{dr} \Big|_{r=R_b} = \frac{1}{R^>} \frac{dR^>}{dr} \Big|_{r=R_b}, \quad (4.13)$$

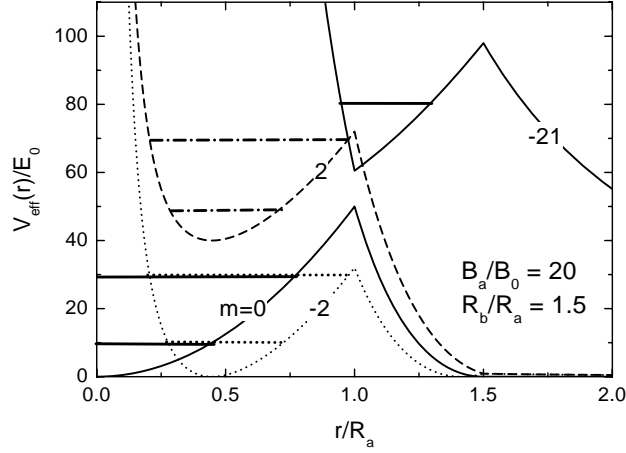


Fig. 4.3 The effective potential  $V_{eff}(r)$  as function of  $r/R_0$  for  $m$ -values, for the case  $B_a/B_0 = 20$  and  $R_b/R_a = 1.5$ . The horizontal lines correspond to the resonant energies.

which is

$$\frac{1}{R^<} \frac{dR^<}{dr} \Big|_{r=\alpha} = \frac{j_m - y_m \tan \delta_m}{J_m(kr) - Y_m(kr) \tan \delta_m}, \quad (4.14)$$

where we have introduced the abbreviations  $z_m = (kr/2)[Z_{m-1}(kr) - Z_{m+1}(kr)]$  with  $(z, Z) = (j, J)$  or  $(y, Y)$ . It is now easy to solve for  $\delta_m$

$$\tan \delta_m = \frac{j_m - E_m J_m(kr)}{y_m - E_m Y_m(kr)}. \quad (4.15)$$

**4.2.2.2 Resonances.** In contrast to the classical problem the ratio  $l_a/R_a$  is not sufficient anymore. We need to know the exact energy and the magnetic field strength. We have chosen to fix the  $B_a$ -value, and to plot the curves as function of  $kl_a$ . Doing so, they all have the same classical limit. The higher the  $k$ -value, the more classical the system is, and the more it converges to our previously obtained classical result. But for lower  $k$ -values, i.e., when the wavelength of the scattering wave is comparable to the dimensions of the scatterer  $1/k \approx R_b$ , quantum mechanics becomes important and results in features which cannot be understood classically, as the existence of resonances.

In order to determine at which energies these resonances occur, one should inspect the phase shift  $\delta_m$  as function of the energy or the corresponding  $k$ -vector. When a jump of  $\pi$  occurs, there is a resonance for that particular  $k$ -value for that  $m$ . The lifetime of that quasi-bound state depends on the

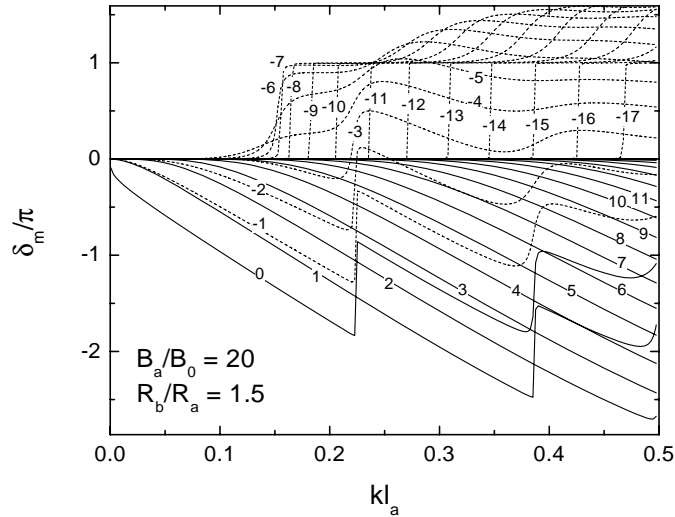


Fig. 4.4 The phase shift  $\delta_m$  as function of  $kl_a$  for different  $m$ -values, for the situation with  $B_a/B_0 = 20$  and  $R_b/R_a = 1.5$ . Phase jumps of  $\pi$  indicate resonant states.

energy-interval over which this jump occurs, or on the peak width of the partial cross section  $\delta_m$ .

In the following, we show the results for the case  $B_a/B_0 = 20$  and  $R_b/R_a = 1.5$ . In Fig. 4.3 we plot the effective potential for several  $m$ -values in this case. In Fig. 4.4 we plot the phase shift as function of  $k/l_a$  for  $-10 \leq m \leq 10$ .

We notice that for some  $m > 0$  quasi-bound states are formed at the Landau-levels of the inner core of the magnetic field profile, i.e. at  $k = \sqrt{B_a(2n+1)} = 4.471, 7.745, 10, \dots$ . Landau states in the outer region ( $B_b/B_0 = 16$ ) are not possible since the total extent of the lowest Landau state ( $= 2l_b = 2R_a/\sqrt{20} = 0.5R_a$ ) does not fit into the outer region ( $R_b - R_a = 0.5R_a$ ).

Nevertheless, for  $m < 0$  there are also resonances which have an energy lower than the first Landau level of the inner core. They correspond to quasi-bound snake orbit states, which travel around the profile, propagating from the  $B_a$ -region into the  $B_b$ -region and vice versa. As an example we plot the effective potential and the corresponding radial wavefunction  $R_m$  for  $m = -8$  in Fig. 4.5. Because the two wells are joined together, they form one well which is broader, and consequently the energy decreases. A similar effect we encountered in a previous paper,[77] this effect gave rise to snake orbits which do not have a classical counterpart. In this case, the electrons propagate classically as schematically depicted on the right hand side.

For higher energies we also notice resonances for  $m < 0$ . Also they correspond to snake orbits, but since they have a larger energy, they have to

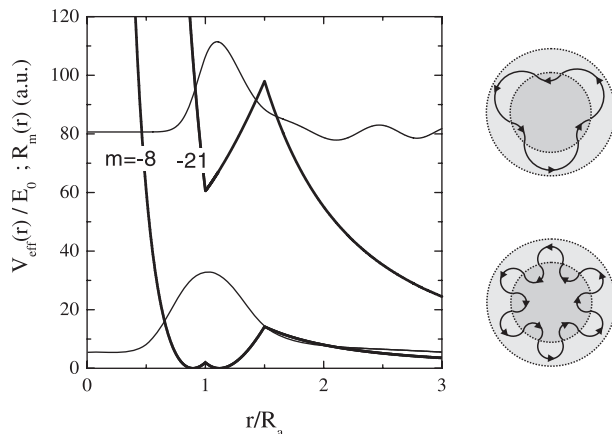


Fig. 4.5 The effective potential  $V_{eff}(r)$  as function of  $r/R_0$  for  $m = -8$  and  $m = -21$  when  $B_a/B_0 = 20$  and  $R_a/R_0 = 1.5R_0$ , together with the radial wavefunctions at resonant energies. These quasi-bound states correspond to different types of snake orbits, propagating parallel to the magnetic edge, as depicted schematically on the right side of the figure.

move closer to the interface, since their cyclotron radius is larger. The effective potential and the resonant scattering wavefunction for  $m = -21$  are also plotted in Fig. 4.5 together with the classical picture. These type of states will extinct, when the cyclotron radius in the outer part exceeds the radius of the outer part  $R_b$ , i.e. for  $kl_a \approx R_b/R_a = 1.5$ . We have checked this and these resonances indeed disappear.

**4.2.2.3 The total cross section.** In Fig. 4.6 we plot the total cross section as function of  $kl_a$ . We notice that the quantum mechanical cross section is larger than the classical result. For large energies the total cross section is twice as large, for small energies the cross section is four times as large, as is the case for any scatterer. We also notice the resonances mentioned before, present as small peaks, which can be attributed to a particular  $m$ -value. As an example, we indicated the  $m = -8$  and  $m = -21$  resonances, corresponding to the quasi-bound states of Fig. 4.5.

**4.2.2.4 The differential cross section.** In two dimensions, the differential cross section is given by

$$\frac{d\sigma}{d\phi} = \frac{2}{\pi k} \left| \sum_{m=-\infty}^{\infty} e^{im\phi} e^{-i\delta_m} \sin \delta_m \right|^2. \quad (4.16)$$

We plot this together with its classical counterpart in Figs. 4.2 (a-c). We notice that a lot of oscillations are present, due to interference effects. The

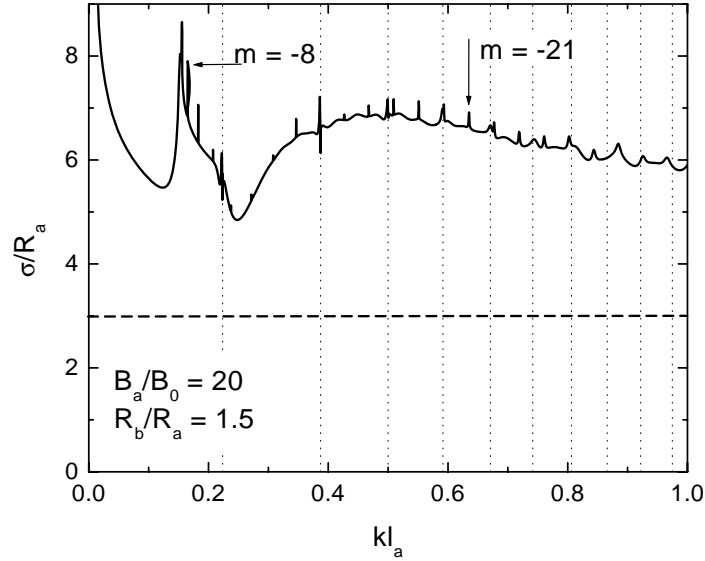


Fig. 4.6 The cross section  $\sigma_m$  as function of  $kl_a$  in the classical limit (dashed curve) and if calculated quantum mechanically (solid curve) for  $B_a/B_0 = 20$  and  $R_a/R_0 = 1.5$ . The marked resonant states correspond to the ones shown in Fig. 4.5 and Fig. 4.9. Vertical dotted lines are the Landau energies of the inner core of the magnetic field profile.

number of these oscillations depends on the energy: the larger the energy the more oscillations. In the high energy limit, the quantum mechanical result will ultimately, on the average, converge to the classical one, except for the peak at  $\phi = 0$ . Its occurrence is a purely quantum mechanical effect, and was already reflected in the total cross section, which is twice as large as classically. This is due to the fact that electrons which would classically pass by –and hence do not interact with– the scatterer, quantum mechanically have a finite overlap with the scatterer, and consequently contribute –although very little– to the cross section. Because the interaction is very little, they get scattered over a very small angle, and thus add to the  $\phi = 0$  peak.

### 4.3 SCATTERING ON MULTIPLE PROFILES

With the knowledge of the classical and quantum mechanical differential cross sections, it is now possible to calculate the Hall and magnetoresistance in a 2DEG subjected to a randomly distributed array of such identical profiles. In order to do this, we have to solve the Boltzmann equation.

### 4.3.1 Solution of the Boltzmann equation

We will make the assumption that the dimensions of the magnetic disks are small compared to the distance between the disks, so we do not include interference effects between different scattering events. Moreover we assume that the mean free path is larger than this inter-disk distance, for simplicity, we take it to be infinite.

Following the derivation as described in the paper of Nielsen and Hedegård,[57] we arrive finally at

$$\rho_{xx} = \frac{1}{(2\pi)^2} \frac{n_0}{n_e} \frac{\hbar}{e^2} \int_{-\pi}^{\pi} d\phi (1 - \cos \phi) w(k, \phi), \quad (4.17)$$

$$\rho_{xy} = \frac{1}{(2\pi)^2} \frac{n_0}{n_e} \frac{\hbar}{e^2} \int_{-\pi}^{\pi} d\phi \sin \phi w(k, \phi), \quad (4.18)$$

where  $n_e$  is the electron concentration,  $n_0$  is the concentration of magnetic scatterers and  $w(k, \phi)$  is the probability for an electron with wavevector  $k$  to be scattered over an angle  $\phi$ . In relation to the differential cross section, we can write  $w(k, \phi) = (\hbar k/m)(d\sigma/d\phi)$ , since  $\sigma v \Delta t$  is the probability for an electron with velocity  $v$  to interact with a scatterer with cross section  $\sigma$  in a unit of time  $\Delta t$ .

### 4.3.2 Classical result

**4.3.2.1 The magnetoresistance.** In Fig. 4.7, we plot the magnetoresistance as function of  $l_a/R_a$  for various  $R_b/R_a$ . The magnetoresistance is zero when  $l_a/R_a = 0$ , because for zero energy, electrons do not move ( $v = 0$ ) and consequently can not be scattered. For small values the magnetoresistance increases linearly up to a certain value after which it decreases for increasing  $l_a/R_a$ . This decrease is due to the fact that for higher energy, the electrons are less deflected because of a larger cyclotron radius in the magnetic inhomogeneity. We notice that for increasing  $R_b/R_a$  the magnetoresistance has an overall increase, on which we will focus a little further together with the Hall resistance, since the latter also exhibits this feature. The curves all show a minimum, which is more pronounced for small energies, due to the  $k$ -factor.

**4.3.2.2 The Hall resistance.** The corresponding Hall resistance is plotted in Fig. 4.8. We notice that both the qualitative and quantitative behaviour are more sensitive to  $R_b/R_a$  than was the case for the magnetoresistance. There are two striking features: (a) there is an overall increase of the Hall resistance with increasing  $R_b/R_a$ , and (b) when  $R_b/R_a$  is rather small, e.g.  $R_b/R_a < 1.5$ , the Hall resistance can change sign as function of  $l_a/R_a$ , i.e., as function of the Fermi-energy or the magnetic field strength.

The first feature can be explained by considering scattering on the inner and outer profile and how they influence each other. For larger  $R_b/R_a$ , the cyclotron radius of the outer part increases quadratically in  $R_b/R_a$  and there-

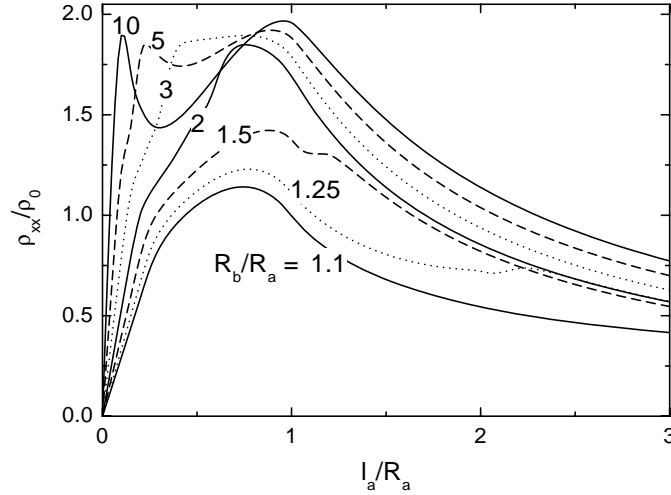


Fig. 4.7 The magnetoresistance in the classical limit as function of  $l_a/R_a$  for different  $R_b/R_a$ -configurations.

fore electrons will be less deflected for increasing  $R_b/R_a$ . However, this is compensated by the fact that the cross section also increases linearly with  $R_b/R_a$ , and consequently scattering on the outer part has more or less the same impact for different  $R_b/R_a$ . Nevertheless, the resistance increases, and this is due to the fact that for larger  $R_b/R_a$ , the scattering on the inner and the outer region can be considered as two separate processes, which only interfere very little. This is not the case for smaller  $R_b/R_a$ , where electrons interacting with the outer part are very likely to interact with the inner part, which deflects the electron in the opposite way, and thus diminishes the scattering effect produced by the outer part. In short we can say, that electrons which interact with the magnetic profile, on average “feel” a nonzero magnetic field which increases with increasing  $R_b/R_a$ , and this results in an increase of the magneto- and Hall resistance.

The fact that the Hall resistance can change sign when  $R_b/R_a < 1.5$  is a consequence of the interplay between scattering in the inner and the outer region. If  $l_a/R_a$  is small enough, such that  $2l_b < (R_b - R_a)$ , electrons cannot probe the center part. For infinitesimally small  $l_a/R_a$ , the outer part will act as a hard wall and consequently there is no Hall resistance. For increasing  $l_a/R_a$ , the electrons will penetrate deeper in the outer region, but not yet in the inner core [see for similar trajectory: the bold path in Figs. 4.2(a)]. The Hall resistance is that of a vortex with magnetic strength  $B_b$ . For increasing  $l_a/R_a$ , the electrons will be able to penetrate into the inner region, where they

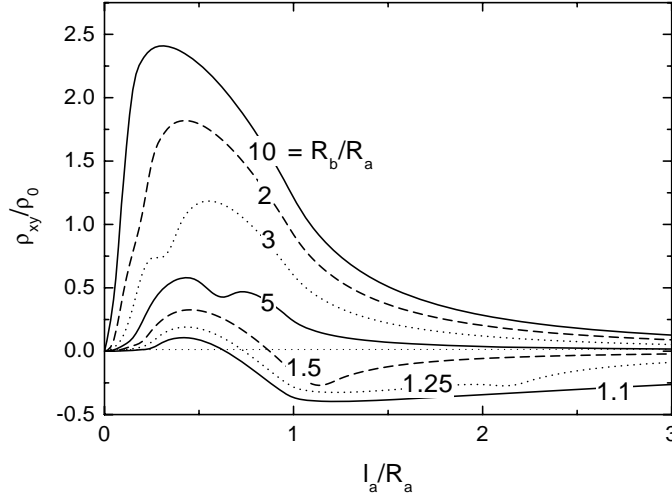


Fig. 4.8 The magnetoresistance in the classical limit as function of  $l_a/R_a$  for different  $R_b/R_a$ -configurations.

get deflected to the other side and the Hall resistance consequently changes sign [see the bold line in Figs. 4.2(b,c)]. For higher  $R_b/R_a$  the same effect can also take place, but only at very low energies, where the resistance is reduced for reasons, mentioned before.

### 4.3.3 Quantum mechanical result

We can rewrite the magnetoresistance and the Hall resistance as function of the phase shifts

$$\rho_{xx} = \frac{n_0}{n_e} \frac{\hbar}{e^2} \sum_{m=-\infty}^{\infty} 2 \sin^2(\delta_m - \delta_{m+1}) \quad (4.19)$$

$$\rho_{xy} = \frac{n_0}{n_e} \frac{\hbar}{e^2} \sum_{m=-\infty}^{\infty} \sin[2(\delta_m - \delta_{m+1})] \quad (4.20)$$

In Fig. 4.9, we plot the Hall and magnetoresistance as function of  $kl_a$  for  $B_a/B_0 = 20$  and  $R_b/R_a = 1.5$ . The solid curve is the quantum mechanical result, the dashed curve is our previously obtained classical result. We observe a lot of resonances, which diminish for increasing  $kl_a$ . Except for that, on the average there is rather good agreement between both curves, which is due to the choice of  $B_a/B_0$  being large, so with this axis ( $kl_a$ ),  $k$  –and consequently the energy– is large.

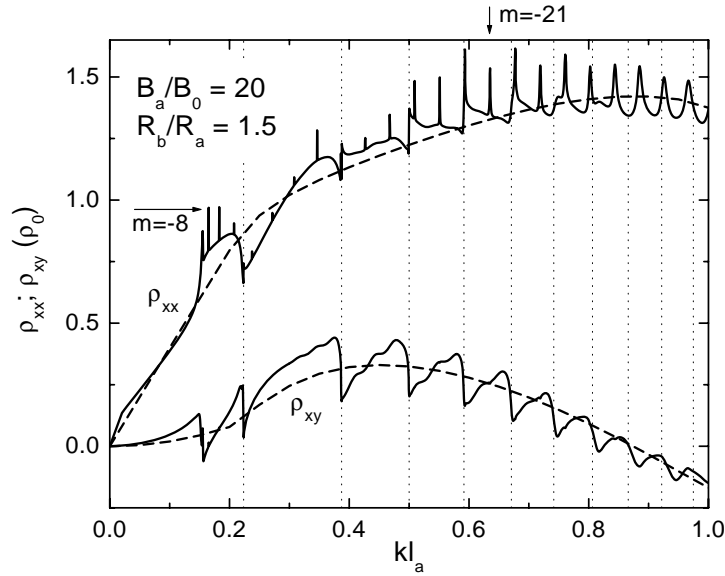


Fig. 4.9 The magneto- and Hall resistance as function of  $kl_a$  in the classical limit (dashed curves) and if calculated quantum mechanically (solid curves) for  $B_a/B_0 = 20$  and  $R_a/R_0 = 1.5$ . The marked resonant states correspond to the ones shown in Fig. 4.5 and Fig. 4.6, and the vertical dotted lines are the Landau energies of the inner core of the magnetic field profile.

There are two types of resonances: (1) those which occur at the energy of the Landau levels of the inner part (thin dotted lines), and (2) those corresponding to quasi-bound snake orbit states.

In case of the first type, the Hall resistance decreases abruptly, while the magnetoresistance increases. This is due to the fact that at the Landau levels, electrons are (quasi-) bound into cyclotron orbits, and hence cannot (1) contribute to the conduction, and consequently the magnetoresistance increases and (2) cannot pile up and generate a voltage difference on the left and right side, and consequently the Hall resistance decreases.

For larger energies, the cyclotron orbit in the center will increase and exceed the inner core classically at  $kl_a = 1$ . Nevertheless, quantum mechanically the electron will “feel” the presence of the outer magnetic field, and this will change the resonant energies. The resistance jumps are also less explicit for higher Landau levels, which is due to the reduced number of states which fit in the core as a result of the large cyclotron radius.

Apart from resonant states at the Landau levels, the magnetoresistance exhibits very sharp peaks, which correspond to the snake orbit states mentioned before. This second type resonances can have a lower energy than the

first Landau level of both the inner and outer part, as explained before. Since for all the snake orbit resonances only one quasi-bound state is involved (in contrast to the Landau states, where various bound states exist for various  $m$ -values, see Fig. 4.3), these peaks are very sharp and are superimposed on a more continuous background.

The influence of the quasi-bound snake orbit states is also visible in the Hall resistance, but not as clear as in the magnetoresistance. These quasi-bound states produce small changes in the slope of in the Hall resistance  $\rho_{xy}$ .

**4.3.3.1 Resonant states experimentally?** There are two competing effects which make experimental measurement of these resonances difficult: in order to detect these quasi-bound states, it is necessary that the energies (bound or resonant) are not too close to each other. To obtain this, one has to make a very small magnet (since  $E_0 = \hbar^2/mR_a^2$ ), but then one encounters the problem that in order to bind the electrons in such a small area one needs a very strong inhomogeneous magnetic field ( $B_0 = c\hbar/eR_a^2$ ), and currently no magnetic materials are available which can realize these strong fields. An example of such a system is the one by Dubonos *et al.*[17]: they managed to deposit a single Dy-magnet with radius  $\approx 0.1\mu\text{m}$  on top of a heterojunction, containing a 2DEG. Our units are given by  $E_0 = 7.63 \times 10^{-3}$  meV and  $B_0 = 0.066$  T. The Fermi energy in their system was about  $E_F = 17.86$  meV, which in our units is  $E_F = 2341E_0$  or  $k_F \approx 70$ . According to their paper, the stray field could locally generate a magnetic fields of  $B_a \approx 1T \approx 15B_0$ , which corresponds to  $k_F/B_a \approx 4.7$ , for which we are in the classical regime and the scattering process can be calculated classically.

In order to measure individual snake orbits, it is therefore necessary to include another confinement, which discretizes the energies and makes measurement possible.

A possibility could be an additional magnetic confinement, i.e., we could add a homogeneous background magnetic field in the  $z$ -direction, which localizes the electrons. Due to this the magnetic field inhomogeneity resulting from the magnetic material will be very small compared to the background field (the difference in cyclotron orbit will be very small), and this small difference will be reflected in the physics: a homogeneous magnetic field will probably be a good approximation. Another –more successful– possibility is by use of electrical confinement, as was also used in the paper by Nogaret *et al.*

If one does not include these additional confinement, discrete changes due to the inhomogeneous magnetic profile cannot be measured and the wavefunctions at the Fermi-level cannot be calculated due to the high number of oscillations, but it still has effect on the transport!

#### 4.4 CONCLUSIONS

In this paper we studied scattering on circular symmetric magnetic field profiles with zero mean magnetic field in the 2DEG. We considered scattering on a single profile, both classically and quantum mechanically, and discussed the quasi-bound states: the Landau-states in the inner core, and different quasi-bound snake orbit states. Next, we investigated the diagonal and Hall resistivity in the presence of a randomly distributed array of these magnetic profiles, using the kinetic equation of Boltzmann, for different magnetic field configurations. We obtain a nonzero Hall resistance although  $\langle B_z \rangle = 0$  and showed that the Hall resistance can change sign as function of the Fermi-energy or the magnetic field strength. We found that the electron resonances in the individual magnetic field profiles are reflected in the Hall and magnetoresistance.

# 5

---

## *Resistance effects due to magnetic guiding orbits*

*The Hall and magnetoresistance of a two dimensional electron gas subjected to a magnetic field barrier parallel to the current direction is studied as function of the applied perpendicular magnetic field. The recent experimental results of Nogaret et al. [Phys. Rev. Lett. **84**, 2231 (2000)] for the magneto- and Hall resistance are explained using a semi-classical theory based on the Landauer-Büttiker formula. The observed positive magnetoresistance peak is explained as due to a competition between a decrease of the number of conducting channels as a result of the growing magnetic field, from the fringe field of the ferromagnetic stripe as it becomes magnetized, and the disappearance of snake orbits and the subsequent appearance of cycloidlike orbits.*

---

The results presented in this chapter were published as:

- J. Reijniers and F. M. Peeters, Phys. Rev. B. (2001).

## 5.1 INTRODUCTION

Recently, there has been a growing experimental and theoretical activity directed towards an increased functionality of present day electronic devices. Previously, electrical potentials were used to modify the current, while more recently one became interested in the effects of magnetic field profiles, modulated or not, on the motion of electrons in semiconductor structures. The latter is usually a heterostructure which contains a two-dimensional electron gas (2DEG). Inhomogeneous magnetic field profiles in the 2DEG are created by depositing superconducting or ferromagnetic materials on top of the heterostructure which is then patterned in the desired shape using modern nanolithography.[65]

These hybrid systems are important from a theoretical and technological point of view, since they open the door to new physics which might result in e.g. new magneto-electronic devices.[16] An example of such a new device is the Hybrid Hall effect device [38, 75] in which the magnetic material provides a local magnetic field which influences locally the electron transport in the underlying 2DEG. The 2DEG then acts as a detector[66] measuring the magnetic state of the magnetic material.

The fringe field arising from a magnetic stripe forms a magnetic barrier for the electron motion in the 2DEG.[40, 47, 52, 53, 67, 91] Barriers can be created in which the sign of the magnetic field alters in different regions of space. Due to this magnetic gradient, electrons can be bound at the boundary line between two regions of opposite magnetic field. The spectrum and the corresponding magnetic edge states have been studied recently. [11, 33, 56, 67, 77, 98]

When an (1D) inhomogeneous magnetic field is applied across a quasi 1D wire, these magnetic edge states are confined electrically due to the wire confinement potential and they mix with the ordinary edge states.[26] Such a situation was recently realized by Nogaret *et al.*,[58] where the inhomogeneous magnetic profile was arising from a perpendicularly magnetized ferromagnetic stripe grown on top of the 2DEG. They measured the magneto- and Hall resistance as function of a background magnetic field, and observed a sharp resistance resonance effect, which they attributed to the formation and subsequent killing of magnetic edge states.

In the present work we give a detailed theoretical analysis of this experiment, using a semi-classical approach in which we consider the electrical and magnetic confinement quantum mechanically, and include scattering processes using classical arguments. Both, the measured Hall resistance and the magnetoresistance will be explained. We will show that the theoretical picture of Nogaret *et al.* only captures part of the physics which is involved and is unable to predict the correct position of the peak in the magnetoresistance and the Hall resistance.

The side and top view of the experimental setup of Nogaret *et al.*[58] are shown in Fig. 5.1. A Hall device consisting of a  $W = 2\mu\text{m}$  wide 2DEG channel

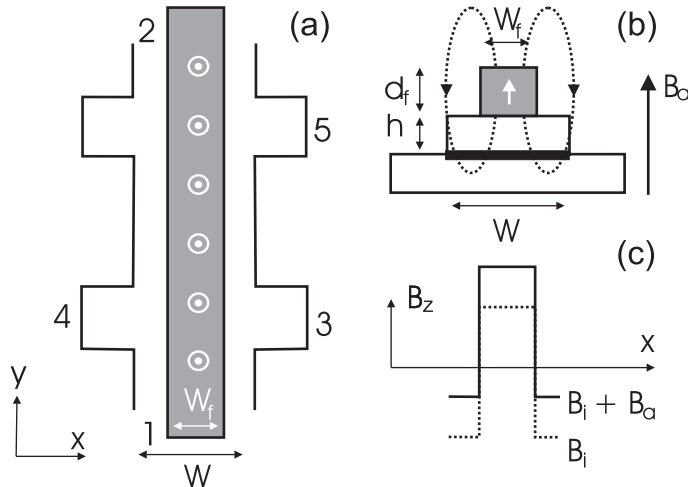


Fig. 5.1 The top (a) and side view (b) of the sample configuration used by Nogaret *et al.* [58]. In (c) the resulting (modeled) magnetic field profile in the wire is shown with  $B_i$  the magnetic field profile due to the fringe fields and  $B_a$  the uniform externally applied field.

in a GaAs/AlGaAs-heterojunction was fabricated, with electron density  $n_e = 1.94 \times 10^{15} \text{m}^{-2}$  and mean free path  $\ell = 4.5 \mu\text{m}$  at 4.2 K. A narrow ( $W_f = 0.5 \mu\text{m}$ )  $32 \mu\text{m}$  long ferromagnetic (Fe or Ni) stripe (thickness  $d_f = 200 \text{nm}$ ) was grown a distance  $h = 80 \text{nm}$  above the center of the electron channel.

The electron transport in the 2DEG is only influenced by the perpendicular component of the magnetic stray field. In absence of any background magnetic field the ferromagnetic stripe is magnetized along the easy axis, i.e. the  $y$ -direction, and the fringe field is situated outside the quasi 1D wire, i.e. in reservoir 1 and 2. Application of a perpendicular background magnetic field rotates the magnetization to align with the  $z$ -axis, and this will result in a stray field in the wire, which imposes a step magnetic field profile along the  $x$ -direction (see Fig. 5.1(b)). The actual magnetic field profile is slightly rounded (see Ref. [58]) but we checked that our results are not influenced by this simplification. This magnetic step adds an inhomogeneous magnetic field component to the uniform applied magnetic field  $B_a$  which induces the observed resistance effects. In the present analysis, we restrict ourselves to a Fe-stripe (saturation magnetization: 1.74 T), since this was studied most thoroughly in Ref. [58] and produced the most pronounced resonance effect.

This paper is organized as follows. In Sec. II we present our theoretical approach. In Sect. III we calculate the two terminal resistance as function of the applied background magnetic field. The Hall resistance is studied in Sect. IV and in Sect. V the magnetoresistance is calculated. We will discuss differences between our theoretical results and the experimental (and theoret-

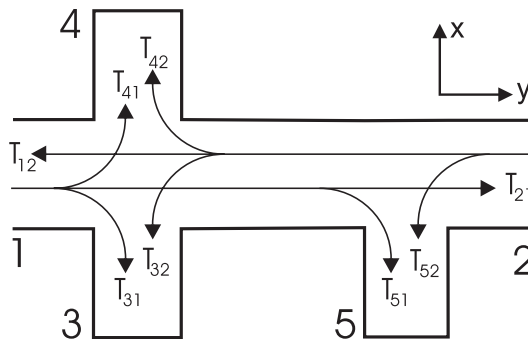


Fig. 5.2 Four-terminal configuration in a Hall (voltage probes: 3 and 4) and a magnetoresistance (voltage probes: 3 and 5) measurement. In a magnetic field the electron current flows along the edge. The different transmission probabilities are shown.

ical) results of Nogaret *et al.*[58] Our theoretical explanation for the observed resonance effect in the magnetoresistance deviates from the one proposed in Ref. [58]. In Sect. VI we summarize our conclusions.

## 5.2 THEORETICAL APPROACH

The magneto- and Hall resistance are measured experimentally by use of a *four-terminal* configuration. In contrast to the theoretical study of Nogaret *et al.*[58], we will retain this feature in the present discussion. The four-terminal configuration is schematically shown in Fig. 5.2 for (a) a Hall measurement and (b) a magnetoresistance measurement. The leads are in thermodynamical equilibrium and can be characterized by a chemical potential  $\mu_i$ . Each reservoir injects a current  $I_i$  of electrons into the 1D wire. If several bands are occupied, we have to consider a many-channel situation, and according to Büttiker, [9] the current in each of the leads is given by

$$I_i = \frac{e}{h} \sum_{n,n'} \left\{ [\delta_{n,n'} - R_{ii}(n, n')] \mu_i - \sum_{j \neq i} T_{ij}(n, n') \mu_j \right\}, \quad (5.1)$$

where  $T_{ij}(n, n')$  is the probability for an electron in channel  $n$  of lead  $i$  to be scattered/transmitted to  $n'$  of lead  $j$ . Current conservation requires  $N_i = R_{ii} + \sum_{j \neq i} T_{ij}$  for all  $i$ , with  $T_{ij} = \sum_{n,n'} T_{ij}(n, n')$  and  $R_{ii} = 1 - T_{ii}$  and  $N_i$  is the number of channels in lead  $i$ .

Each channel  $n$  contributes a probability  $T_{ij}(n) = \sum_{n'} T_{ij}(n, n')$  to the conductivity which is transmitted from probe 1 to probe 2. The total transmission from probe  $i$  to  $j$  then equals  $T_{ij} = \sum_{n \leq N} T_{ij}(n)$ , and Eq. (5.1) is

simplified to

$$I_i = \frac{e}{h} \sum_n \left\{ [1 - R_{ii}(n)] \mu_i - \sum_{j \neq i} T_{ij}(n) \mu_j \right\}. \quad (5.2)$$

In this type of measurement, only two probes are current carrying, i.e.,  $i = 1, 2$ , which results in the condition  $I_1 = -I_2 = I$  while the other probes are voltage probes and do not carry any net current:  $I_3 = I_4 = I_5 = 0$ .

In order to calculate the four-terminal magneto- and Hall resistance, we will make another simplifying assumption that the voltage probes are weakly coupled ( $T_{ij} \ll T_{i1}, T_{i2}$  for  $i, j = 3, 4, 5$ ), their influence on the net current  $I$  is very small ( $I = (\mu_1 - \mu_2)/eR_{12,12}$ ) and the chemical potentials in each of the voltage probes can be calculated in the absence of the other voltage probes ( $\mu_i = (T_{i1}\mu_1 + T_{i2}\mu_2)/(T_{i1} + T_{i2})$  with  $i = 3, 4$ ). The general formula for this kind of resistance measurement is then readily obtained and given by

$$\begin{aligned} R_{12,3i} &= \frac{\mu_3 - \mu_i}{eI} = \frac{h}{e^2} \frac{1}{T_{12}} \frac{T_{31}T_{i2} - T_{32}T_{i1}}{(T_{31} + T_{32})(T_{i1} + T_{i2})} \\ &= \frac{h}{e^2} \frac{1}{T_{12}} F = R_{12,12} F, \end{aligned}$$

which is the two terminal resistance  $R_{12,12}$  multiplied with a geometrical form factor  $F$ , which is less than one.

In the following we will first calculate the two-terminal resistance  $R_{12,12}$  and then concentrate on the geometrical form factor  $F$  in the case of a Hall or magnetoresistance measurement.

### 5.3 THE ENERGY SPECTRUM AND THE TWO-TERMINAL RESISTANCE

The two-terminal resistance is given by  $R_{12,12} = (\mu_2 - \mu_1)/eI$ . We know that in the absence of any collisions, the current which flows from reservoir 1 to 2 is determined by the number of subbands  $N$  which are occupied at the Fermi level. Since the mean free path in the experiment of Nogaret *et al.*[58] is  $\ell = 4.5\mu\text{m}$ , which is larger than the wire width ( $W = 2\mu\text{m}$ ), we can, to a good approximation, neglect the influence of scatterers on the spectrum and calculate the number of channels quantum mechanically following the work of Müller[56] for a pure quasi 1D quantum wire.

We consider a system of noninteracting electrons moving in the  $xy$ -plane subjected to a hard wall confinement  $-W/2 < x < W/2$ , where  $W$  is the width of the wire. The electrons are subjected to a magnetic field profile  $\vec{B} = (0, 0, B_z(x))$ . This profile equals  $B_z = B_i(B_a) + B_a$ , where  $B_a$  is the uniform applied background field and  $B_i$  is the induced magnetic field profile due to the magnetized stripe.

In correspondence with Ref. [58] we will model the shape of the induced magnetic field profile by the average magnetic field on the respective sides of the magnetic stripe edges, i.e. at saturation the magnetic field profile is given by  $B_{sat} = B_1 + (B_2 - B_1)\theta(|x| - W_f/2)$ , where  $\theta$  is the heavyside step function and  $B_1 = 0.28$  Tesla and  $B_2 = -0.06$  Tesla are the modeled magnetic field strengths underneath and away from the stripe as shown in Fig. 5.1(c). We also performed the calculations for the exact magnetic field profile, but this resulted in negligible small quantitative differences.

We model the magnetization of the stripe by considering two limiting cases: (A) when the stripe is already magnetized at  $B_a = 0$  Tesla (as was considered by Nogaret *et al.*), i.e.  $B_i = B_{sat}\text{sign}(B_a)$  which is the hard magnet case, and (B) when the applied magnetic field magnetizes the stripe as for soft magnets. In case (B) we assume  $B_i$  to be linearly varying with applied background magnetic field  $B_a$ , up to  $B_a = 0.05$  Tesla, where saturation is attained according to Ref. [58]. The induced magnetic field is then given by  $B_i = B_{sat}\{1 - [1 - \theta(|B_a| - 0.05)](1 - |B_a|/0.05)\}$ . The actual experimental behaviour is expected to be situated closer to situation (B) than to (A).

The one-particle states are described by the Hamiltonian

$$H = \frac{1}{2m_e}p_x^2 + \frac{1}{2m_e} \left[ p_y - \frac{e}{c}A(x) \right]^2 + V(x), \quad (5.3)$$

where  $V(-W/2 < x < W/2) = 0$  and  $V(x < -W/2) = V(x > W/2) = \infty$ . Taking the vector potential in the Landau gauge  $\vec{A} = (0, A_y(x), 0)$ , such that  $\partial A_y(x)/\partial x = B_z(x)$ , for which we took  $A_y(x) = \int_0^x B_z(x')dx'$ , we arrive at the following 2D Schrödinger equation

$$\left\{ \frac{\partial^2}{\partial x^2} + \left[ \frac{\partial}{\partial y} + A_y(x) \right]^2 + 2[E - V(x)] \right\} \psi(x, y) = 0, \quad (5.4)$$

where the magnetic field is expressed in  $B_0$ , magnetic units are used for a homogeneous field of  $B_0 = 1$  Tesla, i.e., all lengths are measured in  $l_0 = \sqrt{\hbar c/eB_0} = 0.0257\mu m$  and energy is measured in units of  $E_0 = \hbar eB_0/m_e c = 1.7279meV$ .  $H$  and  $p_y$  commute due to the particular choice of the gauge, and consequently the wavefunction becomes

$$\psi(x, y) = \frac{1}{\sqrt{(2\pi)}} e^{-iky} \phi_{n,k}(x), \quad (5.5)$$

which reduces the problem to the solution of the 1D Schrödinger equation

$$\left[ -\frac{1}{2} \frac{d^2}{dx^2} + V_k(x) \right] \phi_{n,k}(x) = E_{n,k} \phi_{n,k}(x), \quad (5.6)$$

where it is the  $k$ -dependent effective potential

$$V_k(x) = \frac{1}{2} [A_y(x) + k]^2 + V(x), \quad (5.7)$$

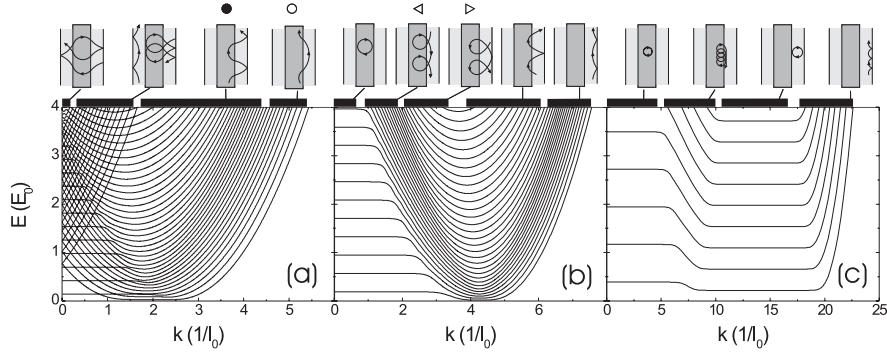


Fig. 5.3 The energy spectrum in case (A) as function of  $k$  for (a)  $B_a/B_0 = 0$ , (b) 0.1, and (c) 0.5. The classical trajectories for  $\epsilon_F = 4E_0$  are schematically shown on top of the figures for the  $k$ -range indicated by the solid bars. The darker area in these insets correspond to the position of the magnetic stripe.

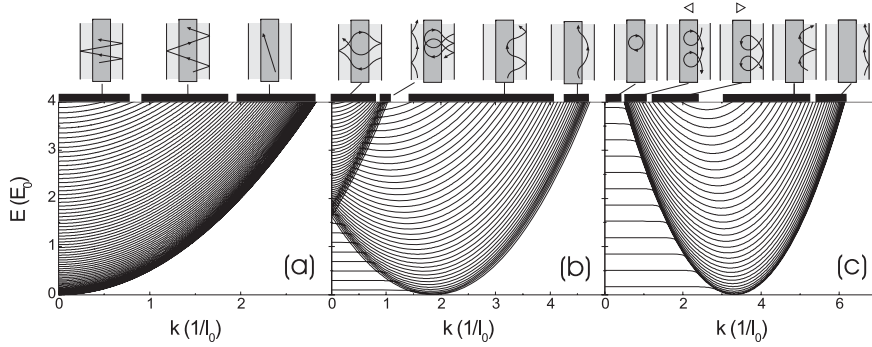


Fig. 5.4 The same as in Fig. 5.3, but now for case (B) for (a)  $B_a/B_0 = 0$ , (b) 0.03 and (c) 0.06.

which contains the two dimensionality of the problem.[67] We solve Eq. (5.6) numerically by use of a discretization procedure.

For given applied background magnetic field we calculated the energy spectrum for case (A) with  $W = 2\mu m$ . The results are shown in Fig. 5.3 for  $B_a/B_0 = 0; 0.1; 0.5$ . These energy spectra are symmetric in  $k$  and for small  $B_a$  consist of the superposition of two parabolic spectra. For small  $k$ -values and for energies below the intersection of the two parabolas Landau levels are present due to electrons which are bound underneath the stripe. These

levels shift away from each other as the background magnetic field increases, due to the increase of the magnetic field underneath the stripe ( $B_1$ ). For increasing magnetic field the two parabolas shift further away from each other, towards higher  $|k|$  values. Due to the confinement of the wire, each parabola is infinitely duplicated, where its maximum is shifted to higher energy and to lower  $k$ -values. For higher magnetic fields ( $B_a > 0.5B_0$ ) Landau levels arise, due to the magnetic field away from the stripe ( $B_2 < B_1$ ) which is now strong enough to localize electrons into cyclotron orbits.

The classical trajectories (for  $E = 4E_0$ ) corresponding to the different regions in  $k$ -space are shown on top of Fig. 5.3. We restricted ourselves to trajectories of states at energy  $E = 4E_0$ , since the experiment was performed at  $\epsilon_F = 6.9\text{meV} \approx 4E_0$  and at zero temperature only channels with this energy contribute to the conductivity. We obtained these classical trajectories by inspection of the electron density distribution  $|\phi_k(x)|^2$  and the effective potential  $V_k(x)$ , and by comparison of the sign of the quantum mechanical velocity in the  $y$ -direction ( $v_y = -\partial E_k / \partial k|_{\epsilon_F}$ ) with the one from our classical orbit.

For (B) the spectrum at  $B_a/B_0 = 0; 0.03; 0.06$  and the corresponding classical orbits at the Fermi energy are shown in Fig. 5.4. For  $B_a = 0$  the magnetic stripe is not magnetized and the spectrum consists only of the potential confined levels. One single parabola (and its duplicates due to confinement) centered around  $k = 0$  is found which splits into two and its center shifts towards higher  $|k|$ -values. Below the intersection of the two shifted parabolas Landau states are formed. Notice that some levels intersect the Fermi energy twice as much as before. These Landau states separate further away from each other for increasing magnetic field. For  $B_a \geq 0.05B_0$  the spectra are identical to the ones of (A).

The current is given by

$$I = \frac{e}{h} T_{12}(\mu_i - \mu_j) \quad (5.8)$$

with  $T_{12} = \sum_{n < N} T_{12}(n)$ . In the absence of any collisions  $T_{12}(n) = 1$ , and consequently  $T_{12} = N$ , where  $N$  is the number of conducting channels, i.e. the energy levels intersecting the Fermi energy.

Nevertheless, the mean free path measured by Nogaret *et al.* is smaller than the length of the wire  $L_y = 16 \mu\text{m}$  and also smaller than the distance between the probes. Thus, scattering will play an important role in electron transport and consequently  $T_{12}(n)$  will be less than 1. In order to account for this, we will estimate the transmission coefficient for every channel using classical arguments. Since we consider the voltage probes as weakly coupled, they result in a very weak perturbation of the electron-current path, and scattering due to the voltage probes will be neglected. The only scattering we consider is due to collisions with impurities and other imperfections in the 1D-channel.

The rate at which these collisions occur depends classically on the velocity in the  $y$ -direction, the length of the wire and the scattering time. The lower the velocity in the  $y$ -direction, the longer it takes to overcome the distance between probe 1 and probe 2, and the more probable it will be to experience a scattering event. Because of this we consider the transmission probability of every channel to be proportional to its velocity  $v_y = -\partial E_n(k)/\partial k|_{\epsilon_F}$  and the scattering time  $\tau$ , and inversely proportional to the length  $L_y$  of the wire, i.e.,

$$T_{12}(n) \sim \frac{v_y(n)\tau}{L_y}. \quad (5.9)$$

So finally, we arrive at the two terminal resistance

$$R_{12,12} = \frac{1}{\alpha} \frac{h}{e^2} \frac{1}{\sum_n v_y(n)}, \quad (5.10)$$

where  $n$  runs over all the  $N$  electron states with positive velocity (or negative velocity) at the Fermi energy  $\epsilon_F$ , and  $\alpha$  is a function of  $L_y$  and  $\tau$ .

First we will discuss the change of the two-terminal resistance  $R_{12,12}$  with respect to the situation in absence of the ferromagnetic stripe  $R_{12,12}^0$ , which we will call the *induced* resistance  $R_{12,12}/R_{12,12}^0$ . This property was also calculated and discussed by Nogaret *et al.*, [58] and is plotted in Fig. 5.5 as function of the applied magnetic field  $B_a$  for the approach of Ref. [58] (dashed curve) and ours (dotted and solid curves). The zero temperature result is shown in the inset.

We notice that at zero temperature, many discontinuous jumps are present. As we will see further on, their position is very sensitive to the Fermi-energy and they disappear at 4.2 K. The energy distribution function  $f(E, T) = \{\exp[(E - \epsilon_F)/k_B T] + 1\}^{-1}$  is not a stepfunction for nonzero temperature and consequently also electrons with energy different from  $\epsilon_F$  will contribute to the conductivity. This smoothes out these oscillations at 4.2 K, as is shown in Fig. 5.5. Also the broadening of the energy levels due to e.g. potential fluctuations will have such a smoothing effect on the resistance curves at nonzero temperature. Hence, we will only show the (smooth) curves at 4.2 K in the next figures.

The curves (A) and (B) differ only for  $B_a < 0.05B_0$ . In case (A) the resistance for  $B_a = 0$  is larger than in the absence of the magnetic stripe. Increasing the background magnetic field results in a slight overall increase of the induced resistance. At  $B_a = 0.02B_0$  the induced resistance reaches its maximum, then it decreases rapidly.

The induced resistance in case (B) starts at 1 for  $B_a = 0$ , increases more rapidly and attains its maximum at a slightly higher  $B_a$ -value, i.e.,  $B_a = 0.0375B_0$ . Then it decreases rapidly up to  $B_a = 0.2B_0$ . We again notice oscillations at zero temperature (see inset), but fewer than for case (A). For larger  $B_a$ -values the oscillations disappear and the scaled resistance increases ultimately to one.

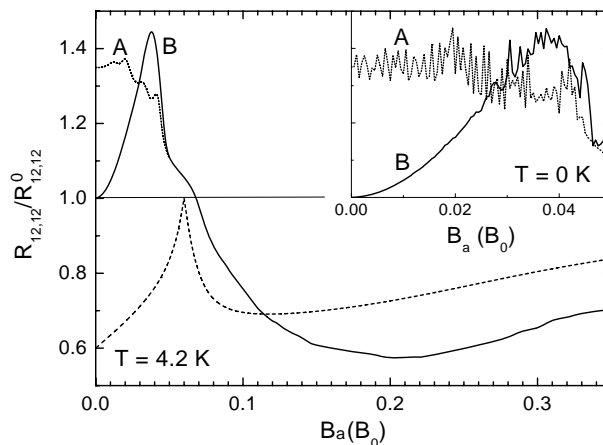


Fig. 5.5 The induced two point resistance  $R_{12,12}/R_{12,12}^0$  at 4.2 K as function of  $B_a$  for case (A) (dotted curve) and case (B) (solid curve), and according to the approach of Nogaret *et al.* (dashed curve). The inset shows the zero temperature induced resistance.

Nogaret *et al.*[58] obtained theoretically a somewhat similar behaviour, as is indicated by the dashed curve, except for the peak which was situated at a slightly higher value  $B_a = 0.06B_0$ . They made the assumption that the stripe was already fully magnetized at  $B_a = 0$  like in our case (A). Moreover they considered the magnetoresistance for a homogeneous magnetic field profile with magnetic field strength  $B_a$ , and considered the effect of the magnetic stripe profile by adding classical trajectories of states which arise due to the presence of the stripe. In order to simplify the problem, they only considered states which do not reach (classically) the edge of the sample. They attributed the initial positive magnetoresistance to *snake orbits* (see situation “o” in Fig. 5.3(a)) which are killed with increasing magnetic field and therefore no longer contribute to the conductivity for larger fields. At  $B_a = 0.06B_0$  all snake orbits have vanished and it is due to this, they inferred, that the resistance reaches its maximum. However if the magnetic field is larger than  $0.06B_0$ , the magnetic field has the same sign over the whole sample but has different strength under the stripe and away from it, and a new type of magnetic edge states, so called *cycloidlike* states (see the states indicated by “◁” in Fig. 5.3(b)), arises, which again enhances conductivity and thus lowers the resistance. The fact that the influence of the latter orbits vanishes for larger  $B_a$ -values is due to the decrease of the velocity of these states with decreasing relative difference between the two neighboring magnetic fields.

In case (A), when the saturation magnetization is already attained at  $B_a = 0$ , we cannot attribute the existence of the (small) peak to the creation or annihilation of a certain classical state. Fig. 5.3 shows the energy spectrum and the corresponding classical states at the Fermi-energy  $\epsilon_F = 4E_0$  for (a)  $B_a = 0$ , (b)  $B_a = 0.1B_0$  and (c)  $B_a = 0.5B_0$ . From this figure we see that the enhancement of the resistance is a pure quantum mechanical effect and involves many different types of states with different velocities. Therefore an explanation based on the appearance or disappearance of only snake orbits as done by Nogaret *et al.* is not possible, at least for small  $B_a$ . The discontinuous behaviour for small  $B_a$  (see the inset in Fig. 5.5) is due to edge states at the Fermi-level whose energy moves through the Fermi level and then no longer contribute to the conduction. They have nonzero velocity and hence this is also reflected in the resistance. For larger  $B_a > 0.05B_0$  the curve coincides with the one of case (B).

In case (B), the initial magnetoresistance can be understood more easily. For  $B_a = 0$ , the stripe is not yet magnetized and thus there is no effect of the magnetic stripe. Fig. 5.4(a) shows subbands formed due to the quasi 1D confinement ( $N = 70$  subbands contribute to the conduction). Already for a small applied magnetic field, a relative large magnetic field is induced in the wire due to the magnetization of the ferromagnetic stripe. Whereas, for  $B_a = 0$  the only confinement was due to the edges of the sample, the magnetic field ( $B_1 + B_a$ ) tends to localize electrons into cyclotron orbits and thus forces them in Landau levels, which separate further in energy with increasing magnetic field. As a consequence less channels will intersect the Fermi-level and consequently less channels contribute to electron transport and the resistance increases.

But there is a competing effect due to the presence of the magnetic stripe which tends to lower the induced resistance: from Figs. 5.3(b,c) one notices that for higher  $B_a$  some subbands hit the Fermi-energy twice instead of once. New edge states arise (see the states indicated by “ $\leftarrow$ ” and “ $\rightarrow$ ” in Figs. 5.3 and 5.4) which travel in the opposite direction of the normal edge states. The birth of these new backwards propagating states enhances the conductivity and overcomes the previous decreasing effect at  $B_a = 0.0375B_0$ , and the induced resistance decreases. This effect contributes even for  $B_a > 0.06B_0$ , when the magnetic field has the same sign in the whole wire, and the previously mentioned cycloidlike orbits appear. For increasing magnetic field their influence decreases, although their number with respect to normal edge states increases. This is due to their velocity, which decreases for increasing  $B_a$  for reasons given by Nogaret *et al.*

In the following sections, we will try to reproduce the experimental results obtained by Nogaret *et al.* First we will concentrate on the Hall resistance, before we focus on the magnetoresistance.

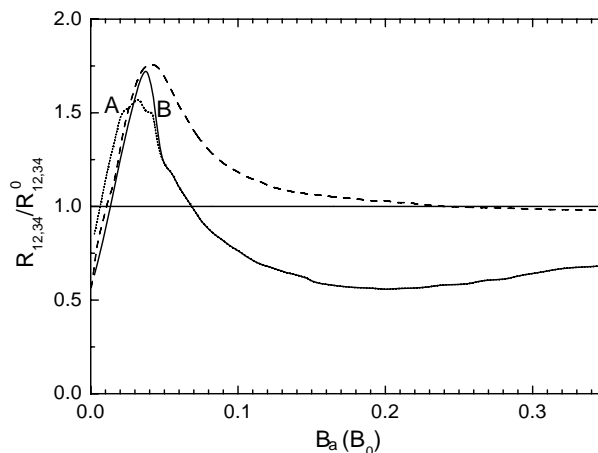


Fig. 5.6 The induced Hall resistance  $R_{12,34}/R_{12,34}^0$  as function of the applied magnetic field  $B_a$  as measured experimentally by Nogaret *et al.* (dashed curve) and our theoretical result for case (A) (dotted curve) and case (B) (solid curve).

#### 5.4 THE HALL RESISTANCE

In order to calculate the magneto- and Hall resistance we will further simplify the problem, by making the assumption of symmetrical probes. In case of the Hall resistance, the two voltage probes, i.e. probe 3 and 4, are in front of each other as is clear from Fig. 5.2, and due to this symmetry the transmission probabilities can be written as  $T_{31} = T_{42} = T$  and  $T_{32} = T_{41} = t$ . The Hall resistance then attains a very simple form

$$R_{12,34} = \frac{1}{\alpha} \frac{h}{e^2} \frac{1}{T_{12}} \frac{(T/t - 1)}{(T/t + 1)}, \quad (5.11)$$

as was already derived in Ref. [61]. Note that there is additionally one parameter  $\alpha$  and one function  $t/T$  which describe the behaviour of the Hall resistance. In the absence of any magnetic field  $t/T = 1$ , and consequently the Hall resistance reduces to zero. As the cyclotron radius decreases, electrons will be localized closer to the edge (in edge states) and consequently the probability for an electron *bouncing* on one edge to be transmitted in a probe on the other side of the wire decreases drastically, i.e. exponentially, with increasing magnetic field, as can be inferred from Ref.[61]. Consequently  $t/T$  will decrease rapidly and ultimately for already a small applied magnetic field the geometrical form factor  $F = (T/t - 1) / (T/t + 1)$  will be 1 in which case the Hall resistance equals the two-terminal resistance  $R_{12,12}$ .

In order to obtain qualitative agreement with experiment, we follow Ref. [62] and take the following functional form for  $t/T = \exp[-25B_a - (35B_a)^2]$  with  $B_a$  expressed in Tesla. If we take  $R_{12,34}^0(B_a) = (3669.4 * B_a)\Omega$  as the functional form of the Hall resistance in absence of the magnetic stripe, which we obtained from a linear fit of the experimental result by Nogaret *et al.*, we obtain the induced Hall resistance  $R_{12,34}/R_{12,34}^0$  as shown in Fig. 5.6 for case (A) and (B) (dotted and solid curves, respectively) which is compared with the experimental result (dashed curve).

We notice that the induced Hall resistance for  $B_a = 0$  approaches 0.5 in both cases (A) and (B), and increases rapidly until  $B_a = 0.0325B_0$  in case (A) and  $B_a = 0.0375B_0$  for (B). The experimental peak position of the Hall resistance  $B_a = 0.04B_0$  is very close to these values. For larger  $B_a$  the curve almost coincides with the one in Fig. 5.5, which is due to the exponential form of  $t/T$ .

Notice that for case (B) the peak is very close to the experimental position and the qualitative behaviour of the Hall resistance is reproduced, the experimental curve differs quantitatively with the theoretical one only for  $B_a > 0.04B_0$ . Our Hall resistance in this magnetic field range is smaller than measured experimentally. From this comparison it seems that the cycloidlike electron trajectories do not contribute much for large applied magnetic field  $B_a$ . This might be due to a large concentration of scatterers underneath the magnetic stripe edge, which might arise from the fabrication process of the sample. This would not only result in an increase of the resistance, but would especially hamper/kill the cycloidlike states propagating underneath it.

Due to the fact that the Hall resistance for large  $B_a$  equals the two terminal resistance, it is possible to estimate  $\alpha$  by comparison of the theoretical curve with the experimental one. In order to obtain reasonable agreement with the experimental curve, we have to assume  $\alpha = 1.59$ . This value is now fixed and will be used to compare our theoretical results on the magnetoresistance with the experimental results of Ref. [58].

## 5.5 THE MAGNETORESISTANCE

In order to measure the magnetoresistance, the voltage probes are on the same side of the wire and separated a distance from each other along the 1D wire as shown schematically in Fig 5.2. If the probes are situated on the same side (which is the case for the curves under study), we can approximate the transmission probabilities by:  $T_{31} = T$ ,  $T_{32} = (1 - \beta)t$ ,  $T_{51} = (1 - \beta)T$ ,  $T_{52} = t$ , where  $\beta < 1$  is defined as the fraction of the current  $I_{12}$  which is reflected due to collisions between probe 3 and 4. The magnetoresistance is then given by

$$R_{12,35} = \frac{1}{\alpha} \frac{h}{e^2} \frac{1}{T_{12}} \frac{(2 - \beta)\beta}{\left[\frac{t}{T} + \frac{T}{t}\right] (1 - \beta) + \beta^2 - 2\beta + 2}. \quad (5.12)$$

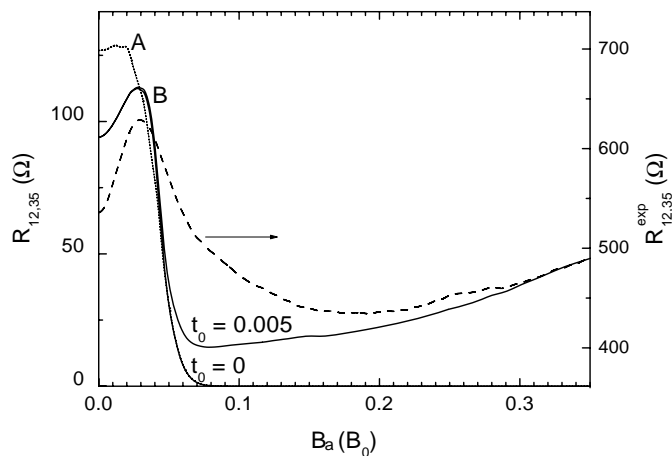


Fig. 5.7 The magnetoresistance  $R_{12,35}$  as function of the applied magnetic field  $B_a$  in case (A) (dotted curve) and (B) (solid curve). The latter is plotted with and without remainder  $t_0$ . The experimental result of Nogaret *et al.* (dashed curve) is plotted with respect to the axis on the right hand side.

Note that in this case there are two parameters  $\alpha$  and  $\beta$  and one function  $t/T$  which determine the magnetoresistance.

In absence of any magnetic field,  $t/T = 1$  and we obtain for the form factor  $F \approx \beta/(2 - \beta)$ . For increasing magnetic field  $B_a$ ,  $t/T$  will decrease rapidly and for  $B_a \gg 0$ ,  $t/T < 1$ , which results in  $F = (t/T)(2\beta)/(1 - \beta)$ .

Theoretically  $\alpha$  and  $t/T$  are identical to those of the previous section and we have only to determine the parameter  $\beta$ . It is clear that also this parameter depends on the distance between the two voltage probes, the scattering time and the velocity of the electron states at the Fermi-level. For simplicity we will consider  $\beta(B_a) \approx \beta$  to be independent of the magnetic field, which is justified since the function  $t/T(B_a)$  changes more drastically than  $\beta(B_a)$ . We will show that this approximation already results in good qualitative agreement with the experimental curves.

If we insert  $\alpha = 1.59$  and  $t/T$  identical to the ones obtained from the Hall resistance, we arrive at the magnetoresistance shown in Fig. 5.7. In this figure we took  $\beta = 0.95$  and plotted  $R_{12,35}$  for case (A) (dotted curve) and case (B) (solid curve) together with the experimental result of Nogaret *et al.* (dashed curve), which is plotted with respect to the right hand axis. We find a peak in the resistance at  $B_a = 0.02B_0$  in case (A), and  $B_a = 0.0275B_0$  for (B). The experimental peak position ( $B_a = 0.03B_0$ ) (dotted curve) is very close to our theoretical result for case (B). Notice that the peak position occurs for smaller  $B_a$  then for the induced Hall resistance, which is in correspondence with the experimental results.

In contrast to the experimental results, we notice that for large  $B_a$ -values the magnetoresistance is zero. This is due to the fact that we have assumed that for large  $B_a$ -values,  $t/T = 0$ . But due to scattering there is always a possibility for an electron to be scattered from an edge state localized on one side of the sample to an edge state on the other side (and traveling in the other direction). If we assume that this effect results in a constant remainder  $t_0 = 0.005$  and corresponding  $t/T = (1 - t_0) \exp[-25B_a - (35B_a)^2] + t_0$ , we obtain the positive magnetoresistance as measured experimentally. This background does not change the Hall resistance qualitatively: the slope decreases, but this can easily be compensated with a larger  $\alpha$  in order to have good agreement with the experiment.

It is very hard to reproduce the experimental results quantitatively, as is obvious from the need for a different left and right axis. The magnitude of the experimental result is larger, and an additional background is present. Due to the approximations made in our simple approach, we underestimated the magnetoresistance. Moreover, the experiment also suffers from other effects, like backscattering etc., which also influence the resistance but which we did not take into account in this paper. Nevertheless, we were able to reproduce the position and the magnitude ( $\approx 150 \Omega$ ) of the peak.

## 5.6 CONCLUSIONS

In this paper we studied electron transport in a quantum wire subjected to an abrupt magnetic field gradient arising from a ferromagnetic stripe fabricated at its surface, as was investigated experimentally by Nogaret *et al.*[58] We were able to reproduce the main qualitative features of the magnetic field dependence of the Hall and magnetoresistance. In particular, the position of the peak in both resistances was correctly explained. This peak is due to two competing effects, i.e. the increase of the separation between subbands for increasing magnetic field, which decreases the number of conducting channels, and the killing of snake orbits and the creation of states which travel in the opposite direction of ordinary snake orbits, the so called cycloidlike states.[77] Two models for the magnetization of the ferromagnetic stripe were considered corresponding to the extreme cases of a hard (A) and a soft (B) magnet. Model (B) gives the closest agreement with experiment which agrees with the observation by Nogaret *et al.* that almost no hysteresis was observed.

In comparison with the theoretical approach of Nogaret *et al.*,[58] ours differs essentially in two ways: (1) the magnetic field profile is the one created by a soft magnet while Nogaret *et al.* assumed a magnetic barrier which is already present for zero applied magnetic field, and (2) we calculated the Hall and magnetoresistance for a four probe measurement with particular geometry, by use of a semi-classical theory based on the Landauer-Büttiker formula, while Nogaret *et al.*[58] made use of a semi-classical drift diffusion model.



# 6

---

## *Hybrid ferromagnet/ semiconductor Hall effect device*

*The diffusive classical transport of a two-dimensional electron gas (2DEG) in a Hall cross, subjected to a locally inhomogeneous magnetic field resulting from an in plane magnetized ferromagnetic film deposited above the 2DEG, is investigated. The magnetic field profile in the 2DEG is obtained analytically and the Hall resistance is calculated for various configurations. Our results are in good agreement with the recent experimental results of Johnson et al [Appl. Phys. Lett. **71**, 974 (1997)] on a novel magneto-electronic device. The output of the device scales inversely with both the size of the voltage and the current probes.*

---

The results presented in this chapter were published as:

- J. Reijniers en F. M. Peeters, Appl. Phys. Lett. **73**, 357 (1998).

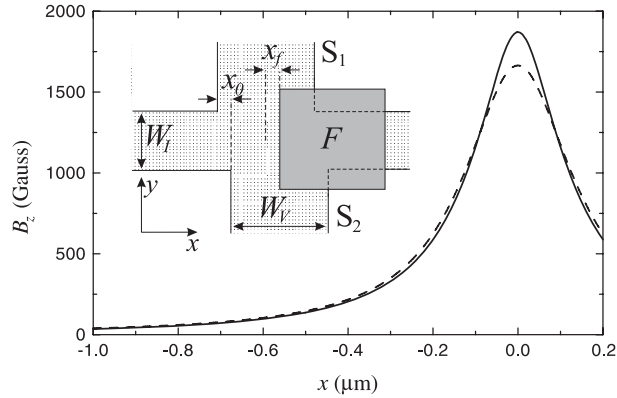


Fig. 6.1 Comparison between the analytically calculated magnetic field profile  $B_z$  in the 2DEG along the center of the current probe (solid curve) and the one based on the line charge model (dashed curve). In the inset the top view of the configuration is shown.

## 6.1 INTRODUCTION

Recently,[64, 73] there has been a growing interest in the effects of magnetic field inhomogeneities in the micrometer and sub-micrometer range, on the transport properties of a two-dimensional electron gas (2DEG). These problems are not only of fundamental interest, but give also rise to several new magneto-electronic device concepts based on these effects. A recent example is the system studied by Monzon *et al.*[54] and Johnson *et al.*[38], who fabricated a new hybrid Hall device, in which a micro-structured ferromagnetic film was incorporated on top of a micron scale Hall cross. This system has potential applications as a magnetic field sensor, a non-volatile storage cell or as a logic gate. Their experimental measurements showed that this new device has excellent scaling properties and output characteristics. In this paper we give a theoretical explanation of the room temperature experimental results of Johnson *et al.*[38] on a novel magneto-electronic device.

## 6.2 SETUP OF THE DEVICE

The top view of the device configuration is shown in the inset of Fig. 6.1. For convenience, we used the same labeling as in Ref. [38]. A thin metal ferromagnetic film  $F$  with thickness  $d_f = 0.15 \mu\text{m}$  was deposited a distance  $h = 0.076 \mu\text{m}$  above a Hall cross, which was fabricated from a high mobility InAs film containing a 2DEG.  $F$  and the 2DEG are electrically isolated from each other. The ferromagnetic film had an in plane magnetization in the  $x$ -direction (taken along the current direction), which will result in an inhomogeneous  $B_z$  profile in the 2DEG. When a voltage is applied to the 2DEG

along the  $x$ -direction, a current will flow, and this will generate a measurable Hall-voltage  $V_H$  over the voltage probes  $S_1$  and  $S_2$ . An external applied magnetic field in the  $x$ -direction sweeps the magnetization, resulting in changes in  $V_H$ . The current probes and the voltage probes of the Hall cross have respectively width  $W_I$ ,  $W_V$ , which are in the micrometer region.  $S_1$  and  $S_2$  may be shifted a distance  $x_0$  from each other, for reasons described below.  $F$  is square shaped with typical width  $W_I + 2 \mu\text{m}$  and is located with one edge at a distance  $x_f$  from the center of the Hall cross. The configuration is symmetric in the  $y$ -direction.

### 6.3 OUR THEORETICAL APPROACH

The experiments of Ref. [38] are done at room temperature and therefore we can rely on the classical diffusion model of Ref. [34] to describe the electrical transport in the present device. This is justified since  $\mu B_{z,max} = 0.37 < 1$ . The theoretical background is fully identical to the one presented in Ref. [34] and starts from the continuity equation which is a 2D partial differential equation

$$\nabla \cdot [\sigma(x, y) \nabla \phi(x, y)] = 0, \quad (6.1)$$

where  $\phi(x, y)$  is the electrical potential and  $\sigma(x, y)$  is the spatial dependent conductivity tensor

$$\begin{aligned} \sigma(x, y) &= \begin{bmatrix} \sigma_{xx} & \sigma_{xy}(x, y) \\ \sigma_{yx}(x, y) & \sigma_{yy} \end{bmatrix} \\ &= \frac{\sigma_0}{1 + [\mu B_z(x, y)]^2} \begin{bmatrix} 1 & \mu B_z(x, y) \\ -\mu B_z(x, y) & 1 \end{bmatrix} \end{aligned} \quad (6.2)$$

where  $\sigma_0 = n_s e \mu$  is the zero magnetic field Drude conductivity,  $n_s$  is the electron density and  $\mu$  is the electron mobility. The 2D partial differential equation is cast into a finite-difference form and is solved numerically using the same matrix recursion scheme as described in Ref. [35]. In the following, we restrict the calculations to a  $(3W_V, 3W_I)$  region centered around  $(0, 0)$ , with the boundary conditions[35]  $\phi(-3W_V/2, y) = 0$  and  $\phi(3W_V/2, y) = 1$ , and the condition that no current can flow out of the sides of the sample, i.e.  $j_y(x, -3W_I/2) = j_y(x, 3W_I/2) = 0$ . We checked that our results are not altered by increasing the length of the voltage leads. The Hall resistance is given by  $R_H = V_H/I$ , where  $V_H = \phi(x, -3W_I/2) - \phi(x, 3W_I/2)$ , and  $I = \int j_x(x, y) dy$  is the total current flowing in the  $x$ -direction. In our numerical analysis we used  $\sigma_0 = 173.37 \Omega$ , which corresponds to the mobility  $\mu = 20\,000 \text{ cm}^2/\text{Vs}$  and the electron density  $n_s = 1.8 \times 10^{12} \text{ cm}^{-2}$  of the experimental system of Ref. [38].

First we calculate the magnetic field profile in the 2DEG, resulting from the magnetization of the ferromagnetic film

$$\vec{M}(x, y, z) = \theta_a(x)(1 - \theta_b(x))\theta_c(y)(1 - \theta_d(y))$$

$$\theta_e(z)(1 - \theta_f(z))(m_x \vec{e}_x + m_y \vec{e}_y + m_z \vec{e}_z), \quad (6.3)$$

where  $\theta_a(x) = \theta(a - x)$  is the Heavy-side step function and  $a = x_f$ ,  $b = x_f + W_I + 2$ ,  $c = -(W_I + 2)/2$ ,  $d = (W_I + 2)/2$ ,  $e = h$  and  $f = h + d_f$ , with the convention that  $z = 0$  is taken in the 2DEG plane. Following Ref. [37], the magnetic scalar potential is given by

$$\phi_m(\vec{r}) = - \int \frac{\vec{\nabla} \cdot \vec{M}(\vec{r}')}{|\vec{r} - \vec{r}'|} d\vec{r}', \quad (6.4)$$

from which we obtain the magnetic field  $\vec{B}(\vec{r}) = \vec{H}(\vec{r}) + 4\pi\vec{M}(\vec{r})$  outside the magnetic film, where  $\vec{H}(\vec{r}) = -\vec{\nabla}\phi_m(\vec{r})$ . For magnetization in the  $x$ -direction,  $m_y = m_z = 0$ , and it is possible to perform the differentiation and the integration over  $x'$ . The problem then reduces to solving  $B_z(\vec{r}) = -\partial\phi_m(\vec{r})/\partial z$ . Performing this differentiation and then the integration over  $y'$  and  $z'$ , we arrive at the following exact solution for the  $z$ -component of the magnetic field

$$B_z(x, y, z) = m_x \left[ \begin{aligned} & -(f_{adf}(x, y, z) - f_{acf}(x, y, z)) \\ & +(f_{ade}(x, y, z) - f_{ace}(x, y, z)) \\ & +(f_{bdf}(x, y, z) - f_{bcf}(x, y, z)) \\ & -(f_{bde}(x, y, z) - f_{bce}(x, y, z)) \end{aligned} \right] \quad (6.5)$$

with  $f_{\alpha\beta\gamma}(x, y, z) = \text{arcsinh} \left[ (\beta - y) / \sqrt{(x - \alpha)^2 + (z - \gamma)^2} \right]$ .

## 6.4 RESULTS AND DISCUSSION

In Fig. 6.1, the  $B_z$ -profile is plotted along the center of the current probe for  $x_f = 0$  in the case of saturation of the magnetization, which for the Permalloy material used in Ref. [38] yielded  $m_x = 860 \pm 20$  emu/cm<sup>3</sup> at room temperature. This result is compared to the *line charge model* (dashed curve in Fig.6.1) used in Ref. [38] which gives  $B_z(x) = 2\lambda_m R / ((x - a)^2 + R^2)$ , where  $\lambda_m = m_x d_f$  is the magnetic charge density and  $R = h + d_f/2$  is the distance between the approximated line of magnetic poles and the 2DEG. Note that the line charge model results in a 12 % smaller value for the maximum field  $B_{z,max}$  but a slightly larger  $B_z$  in the tail region.

Inserting the magnetic field profile (6.5) into (6.2), we solved the partial differential equation (6.1) numerically. We only consider the case when the magnetization is saturated. In Fig. 6.2, the change in the Hall resistance resulting from a flip of the fully saturated magnetic film,  $2\Delta R_H$ , is plotted as a function of  $x_f$  for  $(W_V, W_I) = (2 \mu\text{m}, 3 \mu\text{m})$  in the case of the symmetric Hall bar configuration. Our results (solid curve) overestimate the experimental results (dots) by about 15 %. Nevertheless this result is in much better agreement than those obtained based on the approximation that the Hall resistance is

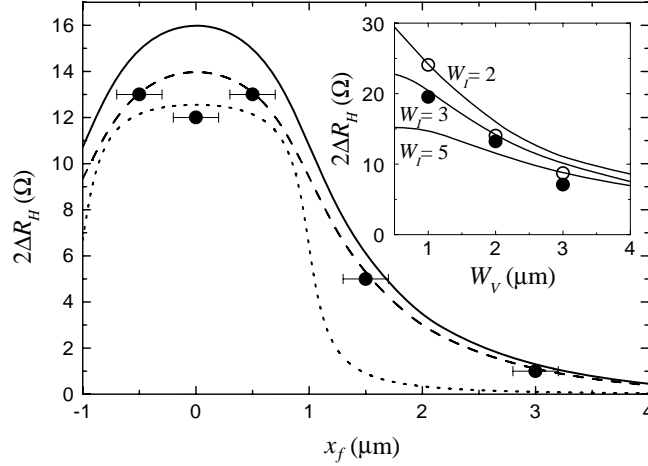
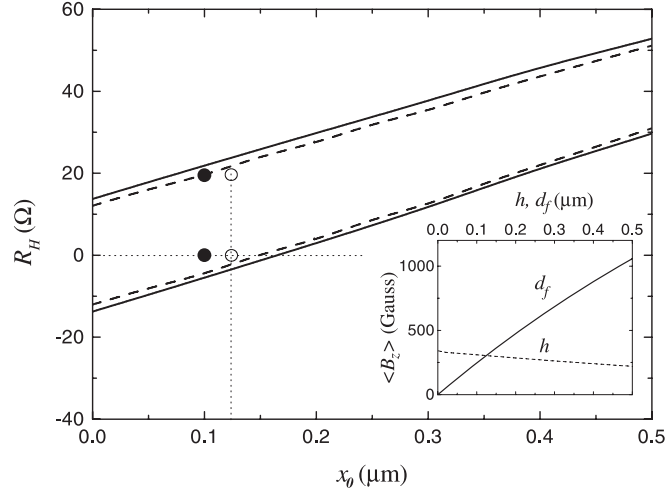


Fig. 6.2 The maximum change in the Hall resistance  $2\Delta R_H$  as a function of  $x_f$  for the  $(W_V, W_I) = (2 \mu\text{m}, 3 \mu\text{m})$  configuration. The symbols are the experimental results, the solid curve is our result using the parameters given by Johnson *et al.* The dashed curve is obtained for a marginally thinner magnetic film with  $d_f = 0.13 \mu\text{m}$  and the dotted curve is calculated based on the simple formula  $2\Delta R_H = 2 \langle B_z \rangle / n_s e$  where the results are reduced by a factor 2. The inset shows  $2\Delta R_H$  for various  $W_I$  as a function of  $W_V$  (solid curves). The experimental values (solid dots) are compared with the calculated values (hollow dots).

given by the average magnetic field in the cross region  $2\Delta R_H = 2 \langle B_z \rangle / n_s e$  (dotted curve which is scaled down by a factor 2). Note that the latter approach only works well in the ballistic regime (i.e. very low temperatures), as was demonstrated in Refs. [35] and [66]. Possible reasons for the discrepancy between experiment and the solid curve are: 1) it is possible that the magnetization of the film is not yet totally saturated, i.e.  $m_x < 860 \text{ emu/cm}^2$ ; 2) the effective distance  $h$  between the magnetic film and the 2DEG, or 3) the thickness  $d_f$  of the magnetic film can be different from those given in Ref. [38]. In order to find agreement we have to increase  $h = 0.076 \mu\text{m}$  up to  $0.25 \mu\text{m}$ , which is unrealistic large. Decreasing the thickness of the magnetic film from  $d_f = 0.15 \mu\text{m}$  to  $d_f = 0.13 \mu\text{m}$  leads to (see dashed curve in Fig. 6.2) excellent agreement with experiment. So it is rather  $d_f$  than  $h$  that dominates the magnetic flux through the Hall center which results in a Hall resistance. This can also be readily seen in the inset of Fig. 6.3, where  $\langle B_z \rangle$  is plotted as a function of  $d_f$  (solid curve) and of  $h$  (dashed curve). The theoretical curve in Fig. 6.2 for  $2\Delta R_H$  attains its maximum value at  $x_f = 0$  which is also found in the low temperature measurements of Ref. [54]. The room temperature measurement of Ref. [38] gave a smaller  $2\Delta R_H$  at  $x_f = 0$  and they found a maximum Hall voltage for  $x_f \approx 0.5 \mu\text{m}$ . This result cannot be explained within the present calculation.



*Fig. 6.3* The Hall resistance  $R_H$  at saturated magnetization as a function of the shift  $x_0$  between the voltage probes  $S_1$  and  $S_2$  for the  $(W_V, W_I) = (1 \mu\text{m}, 2 \mu\text{m})$  configuration. The upper and lower solid curve are respectively with sweep up and sweep down magnetization when  $d_f = 0.15 \mu\text{m}$ . The dashed curves are those for  $d_f = 0.13 \mu\text{m}$ . The experimental data for  $x_0 = 0.1 \mu\text{m}$  are shown by the solid dots. The hollow dots are the same experimental values, assuming  $x_0 \approx 0.125 \mu\text{m}$ . The inset gives the average magnetic field  $\langle B_z \rangle$  in the Hall bar cross region for the  $(2 \mu\text{m}, 3 \mu\text{m})$  configuration as a function of  $d_f$  with  $h = 0.076 \mu\text{m}$  (solid curve) and as a function of  $h$  for  $d_f = 0.13 \mu\text{m}$  (dashed curve).

From Fig. 6.1 we notice that the magnetic field  $B_z$  is essentially non zero in the region  $-0.5 \mu\text{m} < x < 0.5 \mu\text{m}$  and therefore by decreasing the size of the Hall cross, one can increase the average field in the Hall cross and consequently  $2\Delta R_H$ . This is illustrated in the inset of Fig. 6.2 where we show the dependence of  $2\Delta R_H$  on the width of the voltage probes ( $W_V$ ) for three different values of the width of the current probes ( $W_I$ ) for  $d_f = 0.13 \mu\text{m}$ . Note that according to the simple formula  $2\Delta R_H = 2 \langle B_z \rangle / n_s e$  one would expect  $2\Delta R_H$  to be independent of  $W_I$  as long as the ferromagnetic film is wider than the current probes. But in our numerical analysis we find that  $2\Delta R_H$  decreases with increasing  $W_I$ . The experiments (solid dots) were done with samples with different width of current probes and the hollow dots are the corresponding theoretical results. For  $W_V = 1 \mu\text{m}$  we obtain a theoretical value (see also Fig. 6.3) which is 24% larger than found experimentally. This may be a consequence of the fact that the three samples do not have the same ferromagnetic film thickness  $d_f$ . In conclusion, we confirm the inverse scaling for the voltage probes as found in Ref. [38] and add the inverse scaling of the current probes to it.

When the Hall cross is fabricated symmetrically, the hybrid Hall device is characterized by a bipolar output  $\pm \Delta R_H$  as the magnetization is swept from

positive to negative. Introducing a small asymmetry, a shift  $x_0$  of voltage probe  $S_1$  with respect to  $S_2$ , results in a small offset resistance  $R_0$ . This makes it possible to shift the output values, and to obtain output characteristics varying for example between 0 and  $2\Delta R_H$ . In Ref. [38] this situation was investigated in a  $(W_I, W_V)=(1\ \mu\text{m}, 2\ \mu\text{m})$  configuration by shifting the voltage probes by  $x_0 = 0.1\ \mu\text{m}$ . The output characteristics for both negative and positive saturated magnetization are plotted in Fig. 6.3 as a function of  $x_0$  with  $d_f = 0.15\ \mu\text{m}$  (solid curves). When  $x_0 = 0.1\ \mu\text{m}$  we obtain output characteristics  $(-5.5\ \Omega, 21.8\ \Omega)$  which are in reasonable agreement with the experimental values  $(0.5\ \Omega, 19.5\ \Omega)$  (solid dots) obtained by Johnson *et al.* As mentioned above, the discrepancy in  $2\Delta R_H$  is probably due to a different  $d_f$ . This is illustrated by plotting the same curves (dashed curves in Fig. 6.3) considering  $d_f = 0.13\ \mu\text{m}$ , which is, as earlier calculated (see inset of Fig. 6.2), still too large. On the other hand, we can center our numerical results by considering a slightly bigger shift of the voltage probes than given in Ref. [38], i.e.  $x_0 \approx 0.125\ \mu\text{m}$  (hollow dots). This brings the experimental results in close agreement with our theoretical results (dashed curves).

## 6.5 CONCLUSIONS

In this letter we provided a theoretical analysis of the experimental results of Johnson *et al.*[38] on a new magneto-electronic device. We found that the magnetic film may be slightly thinner than measured experimentally. The Hall resistance scales inversely with the size of *both* the voltage and the current probes.



*γ*

---

## *Diffusive transport and optimization of the hybrid Hall effect device*

*We study the temperature dependent Hall resistance  $R_H$  of a new magneto-electronic device consisting of a micron scale Hall cross which is subjected to the fringe field of a ferromagnetic film with in-plane magnetization, placed on top of it. External application of a weak in plane magnetic field yields reversing of the magnetization and consequently modulates  $R_H$ . Starting from the continuity equation, we calculate numerically the steady state electrical potential and current distributions in the Hall device and show that the temperature dependency can be well understood in the diffusive regime. We make a detailed investigation of the influence of different parameters on the output of this device.*

---

The results presented in this chapter were published as:

- J. Reijnders and F. M. Peeters, J. Appl. Phys. **87**, 8088 (2000).

## 7.1 INTRODUCTION

The last three decades have witnessed the rapid advance of solid-state electronics, including first the replacement of discrete circuits elements, and finally the integration of many circuit elements onto one semiconductor chip. The only fundamental discrete elements that have been left behind are those involving magnetic materials. The incorporation of those materials would allow the electronic flexibility of semiconductor-based quantum structures to be combined with local magnetism, enabling the development of new magneto-electronic devices.[65] Almost a school example of such a device was proposed by Johnson *et al.*[38] and Monzon *et al.*[54], who fabricated a device of which the essential physics does not rely on spin-dependent effects (as GMR), but on a phenomenon which was discovered more than hundred years ago by Edwin Hall.[27] Nevertheless, this device has drawn a lot of interest as a possible candidate for a new non-volatile memory element, and efforts are made to commercialize this system.[93, 16]

Hall probes become increasingly popular as local magnetometers for superconducting and ferromagnetic materials, because of their large magnetic field sensitivity and their tolerance to broad ranges of temperatures and magnetic fields. Including magnetic materials on top of a Hall cross, allows one to study their magnetization where standard magnetometry fails, because the amount of magnetic material is too small.[17, 47] By examining the effect of the fringe fields resulting from the magnetic material on the transport properties of the two-dimensional electron gas (2DEG), one can obtain information about its magnetization. This is exactly the basic for the operation of the hybrid Hall effect device, where it is not the goal to study the magnetic material, but solely to obtain the magnetic state of the magnetic film. Electrically (or magnetically) one can manipulate the magnetization of the film, which results in a measurable Hall resistance, and thus can be used as a non-volatile memory element (or a magnetic field sensor).

The side and the top view of the device are shown in Figs. 7.1(a) and (b), respectively. A thin metal ferromagnetic film  $F$  with thickness  $d_f$  is grown a distance  $h$  above a Hall cross, which was fabricated from a high mobility heterojunction which contains a 2DEG.  $F$  and the 2DEG are electrically isolated from each other. The ferromagnetic film has in-plane magnetization in the  $x$ -direction (taken along the current direction), which results in an inhomogeneous  $B$ -profile in the 2DEG due to the fringe fields. When a voltage is applied to the 2DEG along the  $x$ -direction, a current will flow, and this will generate a measurable Hall voltage  $V_H$  over the voltage probes  $S_1$  and  $S_2$ . An external applied magnetic field in the  $x$ -direction sweeps the magnetization, resulting in changes in  $V_H$ . The current probes and the voltage probes of the Hall cross have respectively width  $W_I$  and  $W_V$ , which are in the micrometer region.  $S_1$  and  $S_2$  may be shifted a distance  $x_0$  from each other.  $F$  is square shaped with typical dimensions  $F = W_I + 2\mu m$  and is located with

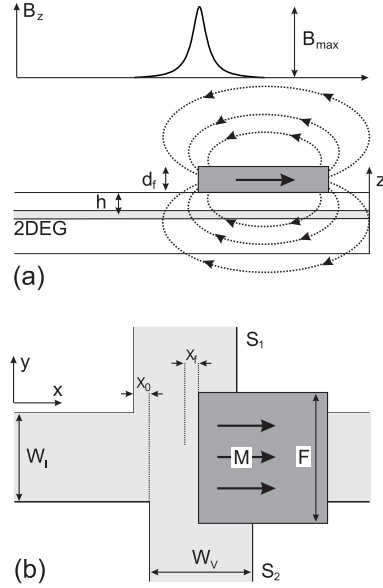


*Fig. 7.1* Schematic diagram of : (a) the side view and (b) the top view of the hybrid Hall effect device.

one edge at a distance  $x_f$  from the center of the Hall cross. The configuration is symmetric in the  $y$ -direction.

Johnson *et al.*[38] fabricated such a device, where the 2DEG was created by means of a InAs film. They performed experiments at room temperature on different device geometries, varying the width of both voltage ( $W_V$ ) and current probes ( $W_I$ ), the position of the film ( $x_f$ ), and the shift between the voltage probes ( $x_0$ ). They found inverse scaling with the width of the voltage probes, i.e. increasing Hall resistance with decreasing size of the Hall probes, and found that the bipolar output can be shifted by introducing an asymmetry in the geometry, i.e. by shifting the voltage probes with respect to each other. In Refs. [75] and [76] we explained their experimental results using a classical theory valid in the diffusive regime. We reproduced both quantitatively and qualitatively their experimental results and calculated the Hall resistance which scaled inversely not only with the voltage probes but also with the size of the current probes.

Monzon *et al.*[54] performed temperature dependent experiments on a similar device, now grown on top of a high mobility  $n$ -type GaAs 2DEG. Their experiment allows us to study the transition of the electron transport from the ballistic to the diffusive regime. In Sect. II, we extend our previous study to the system of Monzon *et al.*[54] and we investigate the temperature dependence of this novel magnetoelectronic device. In Sect. III we elaborate on the Hybrid Hall effect device at room temperature. We discuss the potential profile and the corresponding current distribution in the cross. In Sect. IV we

make a detailed investigation of the influence of different parameters as the thickness of the magnetic film ( $d_f$ ), the distance from the magnetic film to the 2DEG ( $h$ ), the geometry and size of the Hall cross ( $W_I$  and  $W_V$ ), and the shift from the edge of the film with respect to the center of the cross ( $x_f$ ) on the output of the device, i.e. the Hall resistance. Our conclusions are presented in Sect. V.

## 7.2 TEMPERATURE DEPENDENCE OF THE HALL RESISTANCE

The device of Monzon *et al.*[54] has the following dimensions:  $d_f = 0.150\mu\text{m}$ ,  $h = 0.077\mu\text{m}$ ,  $W_I = 5\mu\text{m}$ ,  $W_V = 3\mu\text{m}$  and  $F = 7\mu\text{m}$ . A permalloy film layer was grown on top of a high mobility  $n$ -type GaAs 2DEG, of which the mobility  $\mu$  and the electron density  $n_e$  were measured using independent Hall bar measurements (see Fig. 4 in Ref. [54]). At low temperature (i.e.  $T \approx 4.2$  K) the mobility was  $\mu = 1.0 \times 10^6 \text{cm}^2/\text{Vs}$ , with an electron density  $n_e = 1.52 \times 10^{11} \text{cm}^{-2}$ . The corresponding numbers at room temperature are  $\mu = 8351 \text{cm}^2/\text{Vs}$  and  $n_e = 2.31 \times 10^{11} \text{cm}^{-2}$ . They measured the Hall resistance for different devices as function of temperature (see the inset of Fig. 3 in Ref. [54]). These devices were fabricated from the same GaAs wafer, i.e. containing the same 2DEG, and only distinguish in the position of the magnetic film with respect to the center of the Hall cross, i.e. different  $x_f$ . Depending on the temperature and the applied magnetic field, transport through high mobility heterostructures can roughly be separated in two regimes: the ballistic and the diffusive regime.

### 7.2.1 Diffusive regime

At high temperatures, scattering dominates electron transport in the Hall cross. To study this regime we rely on a classical model earlier presented in Refs. [34] and [35], where we solved the 2D elliptic partial differential equation for the electrical potential  $\phi(x, y)$

$$\nabla \cdot [\sigma(x, y) \nabla \phi(x, y)] = 0, \quad (7.1)$$

where  $\sigma(x, y)$  is a spatial dependent conductivity tensor due to the presence of the finite magnetic barrier,

$$\sigma(x, y) = \begin{bmatrix} \sigma_{xx}(x, y) & \sigma_{xy}(x, y) \\ \sigma_{yx}(x, y) & \sigma_{yy}(x, y) \end{bmatrix}, \quad (7.2)$$

with  $\sigma_{xx} = \sigma_{yy} = \sigma_0 / \{1 + [\mu B(x, y)]^2\}$  and  $\sigma_{xy} = -\sigma_{yx} = \mu B(x, y) \sigma_{xx}$ , where  $\sigma_0 = n_e e \mu$  is the Drude conductivity. The magnetic field profile  $B(x, y)$  is given by Eq. (5) of Ref. [75]. The temperature dependence enters the conductivity tensor through the mobility  $\mu$ , and the electron density  $n_e$ , which was measured experimentally. This 2D partial differential equation is cast into a finite difference form and solved numerically using the

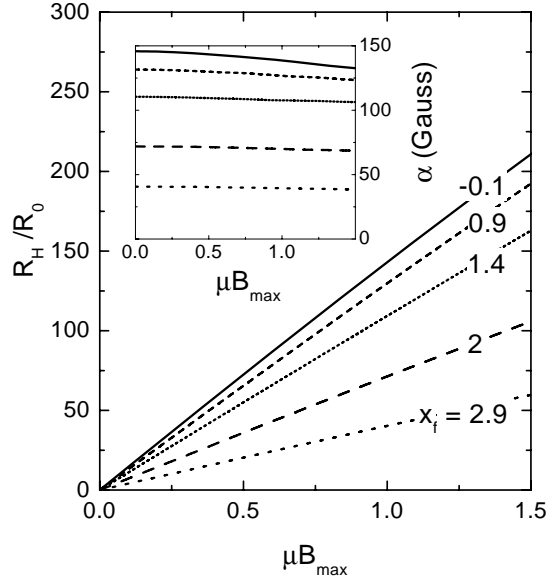


Fig. 7.2 The Hall resistance  $R_H$  as function of  $\mu B_{\max}$  for different magnetic field profiles, determined by the shift  $x_f$  of the peak from the center of the cross. The inset shows the corresponding Hall factor.

same matrix recursion scheme as in Ref. [35]. We restrict the calculations to a  $(3W_V, 3W_I)$  region centered around  $(0, 0)$ , the center of the Hall bar, with boundary conditions defined by the device geometry which is shown in Fig. 7.1(b). A voltage  $V$  is applied over the current probes  $\phi(-3W_V/2, y) = 0$  and  $\phi(3W_I/2, y) = V$ , and no current can flow out the sides of the sample and out the Hall probes  $j_y(x, -3W_I/2) = j_y(x, 3W_I/2) = 0$ . The Hall resistance is given by  $R_H = V_H/I$ , where  $V_H = \phi(0, 3W_I/2) - \phi(0, -3W_I/2)$ , and  $I = \int_c^d j_x(x, y) dy$ , where  $c$  and  $d$  are any two points on opposite sides of the sample at one of the current probes.

In Fig. 7.2 we plot the Hall resistance in units of  $R_0 = 1/\sigma_0$  as function of  $\mu B_{\max}$ , where  $B_{\max}$  is the peak value of the magnetic field profile. We used  $B_{\max}$  as a parameter instead of  $\langle B \rangle$ , because we believe it is more relevant to determine the distinction between the diffusive and the ballistic regime.

For the same functional form of the magnetic field profile, the resistance  $R_H/R_0$  depends only on  $\mu B_{\max}$  for a given geometry. The temperature dependence is therefore only contained in the scaling factors  $R_0$  and  $\mu$ . Thus, the dependence of  $R_H$  on the magnetization of the film (i.e.  $B_{\max}$ ) and on the temperature (as long as we are in the diffusive regime) is contained in the same plot. As was already found in Ref. [35], we notice that the Hall

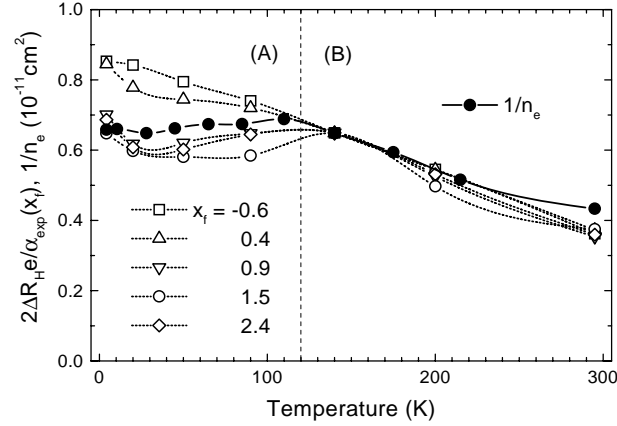


Fig. 7.3 Scaling of the experimental results of Monzon *et al.* [54] for the Hall resistance at saturated magnetization of the ferromagnetic film as function of the temperature, for devices with different position of the edge of the film with respect to the center of the Hall cross. The solid dots show  $1/n_e$ , the inverse of the experimentally measured electron density.

resistance  $R_H$  is a linear function of  $\mu B_{max}$ , as long as  $\mu B_{max} < 1$

$$R_H/R_0 = \alpha' \mu B_{max} = \alpha \mu.$$

Thus, in the diffusive regime, we can associate with every normalized magnetic profile ( $B_{max} = 1$ ) a constant factor  $\alpha'$ , or associate with every magnetic field profile a Hall factor  $\alpha$ . This results in the following equation

$$R_H = \frac{\alpha}{n_e e}, \quad (7.3)$$

which is similar to the one in the ballistic regime, where it was found that [66]  $\alpha = \langle B \rangle$ , with  $\langle B \rangle$  the average magnetic field in the cross. For the diffusive regime, the  $\alpha$  values are shown in the inset of Fig. 7.2.

The validity of this relation is demonstrated in Fig. 7.3, where the inverse electron density  $1/n_e$  (solid dots) is plotted together with the scaled Hall resistance  $2\Delta R_H e / \alpha_{exp}(x_f)$  at saturation magnetization as measured by Monzon *et al.* [54].  $\Delta R_H$  is the Hall resistance at saturation magnetization and  $2\Delta R_H$  is the change in the Hall resistance when reversing the magnetic field direction at saturation. Every curve corresponds to the output of a device with a different  $x_f$ , i.e. position of the magnetic film edge with respect to the center of the Hall cross, and is scaled with a scaling factor  $\alpha_{exp}(x_f)$  such that they all have the same value as the inverse electron density  $1/n_e$  at 140 K. As mentioned earlier, we can essentially divide the temperature range into two regimes, rudely separated by  $T = T(\mu = 1/B_{max}) = \pm 120$  K: the ballistic (A)

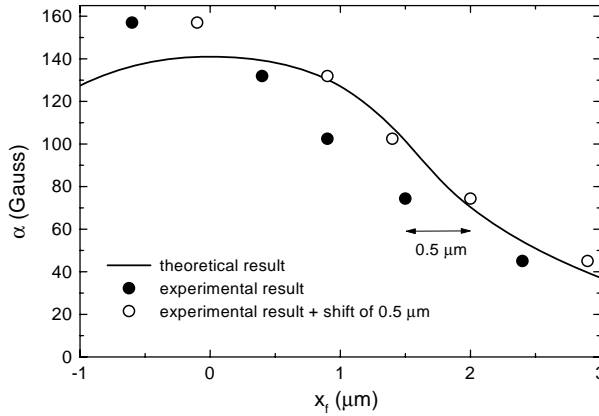


Fig. 7.4 Comparison between the calculated Hall factors  $\alpha(x_f)$  (solid curve) with the experimental scaling factors  $\alpha_{\text{exp}}(x_f)$  (solid dots). The open dots are the experimental results assuming a shift of  $0.5 \mu\text{m}$ .

and the diffusive (B) regime. We notice that all curves overlap rather good in the diffusive region, and for increasing temperature the Hall resistance reduces according to  $1/n_e$ , except at room temperature, where the measured density is 15% below the one we infer from the scaled Hall resistance. A possible reason for this mismatch might be the presence of the conducting ferromagnetic film on top of the 2DEG which acts as a gate and will almost certainly modify the carrier density  $n_e$ .

In order to compensate for this difference we should insert  $n_e = 2.66 \times 10^{11} \text{cm}^{-2}$  instead of  $2.31 \times 10^{11} \text{cm}^{-2}$  in (7.3), which is a difference of about 15%. For decreasing temperature  $\mu B_{\text{max}}$  exceeds 1 at 120K for all curves, and hence the linear behaviour of  $R_H$  with respect to  $\mu B_{\text{max}}$  is no longer rigorously valid. Nevertheless, we notice that there is still a rather good agreement with the  $1/n_e$ -curve for  $x_f \geq 0.9 \mu\text{m}$ . This is due to the fact that the magnetic peak value,  $B_{\text{max}}$ , is positioned further away from the center of the Hall cross, and thus its influence will be smaller. It is remarkable that at the lowest measured temperature all the results for  $x_f \geq 0.9 \mu\text{m}$  agree very well with the diffusion result.

In Fig. 7.4, we compare our numerically calculated Hall factors  $\alpha(x_f)$  (solid curve) with the experimental scaling factors  $\alpha_{\text{exp}}(x_f)$  (solid dots) for the different devices with different shifts  $x_f$ . We obtain a better agreement with experiment if we assume a shift of  $x_f = 0.5 \mu\text{m}$  for the experimental results (open dots). Such a shift was already suggested by Monzon *et al.*, [54] and might be caused by demagnetization effects at the edge of the film. Only for  $x_f = -0.6 + 0.5 \mu\text{m}$  there is a remaining discrepancy between theory and experiment. The reason for this may be due to the fact that every dot cor-

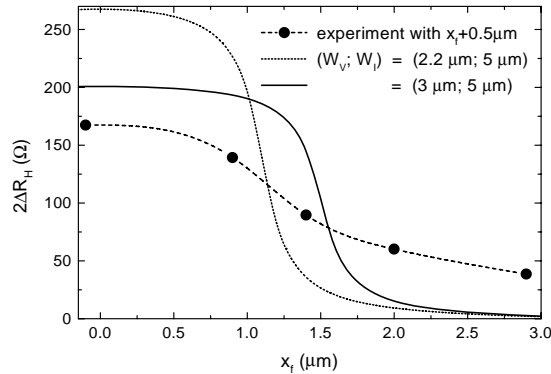


Fig. 7.5 The total resistance change  $2\Delta R_H$  as measured by Monzon *et al.* [54] is shown by the solid dots. The dotted curve is the theoretical curve (in the ballistic regime), assuming  $(W_I, W_V) = (2.2 \mu\text{m}, 5 \mu\text{m})$ . The full curve is the result for  $(W_I, W_V) = (3 \mu\text{m}, 5 \mu\text{m})$ .

responds to a different device with a slightly different geometry, i.e. slightly different width of the probes, thickness of the magnetic film, etc. The output characteristics are very sensitive to these values, as we will show further on.

### 7.2.2 Ballistic regime

Although transport in the ballistic regime is outside the scope of this paper, in the following we limit ourselves to a few remarks. It is well known [66] that in the ballistic regime, i.e. for low temperatures and large mobility, the Hall resistance can be determined using the simple formula

$$\Delta R_H = \frac{\langle B \rangle}{n_e e}, \quad (7.4)$$

as long as  $B$  is not too large. Applying this to the lowest temperature measurement ( $T = 4.2$  K) and again including the shift of  $x_f = 0.5 \mu\text{m}$ , does not yield a qualitative agreement with experiment, as is shown in Fig. 7.5. Nevertheless, we find a slightly better quantitative result (20% discrepancy in the case of  $x_f = 0$ ) with our configuration, than Monzon *et al.* (60%), who estimated the electrical width of the voltage probes to be  $2.2 \mu\text{m}$ , whereas we used the optical width  $W_I = 3 \mu\text{m}$ . Notice that the theoretical  $2\Delta R_H$  decays more rapidly with  $x_f$  than exhibited by experiment. Monzon *et al.* [54] attributed this to the local magnetic field profile which might have a different shape than calculated theoretically. It is as if the average magnetic field reduces too abruptly, when the magnetic film edge exits the cross. In their study, they used the line charge model, in which the fringe field is the one of an infinitesimally thin film with the same total magnetic moment. We used the

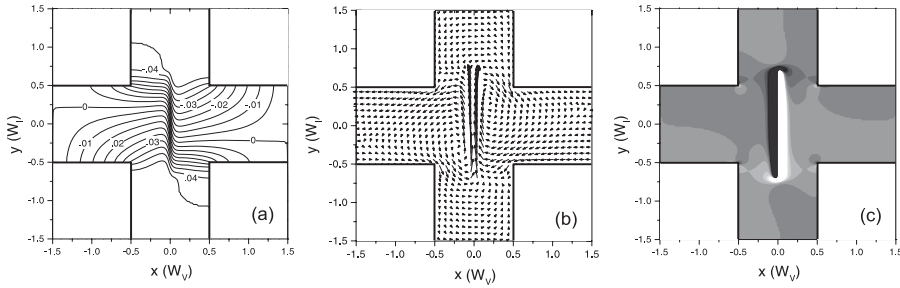


Fig. 7.6 (a) The difference potential profile  $\Delta V/V$ , (b) the difference current profile and (c) the difference induced charge density profile due to the presence of the magnetic film for the Monzon *et al.*[54] configuration with  $x_f = 0$  at temperature 140 K.

exact profile including the effects arising from the finite film thickness, which was calculated in our earlier paper.[75] Clearly this change of shape cannot account for the different behaviour. A smearing out of the magnetic flux, by lowering the theoretical curve and adding the remaining flux as a background field, did also not give a satisfying reproduction of the experimental results. In contrast to Ref. [34], where low temperature transport experiments through magnetic barriers (with dimensions  $(3\mu\text{m}, 40\mu\text{m})$ ) were explained using the same classical diffusive theory, although  $\mu B \gg 1$ , this approach was found not to work here. In order to understand the low temperature behaviour, we believe one should follow a different approach, and for example use the billiard model to calculate the electron trajectories and consequently the electrical properties of the Hall cross. The results will depend on the geometry of the device and both the position and the strength of the magnetic field inhomogeneity.

### 7.3 DETERMINATION OF THE OPTIMAL DESIGN PARAMETERS OF THE DEVICE

Recently, the hybrid Hall effect device has drawn a lot of interest, as being a possible candidate for a non-volatile magnetic memory.[93] Nowadays, efforts are made to realize a commercial *Hall effect hybrid memory*. An advantage of this device is that it is relatively easy to manufacture, and still has good output values at room temperature. In the following we will report on a more general study of this Hall effect device in the diffusive regime, and we will determine the optimal design parameters at room temperature.

Applying a potential  $V$  over the current probes, results in a different potential profile over the Hall cross for the case with and without magnetic film. The most important features are most pronounced at 140 K, where  $\mu = 3.5 \times 10^4 \text{cm}^2/\text{Vs}$  and  $n_e = 1.54 \times 10^{11} \text{cm}^{-2}$ . In order to enhance these features, a contour plot of the *difference potential profile* is shown in Fig. 7.6 (a).

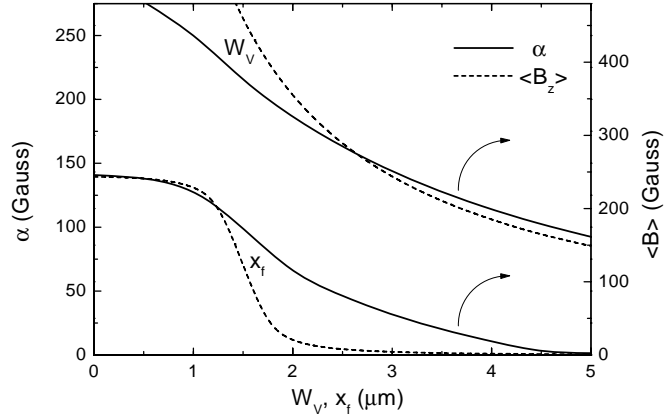


Fig. 7.7 The Hall factor  $\alpha$  at saturated magnetization as function of the shift  $x_f$  and the width of the voltage probe  $W_V$  (solid curves). The dotted curves are the corresponding average magnetic field in the cross region.

This is the difference in potential with and without magnetic film. Notice that a potential difference  $V_H = \phi(x = -3W_I/2) - \phi(x = 3W_I/2)$  (Hall potential) is generated between the two voltage probes, which gives rise to the measured Hall resistance. The magnetic field profile resulting from the magnetic film creates adjacent a small potential dip and barrier in the center of the cross. Its effect on transport can be seen in Fig. 7.6 (b) where the *difference current* is plotted. Notice that due to the inhomogeneous magnetic field profile two large vortex-like current flows are created which are separated by the edge of the film. Electrons are deflected by the profile and circle around near the edge of the magnetic film, creating a vortex/anti-vortex flow pattern. As a result of this, the decrease of the total net current is small, and consequently the longitudinal resistance  $R_{xx} = V_0/I$  does not increase significantly when the magnetic barrier is present (only with 0.55%). The magnetic inhomogeneity induces a charge dipole, which one can see in Fig. 7.6 (c), where the *difference induced charge density*  $\Delta\rho_{ind}$  is plotted (white = positive, black = negative). In this particular case the dipole is extended over a line, under the magnetic film edge and curves around the edge of the magnetic field profile.

We calculate now the optimal design parameters of the device as studied by Monzon *et al.* The full curves in Fig. 7.7 show the Hall factor as function of  $x_f$  and  $W_V$ . To understand this behaviour we also plotted the average magnetic field in the cross, and merged the two graphes together, in such a way that their peak positions at  $x_f = 0$  coincide. This yields a difference of a factor of 1.73.

As function of  $W_V$  we find an increasing Hall factor,  $\alpha$ , with decreasing  $W_V$ , i.e. inverse scaling. For large  $W_V$ -values, i.e.  $W_V > 2\mu\text{m}$ , the behaviour of

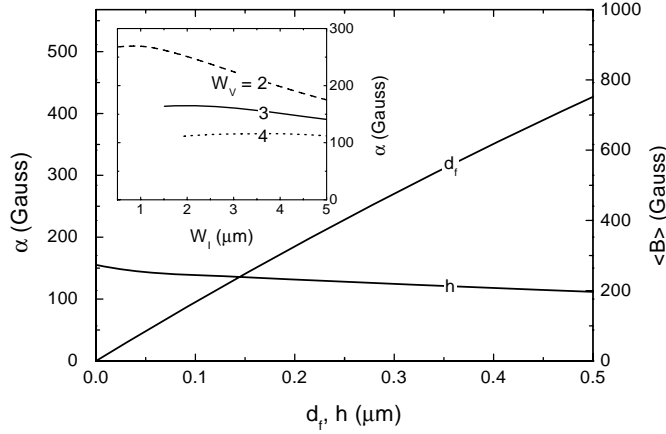


Fig. 7.8 The Hall factor  $\alpha$  at saturated magnetization as function of the thickness of the ferromagnetic film ( $d_f$ ) and the distance between the film and the 2DEG ( $h$ ). Both curves coincide with the average magnetic field  $\langle B \rangle$ , when plotted with respect to the right hand axis. The inset shows  $\alpha$  as function of the width of the current probes ( $W_I$ ) for different widths of the voltage probes ( $W_V$ ).

the Hall factor can be well predicted by  $\langle B \rangle$ . For lower values, i.e.  $W_V < 2\mu\text{m}$ ,  $\alpha$  deviates significantly from what one would expect from the behavior of  $\langle B \rangle$  up to a factor of 1.5 – 2.

The dependence of the output on  $x_f$ , was already discussed in Fig 7.4. We notice that as long as the peak value of the magnetic field profile is in the cross ( $x_f < 1.5\mu\text{m}$ ), the behaviour can be understood through the average magnetic field, but for larger shifts  $x_f$ , the Hall coefficient diminishes more slowly than one would expect from the average magnetic field. This is due to the fact that, in contrast to the ballistic regime, in the diffusive regime the output depends not only on the strength of the magnetic field, but also on the position where the magnetic flux penetrates the 2DEG. With every diffusive Hall cross corresponds a response function, which assigns a weight to the magnetic field strength, depending on its position in the cross.[7]

Consistent with this, when the position of the magnetic field inhomogeneity is fixed, then the behaviour of the Hall factor  $\alpha$  can be well understood through the average magnetic field, as can be seen in Fig. 7.8, where  $\alpha$  is plotted as function of the thickness of the magnetic film ( $d_f$ ), and the distance between the magnetic film and the 2DEG ( $h$ ). When merged as before,  $\alpha$  and  $\langle B \rangle$  overlap and consequently show exactly the same behaviour:  $\alpha$  increases strongly with increasing  $d$ , while the influence of  $h$  is less pronounced.

In the inset of Fig. 7.8, we plot the Hall factor,  $\alpha$ , as function of  $W_I$ , i.e. the width of the current probes. Since the average magnetic field in the cross does not depend on  $W_I$ , one would expect that changing  $W_I$  leaves  $\alpha$

unaltered. One can see that this is not true, since  $\alpha$  increases, when  $W_I$  decreases. This “weak” inverse scaling is present as long as  $W_I > 1.5\mu\text{m}$  and is more pronounced for smaller  $W_V$ . This result is a consequence of the fact that in the diffusive regime the Hall bar probes an area which is larger than only the center part of the Hall cross.

To conclude, in order to obtain the largest voltage output one should decrease  $W_V$ ,  $W_I$ , and  $h$ , and increase  $d_f$ . The optimal values for the device of Monzon *et al.* are  $W_V \sim 0.5 - 1\mu\text{m}$ ,  $W_I \sim 1\mu\text{m}$ ,  $h = 0.5\mu\text{m}$  and  $d_f$  sufficiently large. Decreasing  $W_V$ ,  $W_I$ , and  $h$  below the quoted values will not substantially improve the output of the device.

## 7.4 CONCLUSIONS

In conclusion, we have studied diffusive transport in the hybrid Hall effect device. The temperature dependence of the device was investigated and good agreement with the experimental results of Monzon *et al.* was found. We found that with every geometry, a Hall factor  $\alpha$  can be associated, from which one can obtain the temperature dependence. We calculated numerically the electrical potential, the current distribution and the charge distribution in such a device. The Hall factor  $\alpha$  was found as function of  $W_I$ ,  $W_V$ ,  $x_f$ ,  $d_f$ , and  $h$ , in order to find the optimal parameters for the device. We found that their qualitative behaviour can be well understood by the average magnetic field inside the Hall cross, except for devices where the geometry was altered, i.e. when  $W_I$ ,  $W_V$ , or  $x_f$  was changed.

# 8

---

## *Summary*

The last three decades have witnessed the rapid advance of solid-state electronics, including first the replacement of discrete circuit elements, and finally the integration of many circuit elements onto one semiconductor chip. The only fundamental discrete elements that have been left behind are those involving magnetic materials. It is only recently that one has started to incorporate magnetic materials into planar integrated electronic circuitry. The integration of those materials would allow the electronic flexibility of semiconductor-base quantum structures to be combined with local magnetism, enabling the development of new magnetoelectronic devices based on ... new physics.

The possibility provided by present day fabrication technologies, to create inhomogeneous magnetic fields on a micrometer and nanometer scale, indeed also raises questions from fundamental, theoretical point of view: how do electrons behave in mesoscopic samples under application of an inhomogeneous magnetic field? In this thesis we elaborate on that question.

Therefore, this thesis is in a way bipartite: on one hand we are in search for new phenomena/physics which might occur thanks to these recent fabrication technologies (chapters 2, 3, 4), on the other hand we try to explain recently obtained experimental results on these new systems (chapters 5, 6, 7).

Electronic transport in mesoscopic systems can be subdivided in different regimes, depending on the physics that determine the transport: one can distinct the quantum, the ballistic, the diffusive and the classical regime. We consider two-dimensional electron transport in all four regimes.

In this thesis, we start with purely quantum systems, in which electrons do not suffer from any collisions. In **chapter 2**, we study quantum states in

a magnetic anti-dot. This is a new system in which electrons are confined in two dimensions by an inhomogeneous magnetic field. The system consists of a heterostructure with on top of it a superconducting disk. This magnetic anti-dot has the interesting property that the filling of the dot is a discrete function of the magnetic field. For some of the bound states the circulating electron current inside and outside the anti-dot can be in opposite direction. Such states exhibit a diamagnetic to paramagnetic transition with increasing magnetic field. Because of the non-quadratic nature of the confinement potential, the absorption spectrum consists of many peaks, some of which violate Kohn's theorem, which is due to the coupling of the center of mass motion with the other degrees of freedom.

In **chapter 3**, we study the electron motion near magnetic field steps at which the strength and/or sign of the magnetic field changes. We calculate the energy spectrum for such systems and compare the electron states (bound and scattered) with their corresponding classical paths: they correspond to snake orbits and cycloidlike states. We compare several classical properties as the velocity parallel to the edge, the oscillation frequency perpendicular to the edge and the extent of the states with their quantum mechanical counterpart and distinguish a class of magnetic edge states which do not have a classical counterpart.

In **chapter 4**, we consider electron transport in the ballistic regime. In this regime electrons propagate through the two-dimensional electron gas (2DEG) as pointlike particles. No impurity scattering is present, only circular symmetric steplike magnetic profiles with zero average magnetic field deflect locally the electrons from their classical trajectories. First we concentrate on this scattering on such a single magnetic profile; we study its quasi-bound and scattered states. Next, we calculate the effect of a random distribution of such identical profiles on the transport properties of a 2DEG. We show that a remarkable nonzero Hall resistance can be obtained, although  $\langle B_z \rangle = 0$ , and that in some cases the Hall resistance can even change sign as function of the Fermi energy or the magnetic field strength. The Hall and the magnetoresistance show two pronounced types of resonances, resulting from i) the Landau states of the inner core, and ii) from the quasi-bound snake orbit states of the individual profiles.

When electrons propagate diffusively through the 2DEG, we arrive at the diffusive regime. Recently Nogaret *et al.*[58] (University of Bath, U.K.) did experiments on a quantum wire in which the transport was diffusive. They subjected this wire to a magnetic field barrier parallel to the wire direction and measured the Hall and magnetoresistance as function of an applied perpendicular magnetic field. In **chapter 5**, we study this situation and explain their experimental results for the magneto- and the Hall resistance using a semi-classical theory based on the Landauer-Büttiker formula. We explain the observed positive magnetoresistance peak as due to a competition between a decrease of the number of conducting channels as a result of the growing magnetic field, from the fringe field of the ferromagnetic stripe as it becomes

magnetized, and the disappearance of snake orbits and the subsequent appearance of cycloidlike orbits, which we already encountered in chapter 3.

For higher temperatures, scattering on phonons and other phase breaking collisions reduce the quantum mechanical effects, and transport can be considered classical. In **chapter 6**, we study the diffusive classical transport in a 2DEG subjected to a locally inhomogeneous magnetic field resulting from an in-plane magnetized film deposited above the 2DEG. This is actually the basis configuration of a novel magnetoelectronic device suggested by Johnson *et al.*,[38] (Naval Research Laboratory, Washington D.C., U.S.A.) which has potential applications as non volatile memory element and magnetometer. We explain their room temperature experiments performed on this device and show that the output of this device scales inversely with the size of both the voltage and the current probes.

In **chapter 7**, we elaborate on this system and study the temperature dependency of this device, as was investigated experimentally by Monzon *et al.*[54] (California Institute Of Technology, California, U.S.A.) We find our theoretical results to be in good agreement with their experimental results and find that with every geometry one can associate a temperature independent Hall factor  $\alpha$ , such that the temperature dependency of the device is only contained in that of the electron density. We calculate this Hall factor for different geometries, i.e., as function of the width of both the voltage and current probes, the thickness of the film and its distance to the 2DEG, in order to obtain the optimal parameters for the device.



# 9

---

## *Samenvatting*

De drie laatste decennia heeft de vaste stof-elektronica een enorme vooruitgang geboekt: wat begon bij de vervanging van de buisdiode, resulteerde uiteindelijk in de integratie van vele circuitelementen in één halfgeleiderchip. De enige fundamentele circuitelementen die bij deze revolutie ontzien werden, waren deze betreffende magnetische materialen. Het is pas recent dat men gestart is met het incorporeren van magnetische materialen in vlakke geïntegreerde elektronische circuits. De integratie van dergelijke materialen maakt het mogelijk om de elektronische flexibiliteit van de op halfgeleiders gebaseerde kwantumstructuren te combineren met lokaal magnetisme, wat de weg vrij maakt voor de ontwikkeling van nieuwe mageneto-elektronische devices, gebaseerd op ... nieuwe fysica.

De mogelijkheid om inhomogene magneetvelden op micrometer en nanometerschaal te creëren, werpt immers ook vragen op vanuit fundamenteel theoretisch oogpunt: hoe gedragen elektronen zich in mesoscopische systemen onder invloed van een inhomogeen magneetveld? In deze thesis buigen we ons over deze vraag.

Dit doctoraat is dan ook tweeledig: enerzijds gaan we op zoek naar nieuwe fysische fenomenen die kunnen plaatsgrijpen dankzij deze nieuwe technologieën (hoofdstukken 2, 3, 4), anderzijds trachten we recente experimenten op deze nieuwe systemen te verklaren (hoofdstukken 5, 6, 7).

Elektronisch transport in mesoscopische systemen kan onderverdeeld worden in verschillende regimes, waar het transport door andere fysica bepaald wordt: zo onderscheiden we het kwantum, het ballistisch, het diffusief en het klassiek regime. In deze thesis onderzoeken we tweedimensionaal transport in elk van deze regimes.

We beginnen met pure kwantumsystemen, waar elektronen niet te lijden hebben onder botsingen. In **hoofdstuk 2**, bestuderen we kwantumtoestanden in een magnetische antistip. Dit is een nieuw systeem waar elektronen opgesloten zijn in twee dimensies door een inhomogeen magneetveld. Het systeem bestaat uit een heterostructuur waarop een supergeleidende schijf geplaatst wordt. De magnetische antistip heeft de bijzondere eigenschap dat de opvulling van de stip een discrete functie is van de magneetveldsterkte. De elektronstroom binnen en buiten de antistip kunnen bij sommige gebonden toestanden in tegengestelde richting vloeien. Dergelijke toestanden vertonen een diamagnetische-paramagnetische transitie bij toenemend magneetveld. Vermits de opsluitingspotentialiaal niet kwadratisch is, vertoont het absorptiespectrum talrijke pieken, waarvan sommige niet voldoen aan Kohns theorema, wat toegeschreven kan worden aan de koppeling van de beweging van het massamiddelpunt met de andere vrijheidsgraden.

In **hoofdstuk 3** bestuderen we de elektronbeweging nabij een magneetveldstap, waarbij de sterkte en/of het teken van het magneetveld abrupt verandert. We berekenen het energiespectrum voor deze systemen en vergelijken zowel de gebonden als de verstrooide elektrontoestanden met hun overeenkomstige klassieke banen: de zogenaamde slangenbanen en cycloïdeachtige banen. We toetsen verschillende klassieke eigenschappen, zoals de snelheid parallel met de rand, de oscillatiefrekwentie loodrecht op de rand en de uitgebreidheid van de toestanden, aan hun kwantummechanische tegenhanger en we onderscheiden een klasse van magnetische-randtoestanden die niet klassiek begrepen kunnen worden.

In **hoofdstuk 4** beschouwen we elektrontransport in het ballistisch regime. In dit regime bewegen elektronen zich in het tweedimensionaal elektrongas (2DEG) als puntdeeltjes. Er zijn geen verstrooiingen t.g.v. onzuiverheden; elektronen worden alleen verstrooid aan cilindrisch symmetrische stapsgewijze magneetveldprofielen met gemiddeld magneetveld nul. Vooreerst beperken we ons tot verstrooiing aan slechts één enkel magneetveldprofiel en bestuderen we de hiermee corresponderende quasi-gebonden en verstrooide toestanden. Vervolgens berekenen we het effect van een random verzameling van zulke identieke profielen op de transporteigenschappen van een 2DEG. We tonen aan dat een Hallweerstand verkregen kan worden, niettegenstaande  $\langle B_z \rangle = 0$ , en dat deze Hallweerstand in sommige gevallen zelfs van teken kan veranderen als functie van de Fermi-energie of de magneetveldsterkte. De Hall- en de magnetoweerstand vertonen twee types van resonanties, overeenstemmend met i) de Landautoestanden in de binnenste kern, en ii) de quasi-gebonden slangenbanen van de individuele profielen.

Indien de elektronen zich diffusief door het 2DEG bewegen, belanden we in het diffusief regime. Recent hebben Nogaret *et al.*[58] (University of Bath, U.K.) experimenten uitgevoerd op een kwantumdraad in dit regime: in de draad creëerden zij een magneetveldbarrière parallel met de draad en zij maten de Hall en de magnetoweerstand als functie van een uitwendig aangelegd magneetveld. In **hoofdstuk 5** bestuderen we deze situatie, en verklaren we hun

experimentele resultaten voor de Hall- en de magnetoweerstand, waarbij we gebruik maken van een semi-klassieke theorie die gebaseerd is op de Landauer-Büttiker formule. We schrijven de geobserveerde positieve piek in de magnetoweerstand toe aan een competitie tussen i) een vermindering van het aantal geleidingskanalen in de draad t.g.v. het toenemende magneetveld afkomstig van de ferromagnetische strip wanneer die gemagnetiseerd wordt, en ii) het verdwijnen van slangenbanen en vervolgens het opduiken van cycloïde banen, die we al in hoofdstuk 3 waren tegengekomen.

Bij hogere temperaturen worden kwantummechanische effecten vernietigd door interacties met fononen en door andere fasevernietigende botsingen, waardoor het transport klassiek beschouwd kan worden. In **hoofdstuk 6** bestuderen we diffusief klassiek transport in een 2DEG onderhevig aan een lokaal inhomogeen magneetveld afkomstig van een ferromagnetische film met magnetizatie in het vlak, geplaatst boven het 2DEG. Dit is de basisopstelling van een nieuw magneto-elektronisch device, voorgesteld door Johnson *et al.*[38] (Naval Research Laboratory, Washington D.C., U.S.A.), dat mogelijk toepassingen heeft als niet-vluchtig geheugenelement en als magnetometer. Wij verklaren hun experimentele resultaten uitgevoerd op dit device bij kamertemperatuur en tonen aan dat de prestatie van dit device omgekeerd schaalt met de grootte van zowel de spannings- als de stroomprobes.

Ook in **hoofdstuk 7** behandelen we dit device, en onderzoeken we zijn temperatuursafhankelijkheid, die experimenteel bestudeerd werd door Monzon *et al.*[54] (California Institute Of Technology, California, U.S.A.) Onze theoretische resultaten zijn in goede overeenkomst met hun experimentele resultaten en we vinden dat met elke geometrie een temperatuursonafhankelijke Hallfactor kan geassocieerd worden, zodat de temperatuursafhankelijkheid van het device volledig vervat is in die van de elektrondichtheid. We berekenen deze Hallfactor voor verscheidene geometrieën, i.e. als functie van zowel de spannings- als de stroomprobes, de dikte van de film en van zijn afstand tot het 2DEG, teneinde de optimale parameters van het device te bepalen.



# 10

---

## *List of Publications*

1. J. Reijniers and F. M. Peeters, Appl. Phys. Lett. **73**, 357 (1998).
2. J. Reijniers, F. M. Peeters, and A. Matulis, Phys. Rev. B **59**, 2817 (1999).
3. F. M. Peeters, J. Reijniers, S. M. Badalian, and P. Vasilopoulos, Micro-electronic engineering **74**, 405 (1999).
4. J. Reijniers, A. Matulis and F. M. Peeters, Physica E **6**, 759 (2000).
5. J. Reijniers and F. M. Peeters, J. Appl. Phys. **87**, 8088 (2000).
6. J. Reijniers and F. M. Peeters, J. Phys.: Condens. Matter **12**, 9771 (2000).
7. J. Reijniers and F. M. Peeters, Phys. Rev. B, (2001).



# References

1. *Handbook of Mathematical Functions*, M. Abramowitz and I. A. Stegun, (National Bureau of Standards/Dover Publications, New York, 1970).
2. H. Akinaga, J. de Boeck, G. Borghs, S. Miyanishi, A. Asamitsu, W. Van Roy, Y. Tomioka and L. H. Kuo, *Appl. Phys. Lett.* **72**, 3368 (1998).
3. S. M. Badalyan and F. M. Peeters, to be published (2001).
4. H. U. Baranger, *Phys. Rev. B* **42**, 11479 (1990).
5. A. Barthélémy, A. Fert, R. Morel and L. Steren, *Physics World* November, 34 (1990).
6. C. W. J. Beenakker, *Phys. Rev. Lett.* **62**, 2020 (1989).
7. J. Bending and A. Oral, *J. Appl. Phys.* **81**, 3721 (1997).
8. L. Brey and H. A. Fertig, *Phys. Rev. B* **47**, 15961 (1993).
9. M. Büttiker, *Phys. Rev. Lett.* **57**, 1761 (1986).
10. M. Büttiker, *Phys. Rev. B* **38** (1988).
11. A. A. Bykov, G. M. Gusev, J. R. Leite, A. K. Bakarov, N. T. Moshegov, M. Cassé, D. K. Maude and J. C. Portal, *Phys. Rev. B* **61**, 5505 (2000).
12. M. Calvo, *Phys. Rev. B* **48**, 2365 (1993).

13. *Quantum Mechanics*, C. Cohen-Tannoudji, B. Diu, and F. Laloë, (John Wiley & Sons, Paris, 1977), p. 827.
14. S. Datta and M. K. McLennan, Rep. Prog. Phys. **53**, 1003 (1990).
15. M. Dax, Semiconductor International, September, 84 (1997).
16. J. de Boeck and G. Borghs, Physics World, Vol.12 (April, 1999), p. 27.
17. S. V. Dubonos, A. K. Geim, K. S. Novoselov, J. G. S. Lok, J. C. Maan, and M. Henini, Physica E **6**, 746 (2000).
18. C. L. Foden, M. L. Leadbeater, J. H. Burroughes, and M. Pepper, J. Phys.: Condens. Matter **6** (1994).
19. C. L. Foden, M. L. Leadbeater and M. Pepper, Phys. Rev. B **52**, 8646 (1995).
20. F. Geerinckx, F. M. Peeters and J. T. Devreese, J. Appl. Phys. **68**, 3435 (1990).
21. A. K. Geim, JETP Lett. **50**, 389 (1989).
22. A. K. Geim, S. V. Dubonos, J. G. S. Lok, I. V. Grigorieva, J. C. Maan, L. T. Hansen, and P. E. Lindelof, Appl. Phys. Lett. **71**, 2379 (1997).
23. A. K. Geim, I. V. Grigorieva, S. V. Dubonos, J. G. S. Lok, J. C. Maan, A. E. Filippov, and F. M. Peeters, Nature **390**, 259 (1997).
24. R. R. Gerhardts, Phys. Rev. B **53**, 11064 (1996).
25. M. Governale, D. Boese, cond-mat/0009155 (2000).
26. B.-Y. Gu, W.-D. Sheng, X.-H. Wang, and J. Wang, Phys. Rev. B **56**, 13 434 (1997).
27. E. H. Hall, Am. J. Math. II, 287 (1879).
28. L. T. Hansen, R. Taboryski, A. Smith, P. E. Lindelof, P. Hedegård, Surface Science 361/362, 349 (1996).
29. P. Hedegård and A. Smith, Phys. Rev. B **51**, 10869 (1995).
30. R. D. Hofstadter, Phys. Rev. B **14**, 2239 (1976).
31. E. Hofstetter, J. M. C. Taylor and A. MacKinnon, Phys. Rev. B **53**, 4676 (1996).
32. *Micro-inhomogeneous Magnetic Fields and their effects on a Two-dimensional Electron Gas*, I. S. Ibrahim, (Phd-thesis, 1998).
33. I. S. Ibrahim and F. M. Peeters, Am. J. Phys. **63**, 171 (1995).

34. I. S. Ibrahim, V. A. Schweigert, and F. M. Peeters, *Phys. Rev. B* **56**, 7508 (1997).
35. I. S. Ibrahim, V. A. Schweigert, and F. M. Peeters, *Phys. Rev. B* **57**, 15416 (1998).
36. See, for example, *Quantum Dots*, L. Jacak, P. Hawrylak, and A. Wojs (Springer-Verlag, Berlin, 1998).
37. *Classical Electrodynamics*, J. D. Jackson, (John Wiley & Sons, New York, 1962), p. 157.
38. M. Johnson, B. R. Bennett, M. J. Yang, M. M. Miller, and B. V. Shanabrook, *Appl. Phys. Lett.* **71**, 974 (1997).
39. M. Johnson, *J. Vac. Sci. Technol. A* **16**, 1806 (1998).
40. M. Kato, A. Endo, M. Sakairi, S. Katsumoto, and Y. Iye, *J. Phys. Soc. Jpn.* **68**, 2870 (1999).
41. *Low-dimensional Semiconductors: materials, physics, technologies, devices*, M. J. Kelly, (Clarendon Press, Oxford, 1995).
42. N. Kim, G. Ihm, H.-S. Sim and K. J. Chang, *Phys. Rev. B* **60**, 8767 (1999).
43. N. Kim, G. Ihm and T. W. Kang, to be published.
44. *La Physique des Semiconducteurs*, P. Kiréev, (Editions MIR, Moscou, 1975).
45. *Introduction to Solid State Physics*, C. Kittel, (John Wiley & Sons, New York, 1996).
46. *Quantum transport in Semiconductor Submicron Structures*, B. Kramer, (Kluwer Academic Publishers, Dordrecht, 1996), p. 6.
47. V. Kubrak, F. Rahman, B. L. Gallagher, P. C. Main, M. Henini, C. H. Marrows, and M. A. Howson, *Appl. Phys. Lett.* **74**, 2507 (1999).
48. *The Application of High magnetic fields in Semiconductor Physics*, edited by G. Landwehr, Lecture Notes in Physics Vol. 177 (Springer-Verlag, Berlin, 1983).
49. D. N. Lawton, A. Nogaret, S. J. Bending, D. K. Maude, J. C. Portal and M. Henini, to appear in *Phys. Rev. B* (2001).
50. G. P. Mallon and P. A. Maksym, *Semimag - 13* (Nijmegen, 1998).
51. Y. I. Man'kov, *Soviet Physics-Solid State* **14**, 62 (1972); Y. I. Balkarei and L. N. Bulaevskii, *Soviet Physics-Solid State* **14**, 2018 (1973); A.S.

- Rozhavsky and R. I. Shekhter, *Solid State Commun.* **12**, 603 (1973); G. G. Cabrera and L. M. Falicov, *Phys. Stat. Sol. (b)* **61**, 539 (1974); *ibid.*, *Phys. Stat. Sol. (b)* **62**, 217 (1974); L. Berger, *J. Appl. Phys.* **49**, 2156 (1978); Y. V. Zakharov and Y. I. Man'kov, *Phys. Stat. Sol. (b)* **125**, 197 (1984).
52. A. Matulis and F. M. Peeters, *Phys. Rev. B* **62**, 91 (2000).
53. A. Matulis, F. M. Peeters, and P. Vasilopoulos, *Phys. Rev. Lett.* **72**, 1518 (1994).
54. F. G. Monzon, M. Johnson, and M. L. Roukes, *Appl. Phys. Lett.* **71**, 3087 (1997).
55. *Methods of Theoretical Physics*, Morse and Feshbach, (McGraw-Hill, New York, 1953), p. 1292.
56. J. E. Müller, *Phys. Rev. Lett.* **68**, 358 (1992).
57. M. Nielsen and P. Hedegård, *Phys. Rev. B* **51**, 7679 (1995).
58. A. Nogaret, S. J. Bending and M. Henini, *Phys. Rev. Lett.* **84**, 2231 (2000).
59. A. Nogaret, S. Carlton, B. L. Gallagher, P. C. Main, M. Henini, R. Wirtz, R. Newbury, M. A. Howson, S. P. Beaumont, *Phys. Rev. B* **55**, 16037 (1997).
60. N. Overend, A. Nogaret, B. L. Gallagher, P. C. Main, M. Henini, C. H. Marrows, M. A. Howson and S. P. Beaumont, *Appl. Phys. Lett.* **72**, 1724 (1998).
61. F. M. Peeters, *Phys. Rev. Lett.* **61**, 589 (1988).
62. F. M. Peeters, *Superlattices and Microstructures* **6**, 217 (1989).
63. F. M. Peeters, *Phys. Rev. B* **56**, 1468 (1990).
64. F. M. Peeters, *Physics World* **8**, 24 (October 1995).
65. F. M. Peeters and J. De Boeck, in *Handbook of nanostructured materials and technology*, Edited by N. S. Nalwa, Vol. 3 (Academic Press, N. Y., 1999), p. 345.
66. F. M. Peeters and X. Q. Li, *Appl. Phys. Lett.* **72**, 572 (1998).
67. F. M. Peeters and A. Matulis, *Phys. Rev. B* **48**, 15166 (1993).
68. F. M. Peeters, A. Matulis, and I. S. Ibrahim, *Physica B* **227**, 131 (1996).
69. F. M. Peeters, J. Reijniers, S. M. Badalian, and P. Vasilopoulos, *Micro-electronic engineering* **74**, 405 (1999).

70. F. M. Peeters and P. Vasilopoulos, *Surface Science* **229**, 271 (1990).
71. F. M. Peeters and P. Vasilopoulos, *Phys. Rev. B* **46**, 4667 (1992).
72. F. M. Peeters and P. Vasilopoulos, *Phys. Rev. B* **47**, 1466 (1993).
73. G. A. Prinz, *Phys. Today* **48**, 58 (1995).
74. J. Reijniers, A. Matulis and F. M. Peeters, *Physica E* **6**, 759 (2000).
75. J. Reijniers and F. M. Peeters, *Appl. Phys. Lett.* **73**, 357 (1998).
76. J. Reijniers and F. M. Peeters, *J. Appl. Phys.* **87**, 8088 (2000).
77. J. Reijniers and F. M. Peeters, *J. Phys.: Condens. Matter* **12**, 9771 (2000).
78. J. Reijniers and F. M. Peeters, *Phys. Rev. B*, (2001).
79. J. Reijniers, F. M. Peeters, and A. Matulis, *Phys. Rev. B* **59**, 2817 (1999).
80. *Electronic Properties of Multilayers and Low-Dimensional Semiconductor Structures*, M. L. Roukes, T. J. Thornton, A. Scherer and B. P. Van de Gaag, (Plenum, London, 1990).
81. A. W. Rushforth, B. L. Gallagher, P. C. Main, A. C. Neumann, C. H. Marrows, I. Zoller, M. A. Howson, B. J. Hickey and M. Henini, *Physica E* **6**, 751 (2000).
82. *Modern Quantum Mechanics*, J. J. Sakurai, (Addison-Wesley Publishing Company, 1994).
83. J. Shi, J. M. Kikkawa, R. Proksch, T. Schäffer, D. D. Awschalom, G. Medeiros-Ribeiro and P. M. Petroff, *Nature* **377**, 707 (1995).
84. H.-S. Sim, K.-H. Ahn, K. J. Chang, G. Ihm, N. Kim, and S. J. Lee, *Phys. Rev. Lett.* **80**, 1501 (1998).
85. J. L. Simonds, *Physics Today* April, 25 (1995).
86. A. Smith, R. Taboryski, L. T. Hansen, C. B. Sørensen, P. Hedegård, and P. E. Lindelof, *Phys. Rev. B* **50**, 14 726 (1994).
87. L. Solimany and B. Kramer, *Solid State Commun.* **96**, 471 (1995).
88. S. Souma and A. Suzuki, *Phys. Rev. B* **60**, 15 928 (1999).
89. O. Tchernyshyov, F. Wilczek, *Phys. Rev. B* **62**, 4208 (2000).
90. T. J. Thornton, M. L. Roukes, A. Scherer and B. P. Van de Gaag, *Phys. Rev. Lett.* **63**, 2128 (1989).

91. T. Vančura, T. Ihn, S. Broderick, K. Ensslin, W. Wegscheider, and M. Bichler, *Phys. Rev. B* **62**, 5074 (2000).
92. H. van Houten, C. W. J. Beenakker, P. H. M. van Loosdrecht, T. J. Thornton, H. Ahmed, M. Pepper, C. T. Foxon and J. J. Harris, *Phys. Rev. B* **37**, 8534 (1988).
93. W. Wayt, *Scientific American*, May, 9 (1999).
94. D. Weiss, K. von Klitzing, K. Ploog, and G. Weimann, *Europhys. Lett.* **8**, 179 (1989);
95. P. D. Ye, D. Weiss, G. Luthering, R. R. Gerhardts, K. Von Klitzing, K. Eberl, H. Nickel and G. Weimann, 23rd International Conference on the Physics of Semiconductors (World Scientific, Singapore, 1997), p. 1529.
96. P. D. Ye, D. Weiss, K. von Klitzing, K. Eberl and H. Nickel, *Appl. Phys. Lett.* **67**, 1995.
97. *Fundamentals of Semiconductors: physics and materials properties*, P. Y. Yu, (Springer-Verlag, Berlin, 1996).
98. S. D. M. Zwerschke, A. Manolescu, and R. R. Gerhardts, *Phys. Rev. B* **60**, 5536 (1999).